Max Planck Institut für Kolloid und Grenzflächenforschung

Novel lithium iron phosphate materials for lithium-ion batteries

Dissertation

zur Erlangung des akademischen Grades
"doctor rerum naturalium"
(Dr. rer. nat.)
in der Wissenschaftsdisziplin "Kolloidchemie"

eingereicht an der
Mathematisch-Naturwissenschaftlichen Fakultät
der Universität Potsdam

von

Jelena Popović

Potsdam, im Juni 2011

Table of Contents

1 Introduction

Energy production and storage has been one of the main questions and societal challenges since the beginning of mankind, with wide impact on environment, human health and world's economy. Conventional energy sources (coal, oil and natural gas) are diminishing and non-renewable, take million years to form and are indirectly causing regional and global conflicts as well as environmental degradation. As a worrying example, mass combustion of fuels lead to generation of CO_2 greenhouse gas whose annual global emission rose by 80% between 1970 and 2004 making it responsible for global warming (reported on the 2009 United Nations Climate Change Conference). Thus, in the 21st century, we have to aim at achieving sustainable, environmentally friendly and cheap energy supply by employing renewable energy technologies (solar energy, wind power, geothermal energy, biomass and biofuel, hydropower) associated with portable energy storage devices that can quickly capture and release energy.

Rechargeable batteries can repeatedly generate clean energy from stored materials and convert reversely electric into chemical energy. They have been developed to power a wide variety of applications which can be mainly classified into portable electronic consumer devices (cell phones, laptop computers etc.), electric vehicles and large-scale electricity storage in smart or intelligent grids (Figure 1.1).

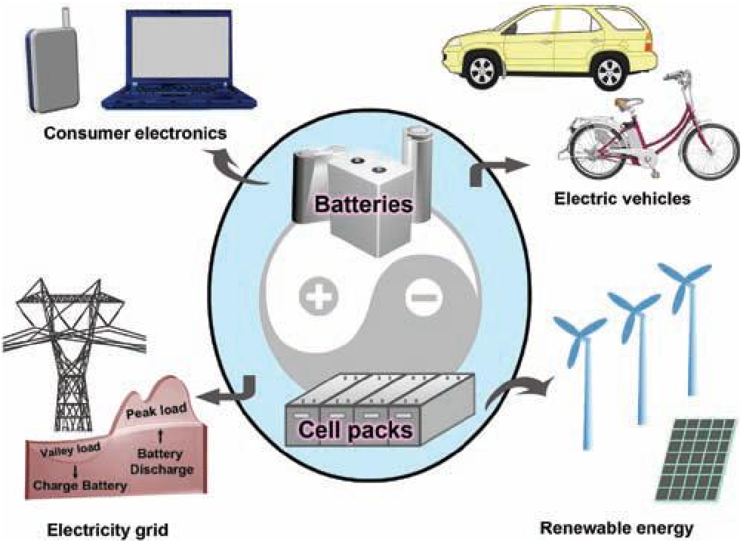

Figure 1.1 Schematic representation of applications for rechargeable batteries [1].

Amongst various existing technologies (lead-acid, nickel-cadmium), lithium-ion batteries have the advantage of high voltage, long cycling life, high power (Figure 1.2), high reliability and design flexibility. However, energy storage progress in lithium-ion batteries cannot be compared to the progress in computer industry (doubling of the memory capacity every two years according to Moore's law), and major breakthroughs are needed [2, 3].

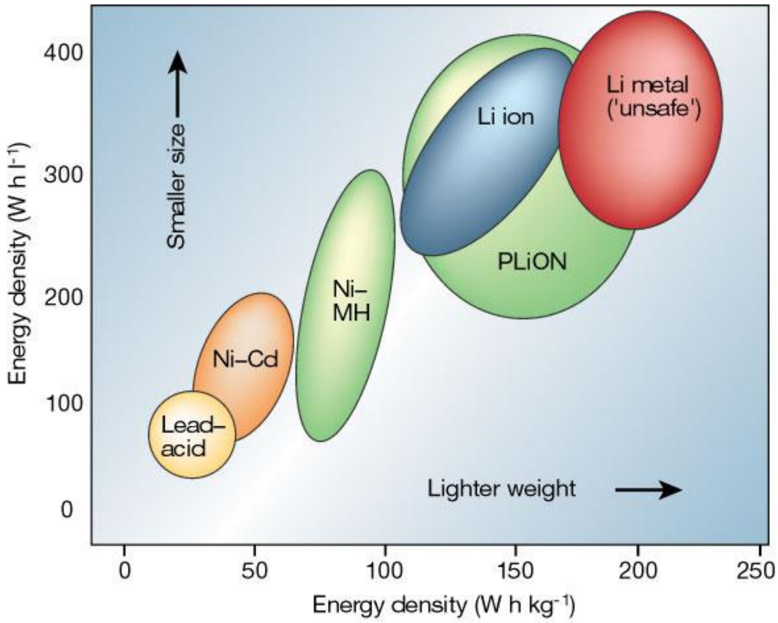

Figure 1.2 Comparison of different battery systems in terms of volumetric and gravimetric energy density [4].

The performance of lithium-ion batteries depends intimately on the properties of their materials. Presently used battery electrode materials are expensive to be produced; they offer limited energy storage possibility and are unsafe to be used in larger dimensions limiting the diversity of application, especially in hybrid electric vehicles (HEVs) and electric vehicles (EVs). Most recently, in 2006, a Dell® laptop battery explosion was reported owing to the uncontrolled oxygen build-up and as a result, 4.1 million Sony® batteries have been recalled from the market leaving the company and customers in a bad position. Thus, developing new type of enhanced lithium-ion battery materials and simplified, eco-efficient and environmentally friendly synthesis routes to accompany them is crucial for the future development of lithium-ion battery concept.

Lithium iron phosphate ($LiFePO_4$) has been discovered in the late 1990s and is currently the most studied positive electrode (“cathode”) material for lithium-ion batteries, with a possibility to be fully employed and commercialized in the following years. However, researchers are still in the lookout for a perfect morphology and the easiest up-scalable synthesis method in order for this goal to be met. In this scope, the findings presented in my thesis are related to new solvothermal methods which enable the production of two very different morphologies of $LiFePO_4$, namely - mesocrystals and nanostructured materials.

This thesis is structured as follows:

- In the first part (Chapter 2), some basic principles of lithium-ion batteries are introduced, followed by a short overview on already existing electrode materials. A more detailed insight into why $LiFePO_4$ is the lithium-ion battery electrode material of the future is provided through explanations of its crystalline structure, electrochemical properties and presently used synthetic techniques.
- Some of the most important analytical methods needed for a deeper understanding of the materials synthesized and described in this thesis are further presented in Chapter 3.
- The core of this thesis is represented in Chapters 4 and 5, where detailed information on synthesis and characterization (electron micrographs, powder diffraction patterns, electrochemical testing) are presented and discussed for two $LiFePO_4$ morphologies, mesocrystals (Chapter 4) and nanostructures (Chapter 5).

- Chapter 6 consists of some general conclusions as well as new ideas on future research concerning $LiFePO_4$ structures presented in this thesis.

2 $LiFePO_4$ as a cathode material in lithium-ion batteries

2.1 Introduction to lithium-ion batteries

Since its discovery and commercialization by Sony Corp. in the early 1990s [5], lithium-ion battery became the most important secondary battery produced by billion units per year and thus triggered the revolution of portable electronic devices. Typical commercially used lithium-ion battery consists of several interconnected electrochemical cells, where each cell is composed of a graphite anode (e.g. mesocarbon microbeads), a cathode formed by lithium metal oxide (e.g. $LiCoO_2$) and electrolyte (e.g. $LiPF_6$ dissolved in ethylene carbonate/dimethyl carbonate mixture) embedded in a separator felt. During discharge, Li^+ ions are extracted from the layered graphite, they pass through the electrolyte and intercalate between the $LiCoO_2$ layers (Figure 2.1).

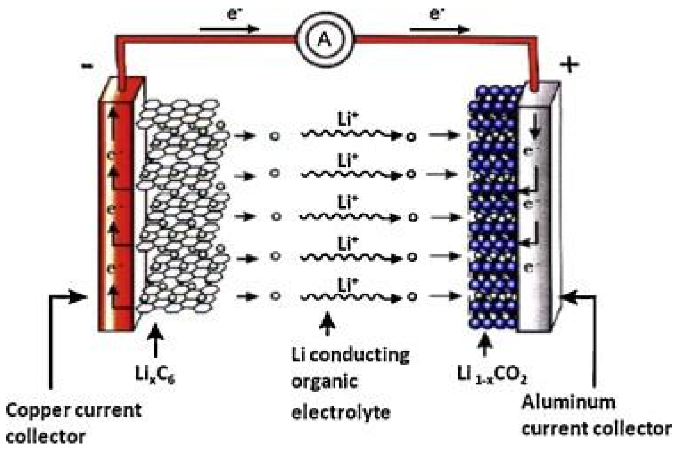

Figure 2.1 Schematic representation of a typical commercial lithium-ion battery showing the discharge intercalation mechanism [6].

The process is reversible during charge in a rechargeable (secondary) battery:

$$yC + LiCoO_2 \leftrightarrow Li_xC_y + Li_{1-x}CoO_2,\ x \approx 0.5,\ y = 6,\ V_{oc} \approx 3.7\ \text{V}. \qquad (1)$$

Lithium-ion battery is also referred to a “rocking-chair” battery as Li^+ ions “rock” back and forth between the positive and negative electrode. Simultaneously to Li^+ intercalation/deintercalation, the electrons pass through an external circuit enabling the current to be retrieved by user. Detailed account on science and technology of lithium-ion batteries can be found in extensive literature [4, 7-12].

The amount of electrical energy that any battery is able to deliver can be expressed per unit of weight as gravimetric energy density (W h kg^{-1}) or per unit of volume as volumetric energy density (W h l^{-1}). The energy density in a lithium-ion battery is a product of its cell potential, V_{OC} and the capacity of reversible charge transfer per unit weight or unit volume, Λ. The values of V_{OC} and Λ are linked directly to the intrinsic properties of the materials that form the positive and negative electrodes. Furthermore, the cycle-life and lifetime of a lithium-ion battery are dependent on the nature of the interfaces between the electrodes and electrolyte, while safety is the function of the stability of the electrodes and electrode/electrolyte interfaces. Thus, the key for building better lithium-ion batteries with high energy density, long life, small size, and light weight, low cost and environmental compatibility lies in the new chemistry of anode and cathode materials.

Figure 2.2 shows various materials that can be potentially used as anode (denoted as negative materials) or cathode (denoted as positive materials) in a lithium-ion battery.

In the case of anode, Li metal is found to be the most electropositive (-3.04 V versus standard hydrogen electrode) with large reversible capacity (≈ 4000 A h kg^{-1}). However, due to safety considerations (explosion hazards as a result of dendrite growth during cycling), metallic Li has been substituted by various carbonaceous materials (Li_xC_6) [13].

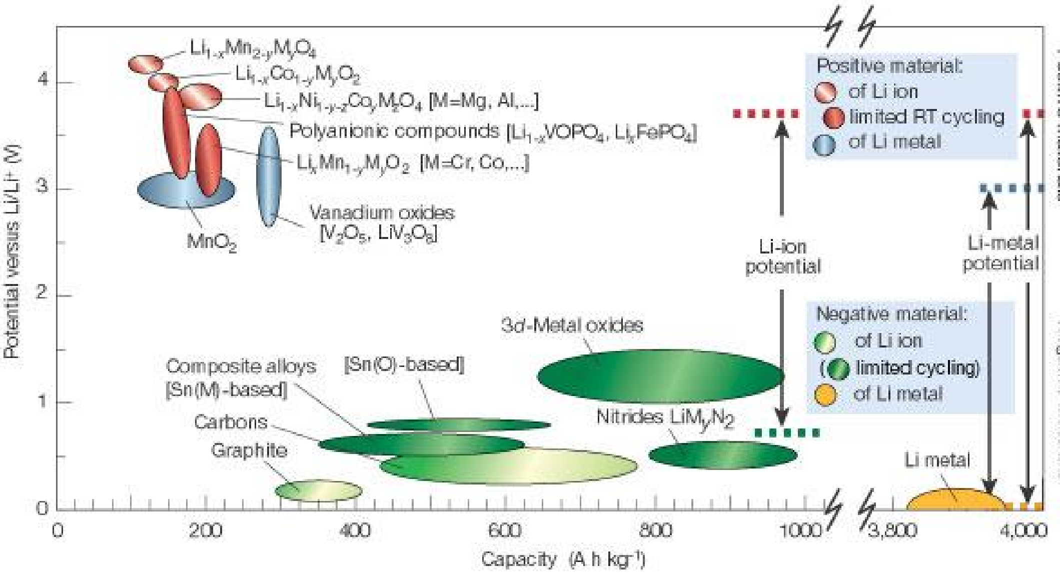

Figure 2.2 Comparison of various lithium-ion battery anode and cathode materials in terms of voltage and capacity [4].

Carbon-lithium anodes have much lower gravimetric and volumetric energy densities than pure lithium which lead towards the development of interstitial-free 3d transition-metal oxides (M_xO_y, M = Fe, Co, Ni, Mn, Cu). These materials are able to incorporate more than one Li^+ per metal through conversion (displacement) reactions giving higher capacities (≈ 800 A h kg^{-1}) in comparison to carbon anodes [14-17]. Large reversible capacities have also been reported for Li transition-metal nitrides ($Li_{3-x}Co_xN$: 900 A h kg^{-1}) which are not commercialized until now due to their high moisture-sensitivity [18-21].

In the recent years, it has been discovered that some main-group elements can generate Li alloys with high theoretical capacities ($Li_{4.4}Si$: 4200 A h kg^{-1} – larger than of Li metal, $Li_{4.4}Ge$: 1600 A h kg^{-1}, LiAl and $Li_{4.4}Sn$: 900 A h kg^{-1} and Li_3Sb: 665 A h kg^{-1} [22]). The main problem concerning application of these materials was their severe volume expansion during cycling (in the order of 300% for Si) which causes fast cracking and pulverization of the electrode. To address this issue, various different morphologies of metal-Li alloys have been suggested as volume change buffers, such as nanowires/nanoparticles with or without carbon coating, mostly for Si and Sn based materials [23-27]. In 2008, the group of Dr. Maria-Magdalena Titirici (Max Planck Institute of Colloids and Interfaces) was able to synthesize mesoporous SnO_2 microspheres [28] and $Si@SiO_x/C$ nanocomposite [29] using easy, low temperature, up-scalable hydrothermal route with obtained stable capacities as high as 370 A h kg^{-1} and 1000 A h kg^{-1}, respectively. It is worth noting that Sn-based anodes have already been applied in a commercial Nexelion™ battery (Sony Corp., 2005).

The area of potentially greatest opportunity for the materials chemist is however the cathode. Basic requirements for a cathode material have been proposed by Whittingham [2] and it should:

(i) consist of a reducible/oxidizable ion such as transition metal;
(ii) intercalate lithium reversibly and without severe structural change;
(iii) react with lithium with a high free energy for high voltage;
(iv) react with lithium rapidly during insertion/removal for high power;
(v) be a good electronic conductor;
(vi) preferably be of low cost and environmentaly benign.

Presently employed layered cathode material $Li_{1-x}CoO_2$ has desirable electrochemical properties ($V_{OC} \approx 4$ V vs. Li^+/Li^0 and high volume energy density) for hand-held devices. However, this material cannot be employed for the new generation of HEVs and EVs for several reasons:

(i) its reversible capacity is limited to $x \approx 0.5$ related to chemical instability (redox active $Co^{3+/4+}$:t_{2g} band lies on the top of O^{2-}:2p band, [30]) which finally results in realtively low specific capacity of 140 A h kg^{-1};
(ii) during overcharge, O_2 forms inside the cell building high pressure, and causing rapid temperature increase and possible battery explosion [31];
(iii) production of $LiCoO_2$ is expensive due to cobalt's low availability in comparison to other transition metals (20 ppm in the earth's crust);
(iv) Co is toxic and large batteries based on $LiCoO_2$ chemistry would be unsafe for the environment.

Different layered oxides and spinel structures as well as their cationic substitutes have been employed as a substitute to $LiCoO_2$ such as Li_xNiO_2 and its Co, Ti and Mg substitutes, Li_xFeO_2, Li_xMnO_2 and its Cr substitutes, $Li_xMn_2O_4$ and its Al substitutes. All of these materials did not show satisfying electrochemical results [32, 33].

Polyanion-based compounds, $Li_xM_y(XO_4)_z$ (M = metal, X = P, S, Si, Mo, W), are now regarded to be the most promising cathode materials for future lithium-ion batteries. Among them, spinel $LiFePO_4$ has been by far most studied since its discovery. The first reports of Li^+ intercalation in $LiFePO_4$ have been published by Padhi [34, 35] in the group of John B. Goodenough in 1997 at University of Texas, Austin. From then on, $LiFePO_4$ has been recognized to encompass qualities such as:

(i) high reversible capacity of 170 A h kg^{-1} at a $V_{oc} = 3.45$ V with long cycle ability;
(ii) high safety;
(iii) possible low cost of production (earth's core consists of 80% Fe);
(iv) environmental compatibility.

Due to strong interest in further developing such type of cathode material, this PhD thesis describes novel synthetic routes to produce $LiFePO_4$ cathode material for lithium-ion batteries.

Therefore, the following subchapters will describe the state-of-art related to LiFePO$_4$ structure, Li$^+$ insertion/extraction mechanism and the existing synthetic routes for obtaining LiFePO$_4$.

2.2 Structure of LiFePO$_4$

Triphylite LiFePO$_4$ belongs to the ordered olivine family of lithium-ortho phosphates with an orthorhombic lattice structure in the space group #62, *Pnma*. The structure consists of corner-shared FeO$_6$ octahedra (*b-c* plane, forming zigzag planes), edge-shared LiO$_6$ octahedra running parallel to the *b*-axis and PO$_4$ groups which share one edge with a FeO$_6$ octahedron and two edges with LiO$_6$ octahedra (Figure 2.2). Thus, the phosphorus atoms occupy tetrahedral sites, iron and lithium atoms occupy octahedral 4a and 4c sites while oxygen atoms are located in a slightly distorted, hexagonal close-packed array. As a result of the described 3D structure, LiFePO$_4$ is a stable compound.

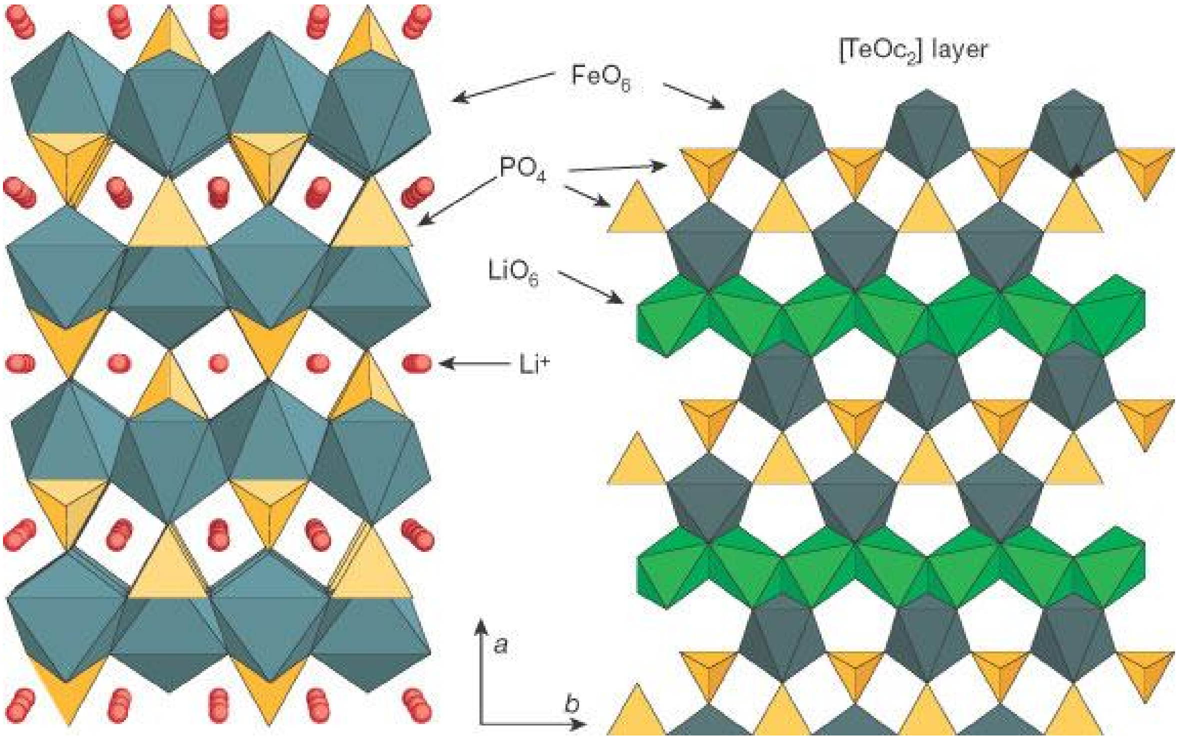

Figure 2.2 Schematic representation of LiFePO$_4$ crystal structure [4].

When Li$^+$ ions are removed from LiFePO$_4$, the remaining FePO$_4$ framework has the same structure with slight deformation to orthorhombic symmetry (6.8% volume reduction, 2.6% density increase). LiFePO$_4$ and FePO$_4$ atomic coordinates, cell parameters and interatomic distances were calculated using Rietveld refinement of X-ray powder diffraction data and are confirmed by Neutron diffraction data (Table 2.1).

The observed structure similarities between LiFePO$_4$ and FePO$_4$ help in avoiding capacity degradation that results from severe volume changes during the charge/discharge process in cathodes and can perhaps also effectively compensate volume changes of the carbon anode. Therefore, prerequisites to excellent battery cyclability are met in the LiFePO$_4$/FePO$_4$ structure.

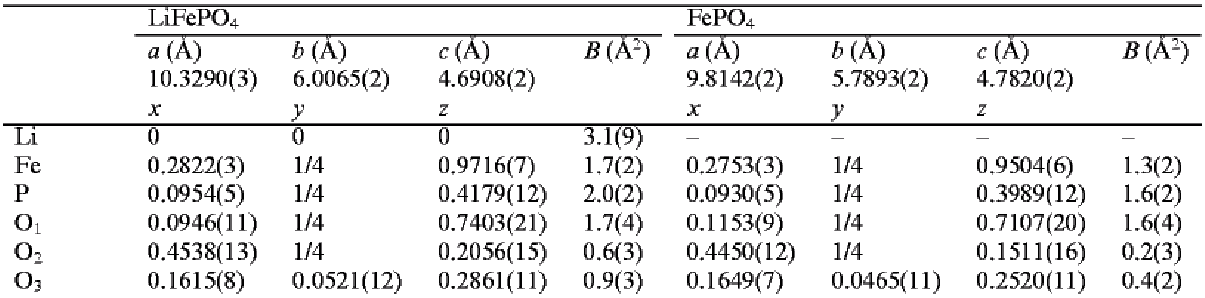

	LiFePO$_4$				FePO$_4$			
	a (Å) 10.3290(3)	*b* (Å) 6.0065(2)	*c* (Å) 4.6908(2)	*B* (Å^2)	*a* (Å) 9.8142(2)	*b* (Å) 5.7893(2)	*c* (Å) 4.7820(2)	*B* (Å^2)
	x	*y*	*z*		*x*	*y*	*z*	
Li	0	0	0	3.1(9)	–	–	–	–
Fe	0.2822(3)	1/4	0.9716(7)	1.7(2)	0.2753(3)	1/4	0.9504(6)	1.3(2)
P	0.0954(5)	1/4	0.4179(12)	2.0(2)	0.0930(5)	1/4	0.3989(12)	1.6(2)
O$_1$	0.0946(11)	1/4	0.7403(21)	1.7(4)	0.1153(9)	1/4	0.7107(20)	1.6(4)
O$_2$	0.4538(13)	1/4	0.2056(15)	0.6(3)	0.4450(12)	1/4	0.1511(16)	0.2(3)
O$_3$	0.1615(8)	0.0521(12)	0.2861(11)	0.9(3)	0.1649(7)	0.0465(11)	0.2520(11)	0.4(2)

Table 2.1 Atomic and unit cell parameters for LiFePO$_4$ and FePO$_4$ obtained *via* Rietveld refinement of the X-ray powder diffraction data [36].

Additionally, as the oxygen atoms are strongly covalently bonded by phosphorus atoms in the (PO$_4$)$^{3-}$ clusters (calculated interactomic distance is $r_{P\text{-}O}$ = 1.512 Å [36]), the structures of both LiFePO$_4$ and FePO$_4$ are stable under oxygen and nitrogen atmospheres even at high temperatures (up to 350 ^{o}C). This results in excellent operation safety of LiFePO$_4$. Furthermore, there is no evidence of potentially troublesome reactions between the commonly used electrolyte and LiFePO$_4$ under charged and discharged conditions up to 85 ^{o}C, guaranteeing no O$_2$ release and no likely pressure build-up inside the battery.

However, it is well known that Fe^{2+} in LiFePO$_4$ can be quite unstable under oxygen and water, as it is the case in the atmospheric air. As a result, long-term air exposure of LiFePO$_4$ can lead to severe oxidation (Fe^{2+} to Fe^{3+} conversion on the surface of the particles) limiting its electrochemical performance [37].

This problem could be resolved by employing full carbon coating of $LiFePO_4$. However, most recent reports show that even $LiFePO_4$/C composite can react with air and form $Li_xFePO_4(OH)_x$, an intermediate between olivine and tavorite, due to moisture-driven aging [38]. If this is the case, additional heat treatments are necessary for the recovery of the pristine structure in air-aged materials.

2.3 Electrochemical properties of $LiFePO_4$

In the first electrochemical tests, it has been shown that the galvanostatic Li^+ charge/discharge curve of $LiFePO_4$ is very flat at V_{oc} = 3.45 V over a large composition range [34]. This suggests two phase Li^+ intercalation/deintercalation mechanism,

$$LiFePO_4 \leftrightarrow xFePO_4 + (1-x)LiFePO_4 + xLi^+ + xe^- , \tag{2}$$

and excellent cycling stability since the voltage lies in the energy window of presently used carbonate electrolytes. First obtained capacity of $LiFePO_4$, however, was only 110 mA h g^{-1} at low current densities and high constant temperature of cycling (300 ^oC). Also, the reversible capacity decreased rapidly with increased current density. Further studies proved that the limiting process in Li^+ ion intercalation/deintercalation in $LiFePO_4$ is diffusion-controled, with a combination of low Li^+ ion phase-boundary diffusion and low electronic conduction in end phases, preventing the full conversion between $LiFePO_4$ and $FePO_4$ [36, 39].

The diffusion coefficient of Li^+ ion has been measured by various techniques (e.g., galvanostatic intermittent titration technique, electrochemical impendance spectroscopy and systematic cyclic voltametry) and all of the obtained values (10^{-10} – 10^{-16} cm^2 s^{-1}) were much lower than those of the layered $LiCoO_2$ (5 x 10^{-9} cm^2 s^{-1}). However, the performed electrochemical experiments could not distinguish between the mass transfer in the bulk and across the surfaces; therefore, computational predicaments needed to be employed. Calculations based on first principles [40] and atomistic calculations of ionic conductivity [41] showed that the Li^+ ion diffusion is most probably occurring only through 1D channels along the *b*-axis in the [010] direction with low possibility of crossing through channels as schematically shown in Figure 2.2.

This is, however, a serious structural constraint, and the depicted 1D channels can easily be blocked by impurities or defects, thus lowering the ionic diffusivity and the availability of the active volume. Typically found lattice defects in $LiFePO_4$ are Fe/Li point defects (Fe^{2+} ions occupy the M1 sites instead of Li^+ ions), further impeding Li^+ ion diffusion and leading to structural instability due to electrostatic repulsion induced by high valence. Therefore, suitable synthesis method needs to be developed for obtaining highly pure and defect-free $LiFePO_4$.

The electronic conductivity of $LiFePO_4$ is ≈1 x 10^{-9} s cm^{-1} at room temperature which is incomparably lower than of the layered $LiCoO_2$ [42]. This highly limits the electron transfer through the material and employment of additional electronically conductive material as an additive is a necessity to enhance the kinetics of $LiFePO_4$ electrochemical reactions.

To address the ionic and electronic conductivity related problems in $LiFePO_4$ used as lithium-ion battery cathode material, various approaches and their combination have been used:

(i) downsizing the particles for reducing the lengths of ionic and electronic transport [43-45];
(ii) surface modification by coating with conductive agents, mainly carbon [46-50];
(iii) selective doping with supervalent cations to increase the intrinsic conductivity [42, 51] ;
(iv) morphological (introducting porosity) and textural (crystal orientation) tuning [52-55].

2.3.1 Li+ intercalation/deintercalation mechanism

The mechanism of Li^+ intercalation/deintercalation in the $LiFePO_4$ has not been completely elicited. In the first electrochemical studies, Padhi *et. al.* [34] proposed a *"shrinking-core" model*. According to this model, the core of one phase is covered with a shell of a second phase while Li^+ ion proceeds from the surface of the particle to the core, simultaneously moving the two phase interface. This model was confirmed by Srinivasan *et. al.* [56] by measuring the continuous deviation of the V_{oc} from 3.45 at the initial start and the end of discharge (curvature of the voltage-composition profile). The V_{oc} deviation suggested that there could be a corresponding single phase region outside the two-phase coexistence region. Figure 2.3 is an illustration of the discharge process in a "shrinking-core" model: after a small fraction of Li^+ ion intercalates into the lattice (α), further insertion results in phase separation with the formation of new Li-rich phase (Li content of $1-\beta$, β can be expected to be close to zero). With the proceeding lithiation at the surface of the particle, more Li^+ ion is inserted into the lattice and then transported to the Li-deficient core through the Li-rich shell, leading to further phase separation and core shrinkage. The process is reversible upon charge. In recent years, experimental results (HR-EELS, HR-TEM) have invalidated this model.

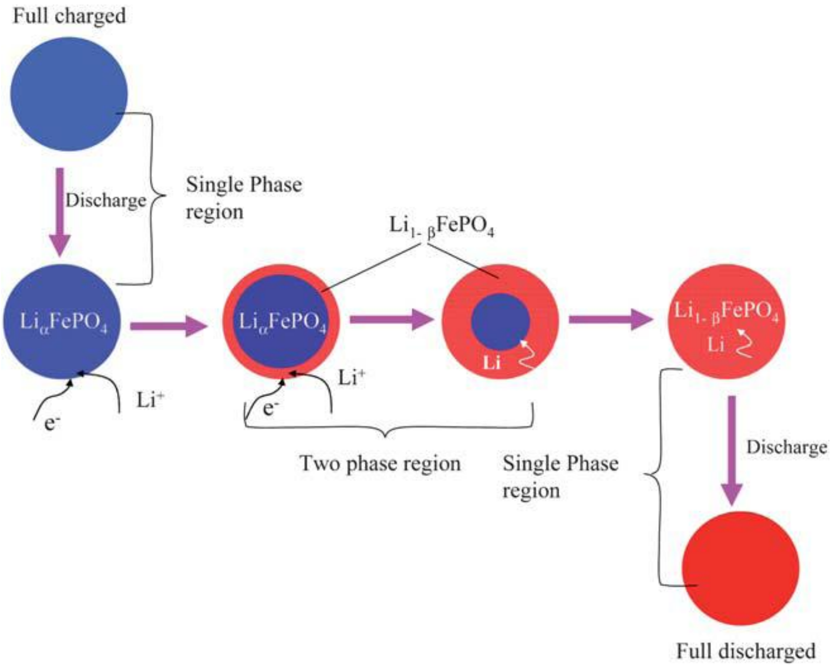

Figure 2.3 Schematic representation of "shrinking-core" model for Li^+ discharge process of $LiFePO_4$ [56].

Laffont *et. al.* [57] proposed a *"new core-shell" model* according to which the Li^+ ion migration in [010] channels is asynchronous and the $LiFePO_4/FePO_4$ system both during charge and discharge keeps the same structure with a $FePO_4$ shell and a $LiFePO_4$ core. The limitation of the core-shell model and its improved version is that these models give an over-simplified image of the intercalation/deintercalation process and do not take into account the anisotropy arising from the fact that ion and electron motion in $LiFePO_4$ are constrained by the olivine structure itself.

Delmas *et. al*. [58] developed a *"domino-cascade" model* which takes in account structural constraints as well as the influence of the reaction interface (Figure 2.4). The minimization of the elastic energy due to structural constraints enhances the intercalation/deintercalation process that as a result occurs as a wave moving through the entire crystal. The "domino-cascade" model claims that the speed of the phase boundaries is extremely high so that no particles with the mixing phases can be identified during reaction process; therefore, single particles are either $LiFePO_4$ or $FePO_4$.

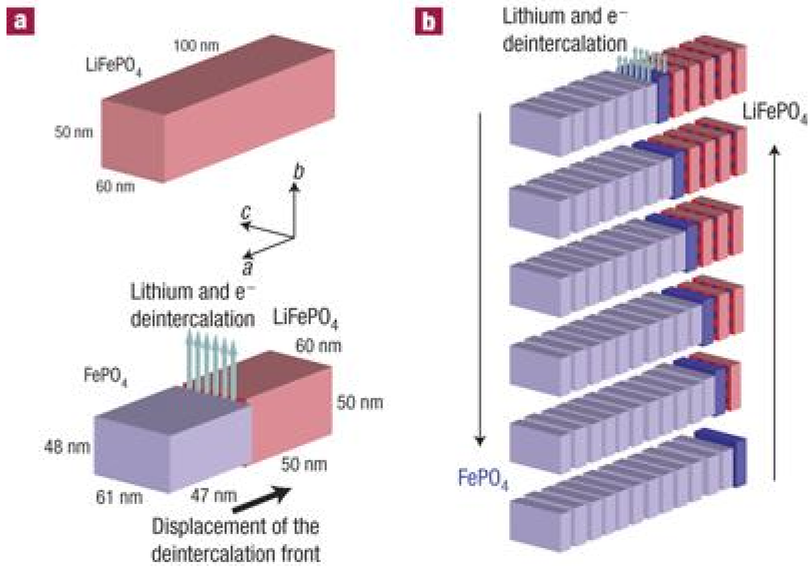

Figure 2.4 Schematic representation of "domino-cascade" model of Li^+ intercalation-deintercalation in $LiFePO_4$ [58].

Finally, Ramana *et. al.* [59] introduced a *"spinodal-decomposition" model* which suggests that the movement of the phase boundaries is relatively slow and multiple domains and phase interfaces should be observed in the partially delithiated particles.

Besides the peculiarities of each Li^+ intercalation/deintercalation model, there is a general agreement that Li^+ ions move in the tunnels along the *b*-direction and are extracted /inserted at the interface (phase boundary) where $LiFePO_4$ and $FePO_4$ crystalline structures coexist. According to different models, the phase boundary can lie in the *b*-*c* plane or in the ([110], *c*) plane and can finally govern the dynamic of the process. It is important to note that the Li^+ insertion/extraction processes appear to depend on the particle size, synthesis method, surface coating, charging rate and testing procedures [60]. Thus, more controlled studies are needed to understand the intercalation/deintercalation mechanism under real operation conditions using novel advanced *in situ* characterization tools.

2.3.2 The effect of carbon coating

Carbon coating is the most efficient way to improve the electronic conductivity and low rate capability of $LiFePO_4$ materials. When synthesized *in situ*, it offers intimate contact between inorganic and organic phase, where carbon acts as an electronic wiring system interconnecting $LiFePO_4$ particles. Since the pioneering work of Armand *et al.* [46], various kinds of organic carbon compounds have been used as precursors, such as glucose [61-64], sucrose [65, 66], citric acid [52, 67], carbonaceous polymers [45, 68] or even carbon containing inorganic precursors (oxalate, acetate, carbonate, citrate) [69].

The electrochemical properties of the final $LiFePO_4$/C composites are strongly dependent on the quality of the carbon coating – its amount, morphology, degree of graphitization, and the distribution on the surface [60]. The general opinion is that the optimal carbon content is 5-10 wt %. In some cases, too much carbon precursor can lead to undesirable impurities such as Fe_2P [70], while too much carbon in the final material reduces volumetric energy density.

Also, it was concluded by researchers that sp^2 (graphitized) carbon is much more effective than sp^3 (disordered) carbon for the Li^+ diffusion throughout the $LiFePO_4$ particle. The sp^2/sp^3 ratio is usually determined by Raman spectroscopy and X-ray photoelectron spectroscopy analysis [71].

The carbon coating on $LiFePO_4$ should preferably be thin (order of couple of nm), uniform and homogeneous so that the particles can get electrons from all directions and the Li^+ ion can penetrate through it without high polarization. Additionally, such carbon coating acts as a reductant to avoid the formation of undesirable Fe^{3+} and related impurities as well as a nucleating agent to decrease the particle size [68, 70]. It has also been reported that carbon can change the surface conditions of $LiFePO_4$ by controlling the spin of iron ions in the amorphous surface layer [72].

Carbons chemically doped with phosphorus, boron and nitrogen have recently attracted a surge of attention in the scientific community due to their specific properties, such as improved electronic conductivity arising from the possible overlapping of the conduction and valence bands. Recently, nitrogen doped carbons showed remarkable behavior in the field of electronics and rechargeable batteries [73-75]. Hydrothermally carbonized nitrogen-containing carbons from chitosan and N-acetlyglucosamine synthesized in the group of Dr. Maria-Magdalena Titirici (Max Planck Institute of Colloids and Interfaces) showed improved conductivity in comparison to the non-nitrogen containing counterparts [76]. Thus, one of the new ideas introduced in this thesis is coating of $LiFePO_4$ using nitrogen-containing carbon precursors with a possibility of further enhancing conductivities of final materials.

2.4 Synthesis of $LiFePO_4$

Although $LiFePO_4$ is a natural mineral found in the earth's crust known as tryphilite, mining of large quantities of highly electrochemically active, pure and morphology-controlled powder is not possible. Therefore, adequate large-scale, low-cost and eco-efficient synthetic technique needs to be developed. Most of procedures used for synthesizing $LiFePO_4$ can be divided into solid-state reactions and solution chemistry reactions [77].

$LiFePO_4$ has been firstly synthesized using conventional *solid-state method*, previously widely employed for producing ceramic materials. This method consists of several successive steps of intimate grinding and annealing of the stoichiometric mixtures of starting materials (iron source: Fe(II) acetate or Fe(II) oxalate; lithium source: Li_2CO_3 or LiOH; phosphorus source: $(NH_4)_3PO_4$) [34, 42, 59, 78, 79]. In the first step, the starting materials are decomposed at 200 ^oC (releasing NH_3) and at 300 ^oC (releasing CO_2). Following this step, the products are reground and calcined at temperatures ranging from 400 to 800 ^oC for 10 to 24 h. Cheaper Fe (III) compounds (Fe_2O_3, $FePO_4$) can also be used as iron precursors; however, reductive atmosphere (Ar + H_2) is then needed throughout the procedure in order to produce Fe^{2+}-rich $LiFePO_4$. The purity of the final material depends on the growth parameters, including: temperature of calcination and exposure time. The main disadvantages of solid-state method include easy formation of Fe^{3+} and its compounds (Fe_2O_3, $Li_3Fe_2(PO_4)_3$), due to presence of residual air (oxidation of Fe^{3+}), as well as uncontrollable particle growth and agglomeration, resulting in non-pure final materials with limited surface area and non-satisfying particle size distribution.

To overcome the stated problems, *mechanochemical activation* was introduced into the solid-state process. As a result of ball-milling in a high-energy vessel, the powder undergoes intimate mixing with continuous renewal of precursor contact surfaces and very small, homogeneous particles with large surface area are obtained. However, a thermal treatment at moderate temperature is needed together with mechanochemical activation to obtain phase-pure $LiFePO_4$ (short-time milling followed by long-time thermal treatment or long-time milling followed by short-time thermal treatment).

This type of synthesis yields powders with good electrochemical behavior since it is suitable for preparation of both $LiFePO_4/C$ composites (by adding carbon precursor into the primary mixture) as well as doped $LiFePO_4$ materials [42, 80].

By adding stoichiometric amounts of carbon to the solid-state precursors and subsequent *carbothermal reduction*, Fe (III) compounds as iron sources can be used in the synthesis of $LiFePO_4$ without the risk of Fe^{3+}-compounds forming. Nevertheless, carbothermal reduction requires very high processing temperatures in order to synthesize pure $LiFePO_4/C$ composite (900 ^oC). Lower temperatures (700 ^oC or even 400 ^oC) can be used only in the case of polymer as carbon source, where pyrolytic degradation occurs instead of carbothermal reduction [68].

A variety of such solid-state methods have been adopted for scaled-up production of $LiFePO_4$ by different companies such as A123 System Inc. [81], Valence Technology Inc. [82] and Sony Corp. [83]. However, the need for repeated calcinations and grindings makes such procedures time and energy-consuming, and thus probably unsustainable in the longer run. As already stated, solid-state methods are limited in controlling the particle size and agglomeration, resulting in irregular morphologies of $LiFePO_4$.

Compared to solid-state methods, solution chemistry routes such as: hydrothermal/solvothermal, sol-gel, co-precipitation, spray-pyrolisis, emulsion-drying and novel ionothermal route, are capable of tailoring the size and morphology of $LiFePO_4$ powders which is important for the electrochemical performance. All of the solution routes start from a precursor in a liquid solution which provides intimate mixing of the ingredients on atomic level, leading to rapid homogeneous nucleation and uniform particle formation. A wide range of iron reactants are available for this synthesis type, including sulfates and chlorides which are not suitable for solid-state reactions due to removal problems. In all solution methods, most of the reactant and reaction produced impurities can be easily removed by washing which lowers fabrication costs (reactants of lower purity can be used). Similarly to the solid-state route, some of the solution methods require further calcinations of obtained materials at high temperature for a certain amount of time in order to enhance crystallinity or to better control of the Li/Fe positions in the $LiFePO_4$ lattice. Here on, only the most commonly used solution methods will be discussed.

Hydrothermal synthesis was used for the production of mineral species in hydrometallurgy as early as in the 19th century. The technique was widely accepted for the synthesis of zeolites in 1940s and has been introduced for practically all inorganic species from oxides, silicates, phosphates to carbonates in 1960s [84]. Hydrothermal reaction is usually held in a closed vessel called autoclave (Figure 2.5). By using reaction's inherent pressure which develops when the temperature is raised above 100 ^oC, the precipitation kinetics and growth *via* Ostwald ripening of favorable material phases can be controlled.

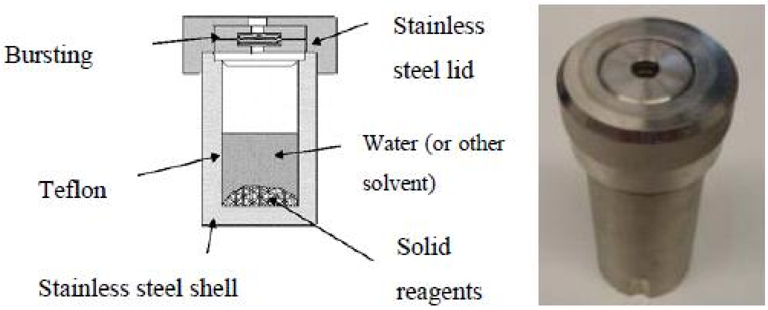

Figure 2.5 Schematic representation and a photograph of an autoclave [85].

$LiFePO_4$ was firstly synthesized hydrothermally at 120 ^oC in the group of Whittingham [86] in 2001 using the following reaction:

$$H_3PO_4 + FeSO_4 + 3LiOH \rightarrow LiFePO_4 + Li_2SO_4 + 3H_2O. \qquad (3)$$

Hydrothermal synthesis has later been improved by other researchers and became the most common way to produce nanostructured $LiFePO_4$ [44, 87, 88]. However, the electrochemical capacity of the firstly synthesized hydrothermal $LiFePO_4$ was rather low due to high Li/Fe disorder (7%, calculated by XRD Rietveld analysis) and the presence of small amount of Fe^{3+}-related compounds in the final material [86]. The solution for the cation disorder problems was the post-firing of the material at 700 ^oC or higher temperatures in inert atmosphere or employing higher temperatures synthesis procedures (over 175 ^oC) [78]. Additionally, by using the hydrothermal method, it was possible to obtain samples with high surface areas by employing surfactants such as hexadecyl-trimethylammonium bromide (CTAB) [89].

Solvothermal method uses the same principles as hydrothermal method (autoclave treatment at (180 – 200 ^oC), employing different organic solvents and solvent mixtures (*e.g.* tetraethyleneglycol [44, 90], benzyl alcohol [91], ethylene glycol [92] and polyethyleneglycol-water mixture [93]) which can then act as stabilizers to allow the control of particle growth (morphology, size and texture) and iron oxidation state.

Ionothermal method is a special type of solvothermal approach recommended by Tarascon *et al.* [94]. It is based on the special solvent characteristics of ionic liquids such as high thermal stability, negligible volatility and tunable solvation properties depending on the cation-anion pairs they are made of. By employing relatively mild temperatures (250 – 280 ^oC), nanostructured, highly crystalline $LiFePO_4$ was obtained.

Sol-gel method for the synthesis of $LiFePO_4$ has been developed by Dominko *et. al.* [69] in order to obtain materials of higher purity, better homogeneity (optimized carbon distribution), internal porosity and at lower temperatures in comparison to the traditional ceramic methods. This method was firstly used for fabrication of metal oxides and consists of transformation of a sol (dispersion of colloidal particles in a solution) to a gel (integrated rigid network of particles) *via* drying and solvent evaporation. In the case of $LiFePO_4$, a variety of solvents (N,N-dimethylformamide, water with ascorbic or citric acid [95], ethylene glycol, ethanol) and iron precursors (Fe(II) oxalate, Fe(III) citrate) have been used to obtain a sol which was then dried until solvent evaporated and calcined at temperatures ranging from 500 ^oC to 700 ^oC under argon/nitrogen atmosphere to retrieve porous $LiFePO_4$/C material.

Most recently, as a step forward from the standard solid-phase/solvothermal routes, the group of Prof. Angela Belcher at Massachusetts Institute of Technology developed genetically engineered high-power $LiFePO_4$ using multiple virus genes [96, 97]. Using biological systems, the formation of α-$FePO_4$ nanoparticles was templated. This route offers a completely new approach towards fabrication of $LiFePO_4$ and other lithium-ion battery electrodes (Figure 2.6).

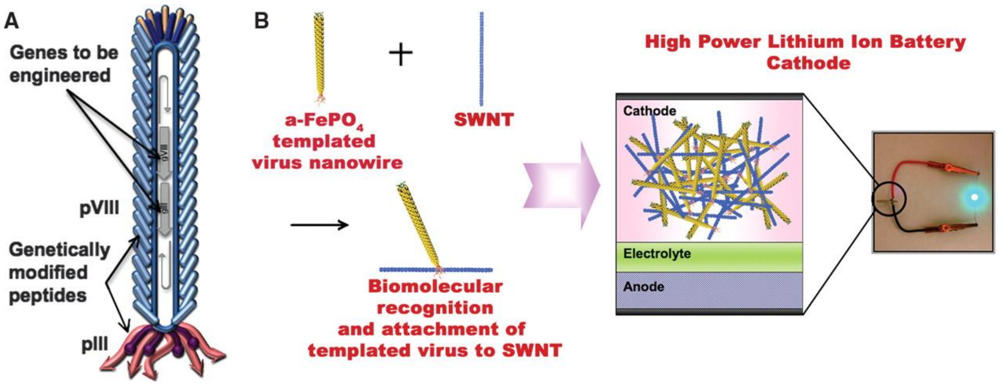

Figure 2.6 Schematic representation of biological toolkits (A, B) used for template-based synthesis of FePO$_4$ and attachment of single-wall nanotubes [97].

Obviously, the main synthetic challenges for LiFePO$_4$ are the control of impurities combined with eco-efficiency of the processes. Some impurities, such as Fe$_2$P, not only can enhance the electrochemical performance of LiFePO$_4$ due to their high conductivity but also can diffuse into the electrolyte. On the other hand, most of the likely occurring impurities (Li$_3$Fe$_2$(PO$_4$)$_3$, Li$_2$P$_2$O$_7$, FeP, FePO$_4$) appear in LiFePO$_4$ depending on the precursor, preparation mode and growth parameters and cause non-satisfying electrochemical behavior. Although many routes have been used to prepare LiFePO$_4$ on the lab scale, commercial production of LiFePO$_4$ still relies on solid-state methods which require expensive pure reactants and high temperatures with low morphological control.

Hydrothermal/solvothermal synthesis stays the most promising alternative since it is easily up-scalable, simple, eco-friendly and offers the possibility to produce different LiFePO$_4$ morphologies.

2.5 Summary

This chapter offers a brief introductory overview of Li-ion batteries with focus on the structure, electrochemical properties and available synthetic methods for producing $LiFePO_4$ cathode materials. It was pointed out that currently used cathodes ($LiCoO_2$) cannot be employed for the new generation of electric vehicles (EVs) and hybrid electric vehicles (HEVs) due to their limited capacity, possible battery explosion, toxicity and high production cost. Thus, $LiFePO_4$ was introduced as a potential replacement for $LiCoO_2$, due to its attractive properties such as: comparably higher capacity, high safety, possible low cost of production and environmental compatibility.

$LiFePO_4$ has olivine orthorhombic 3D structure, and is a stable compound with a reversible Li^+ intercalation/deintercalation mechanism through 1D chanells along the *b*-axis accompanied by mild volume changes. However, major downfall of $LiFePO_4$ lies in its low values of ionic and electronic conductivity. In order to obtain good electrochemical performance and cyclability the $LiFePO_4$ particles need to be either small or porous (morphology control). Furthermore, it needs to be either doped or coated with electronically conductive agents. Carbon coating turned out to be the most efficient way to enhance its electronic conductivity and thus the electrochemical performance. The coating thickness, chemical structure, uniformity and final morphology, are crucial parameters for the good electrochemical behavior of $LiFePO_4$.

Solid-state reactions are still the most commonly used method for commercial production of $LiFePO_4$. However, they rely on harsh temperature conditions ($\approx 1000\ ^oC$) and multiple-step procedures resulting in bad morphological control and unpurified final powders. Hydrothermal/solvothermal reaction on the other hand has been proven as a better solution, offering the possibility to use cheaper precursor materials, lower working temperatures ($\approx 200\ ^oC$) and leading to better morphology control and higher crystallinity.

As a consequence of the here presented state of the art, the subject of this PhD thesis revolves around the development of a new solvothermal route for producing promising $LiFePO_4$ morphologies in combination with the introduction of nitrogen containing carbon coatings for superior electrochemical properties.

3 Analytical methods

3.1 X-ray diffraction

X-ray diffraction involves measuring of the intensity of X-ray scattering from electrons bound to atoms in crystalline materials. As source-generated X-ray waves propagate the substance (electro-magnetic waves, λ from 0.1 to 5 Å), they get coherently, and elastically scattered at atoms at different positions. This behavior can be recorded by a detector and as a result, discrete intensity maxima are obtained as a function of a single independent variable – the Bragg angle. Such diffraction pattern is a snapshot of the 3D reciprocal lattice of a crystal. Thus, X-ray diffraction experiments are essential for performing diffraction analysis, basic materials characterization technique dealing with transformation of reciprocal space to real space and phase identification [98].

The theory of X-ray diffraction is based upon the well known Bragg law which establishes a geometrical relationship between the diffraction angles (Bragg angles, θ), wavelength (λ) and interplanar spacing in a crystalline lattice reflecting X-rays (d_{hkl}):

$$2d_{hkl} \sin \theta = n\lambda \text{ [99].} \tag{1}$$

Bragg's equation treats X-rays as visible light and its reflection is visualized as mirror-like on a series of crystallographic planes with identical Miller indices (*hkl*). The crystallographic planes in such an ideal crystal are considered as separate scattering objects with equal interplanar distance d_{hkl}. This association allowed the first structural solutions of NaCl and diamond.

A better visual representation of the phenomena of diffraction in reciprocal space was introduced by Ewald [100]. A sphere of radius 1/λ is constructed using incident wave vector s_0 and scattered wave vector s which terminates at a point on the sphere's surface (Figure 3.1a). The two vectors are connected by a scattering vector $d^* = s\text{-}s_0$. Bragg's law is satisfied when there is a reciprocal lattice point on the surface of the sphere in which vector d^* terminates. Thus, any vector between these two lattice points can produce a Bragg peak in a diffraction pattern.

However, in the 3D space and in the case of polycrystalline material, the circular intersection of the reciprocal lattice with the Ewald's sphere results in the diffracted X-rays forming coaxial cones, the so-called Debye-Scherrer cones (red and green dashed lines, Figure 3.1b) and associated rings.

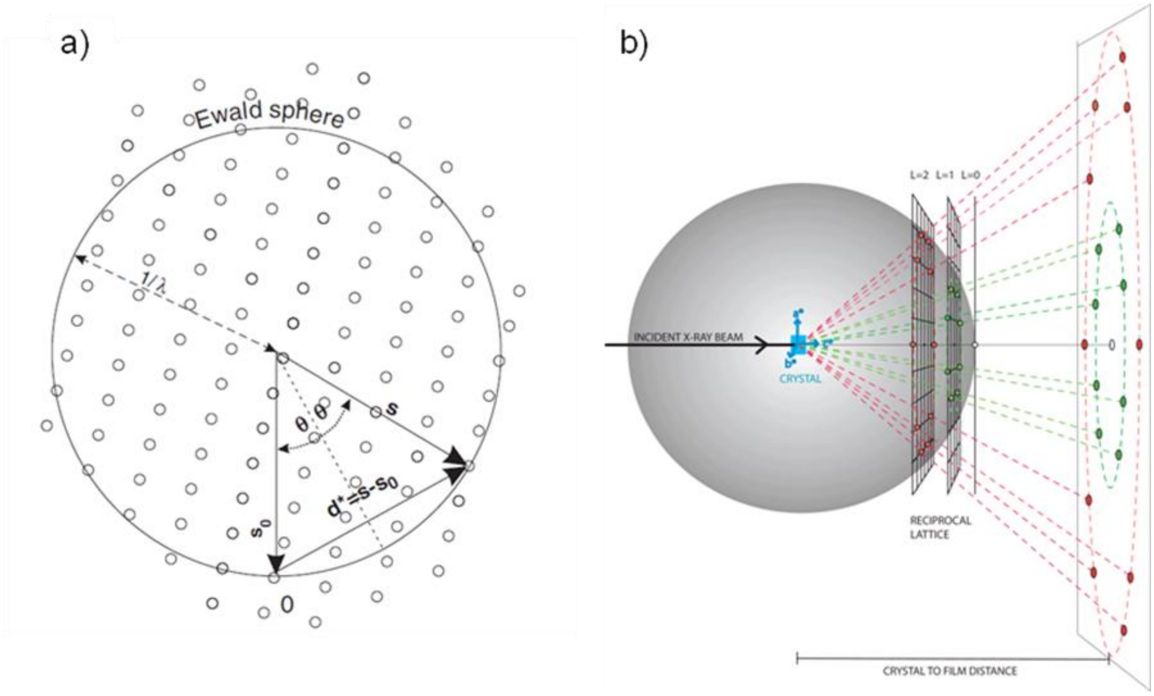

Figure 3.1 Visualization of the diffraction using Ewald's sphere: a) two-dimenstional projection (0 marks the beginning of the reciprocal space) [101], b) three-dimensional projection indicating Debye-Scherrer cones and rings.

Since 1970s, automated powder diffractomers have been used as analytical instruments for X-ray diffraction. The majority of these instruments are based on Bragg-Brentano self-focusing geometry, as shown in Figure 3.2. In such an environment, the sample is placed on a flat plate (preferably horizontal orientation) in the center of the goniometer dotted circle. The incident X-rays produced by a standard anode tube pass through at least two slits before reaching the sample in order to improve the diffracted intensity and resolution. Powder diffractometers usually operate in the θ-2θ scanning regime where both, the incident and the diffracted, beams form the same angle θ with the surface of the sample, while the diffracted beam forms 2θ angle with the incident beam. The diffracted beam is monochromatized and recorded by a detector. The critical part of the powder diffractometer hardware is the goniometer and its alignment. In addition, the sample preparation plays an important role in the quality of X-ray diffraction data (fine powders with particle size under 50 µm are needed).

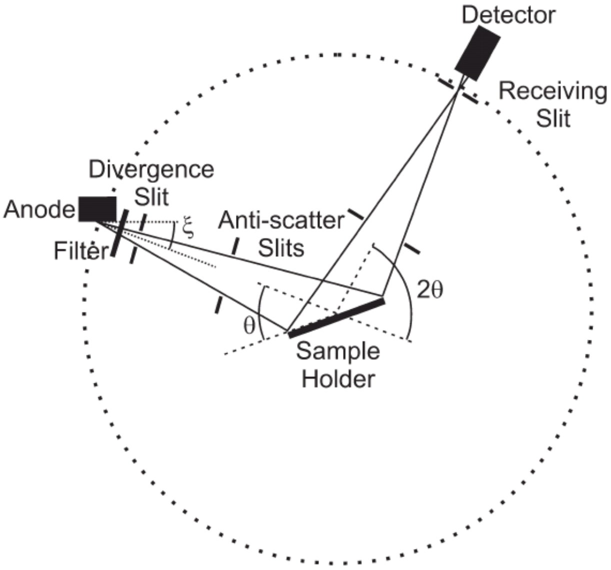

Figure 3.2 Schematic representation of Bragg-Brentano geometry used in a common powder diffractometer [101].

The structure of a typical powder diffraction pattern obtained by X-ray diffraction measurement can be described by the positions, intensities and the shapes of multiple Bragg reflections which contain information about the crystal structure of the material (unit cell parameters *a*, *b*, *c*; atomic parameters *x*, *y*, *z*; crystallinity; disorder; defects). In this thesis, a material with an orthorhombic crystal structure has been characterized. Thus, permissible Bragg angles and interplanar distances can be found by following equations:

$$2\theta_{hkl} = 2\arcsin\left(\frac{\lambda}{2d_{hkl}}\right), \text{where } d_{hkl} = \left(\frac{h^2}{a^2}+\frac{k^2}{b^2}+\frac{l^2}{c^2}\right)^{-1/2}. \tag{2}$$

When available, Bragg peak positions coupled with known *hkl* triplets taken from a literature reference or a database (The International Center for Diffraction Data Powder Diffraction File) can be used instead of the calculated ones. On the other hand, the peak intensity is a function of the periodicity of the unit cells and can give information on the preferred crystal orientation. The shape of the Bragg peaks is usually represented by a bell-like function which is weakly dependent on the crystal structure and is obtained by deconvolution of various individual functions established by some instrumental parameters [98].

For the final evaluation of the X-ray diffraction patterns, Le Bail method of full profile matching has been used in this thesis [102]. This method is a variation of the Rietveld method in which the intensity observed in every point of the X-ray diffraction pattern is divided among different reflections proportionally to their calculated intensities:

$$y_{k,i}^{obs} = p_{k,i}\left(Y_i^{obs} - b_i\right), \tag{3}$$

$$\text{where } p_{k,i} = \frac{y_{k,i}^{calc}}{\sum_{k=1}^{m} y_{k,i}^{calc}}, \text{ and } 1 \leq i \leq n \text{ [6].}$$

In Eq. (3), $y_{k,i}^{obs}$ is the pseudo-observed intensity of the kth Bragg reflection in the ith point, Y_i^{obs}, the observed total intensity in the ith point, b_i, the background and $p_{k,i}$ is the fractional distribution of the kth Bragg reflection to the ith point. The total number of measured data points, *n*, is usually modeled by a polynomial function. The main difference between Le Bail and Rietveld model resides in the fact that Le Bail method uses the intensities calculated from the previous cycle during the decomposition of the X-ray diffraction pattern, while the later model employs intensities calculated from the crystal structure. For both models, the unit cell parameters are set at the beginning of the pattern decomposition. Using Le Bail or Rietveld method, subtle anomalities of Bragg reflections can be connected to the structural details of the characterized materials.

3.2 Electron microscopy

The resolution r_d of any optical system is the diffraction limit imposed by the wavelength of the radiation, λ, the aperture angle of the objective lens, α, and the refractive index, n, and can be formalized through the Abbe's equation:

$$r_d = \frac{k\lambda}{n sin\alpha}. \tag{4}$$

Thus, the resolution in an optical microscope is restricted by the wavelength of the visible light which prevents atomic-scale imaging. On the other hand, electrons have a De Broglie wavelength of less than 1 Å, such that enormous improvement in resolution can be achieved by using a beam of fast electrons for imaging.

Previously described geometrical diffraction theory (Bragg law, Ewald's sphere construction) is also applicable to electron diffraction. However, the interaction between the specimen and electrons is considerably stronger and more dynamical in comparison to the interaction with X-rays.

3.2.1 Scanning electron microscopy (SEM)

The first SEM was developed by Knoll in 1935 and since then is one of the most used electron microscopy instruments. In SEM, the specimen is probed by a beam of electrons scanned across the surface revealing its morphology, 3D microstructure, roughness, cracks and cavities.

A typical SEM microscope consists of a microscope column (electron gun, one or two condenser lenses, objective lens and some apertures) and an electronics console. The detector and specimens are located in an evacuated specimen chamber (pressure $\approx 10^{-4}$ Pa). The electronics console consists of the electric power supplies for the needed acceleration voltage, electronic amplifiers and monitors. As the focused beam of electrons enters the specimen, the electrons get elastically scattered emitting secondary electrons which then can be detected by a weak electric field. The electron detector counts the number of secondary electrons that arrive per unit of time and transforms this count rate into an electronic current synchronically to the scanning electron beam. The topography of the samples can be observed due to the fact that the edges and convex surfaces of the samples facilitate the release of secondary electrons (higher probability to break away from from the surface) and appear brighter, rendering the observed picture three dimensional. The electron beam negatively charges the specimen; therefore, the non-conductive specimens need to be sputtered with a conductive material prior to measurement [103].

3.2.2 Transmission electron microscopy (TEM)

The overall process in the formation of TEM image is similar to the one obtained by light microscopy and involves electron scattering in the nuclei of the specimen, formation of the diffraction pattern in the back focal plane of the objective lens and formation of an image in the image plane, as shown in Figure 3.3. The transformation from reciprocal space to the real space is given mathematically by the Fourier transform.

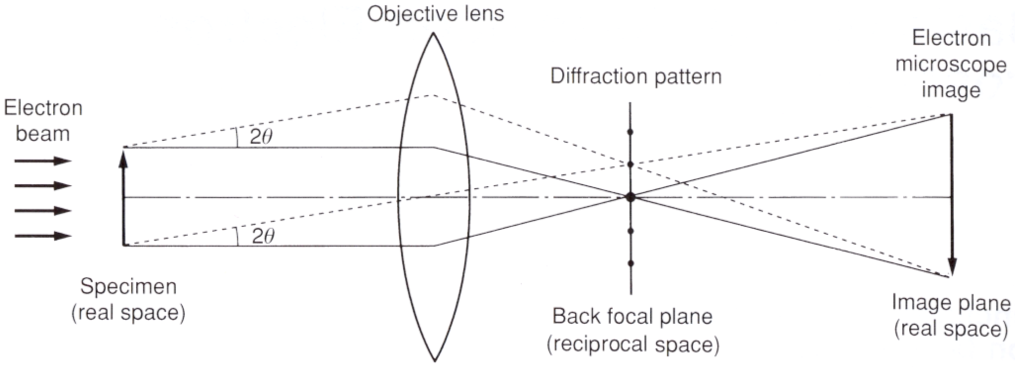

Figure 3.3 Schematic optical ray diagram showing the principle of the imaging in a TEM [104].

The first TEM instrument was built by Ernst and Ruska in 1931 and usually consists of an electron gun, two stage condenser lenses which permit the variation of the illumination aperture, three- or four- stage lens system behind the specimen and digital charge-coupled detectors or TV cameras inside a high vacuum chamber. TEM can operate in image mode (bright field/dark field) or diffraction mode depending on whether the aperture is placed under or above the specimen. Since the electrons interact strongly with atoms by elastic and inelastic scattering, the specimen must be very thin. Consequently, the elements of higher atomic number appear darker in TEM micrographs due to high absorption [103].

High-Resolution Transmission Electron Microscope (HR-TEM) on the other hand is capable of giving resolutions on the picometer scale due to the highly stable electron acceleration voltage and operability on the fixed current. While elastically scattered electrons mainly contribute to the high-resolution bright-field image, inelastically

scattered electrons can provide valuable information about the specimen's composition *via* coupled Electron Energy-Loss Spectroscopy (EELS).
Additionally, the specimen's atomic composition can be detected from the X-rays produced when the electron probe interacts with the specimen *via* a coupled Energy Dispersive X-ray (EDX) detector. Important applications of HR-TEM include the following: determining the microstructure of crystalline defects, interfaces and grain boundaries and studying small particles in heterogeneous catalysis [105].

In this thesis, TEM and HR-TEM were used to investigate the morphology, lattice fringes, carbon coating, crystallinity and atomic composition of the synthesized $LiFePO_4$ materials.

3.3 Li^+ insertion/extraction

The specific capacitance of the potential Lithium-ion battery cathode material is usually determined by electrochemical galvanostatic charge/discharge technique [106]. In this method, Swagelok® cells (Figure 3.4) are assembled in the Argon-filled glove box by using a known weight of active cathode material, mounted on a potentiostat and cycled galvanostatically using different currents.

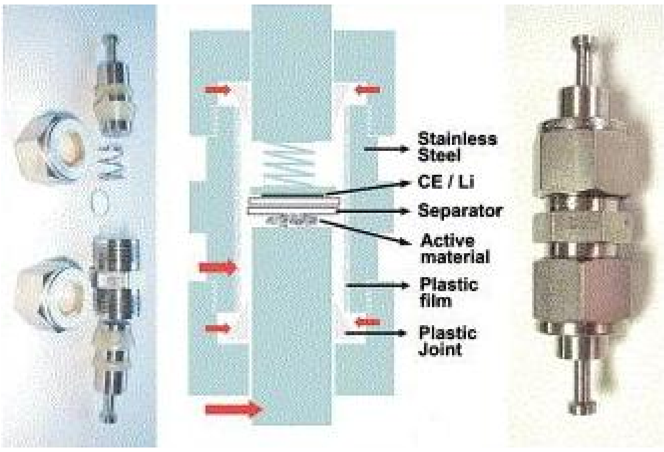

Figure 3.4 Schematic representation and a photograph of a Swagelok® cell [107].

The selected current rates, the so-called *C*-rates, should correspond to the utilization of theoretically calculated specific capacity in various time spans (e.g., 2, 5, 10 hours).

The cut-off voltages used for measurements are adapted according to the type of measured cathode material. It is important to note that materials that can be cycled at high *C*-rates and operating in the voltage window of commercially used electrolytes are desirable.

During galvanostatic cycling, structural change occurs inside electrode material as a result of Li^+ insertion/extraction (Lithium metal is used as a counter electrode - anode). The results form obtained measurements can be plotted in galvanostatic charge/discharge curves (voltage vs. capacity, voltage vs. composition as shown in Figure 3.5 and capacity vs. cycle number). Important parameters that can be determined from these curves are specific capacity, voltage, and reversibility (e.g., polarization, voltage gap between charge and discharge).

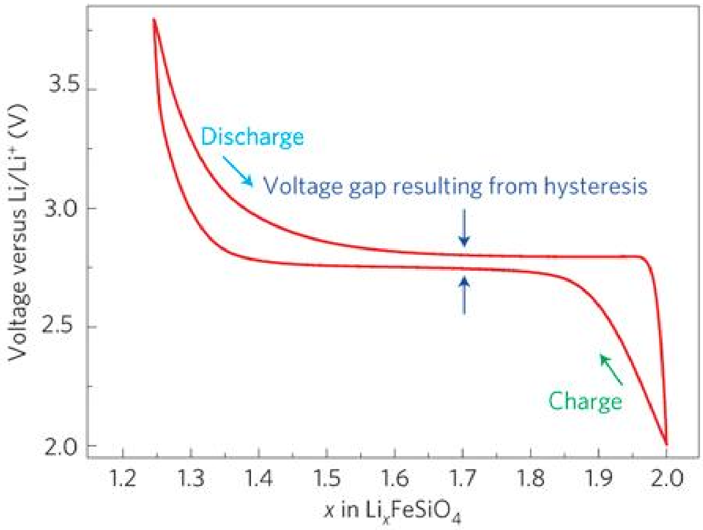

Figure 3.5 Typical galvanostatic charge-discharge curve of $LiFeSiO_4$ at a C/20 rate [108].

In order to assess the rate capability of a cathode material, additional galvanostatic measurements are usually performed in which the *C*-rates are varied after a certain number of cycles. The results are plotted in a specific capacity vs. cycle number diagram.

4 Synthesis of LiFePO$_4$ mesocrystals

4.1 Introduction

Mesoscopically structured crystals (abbreviated mesocrystals) as described by Cölfen *et. al.* [109-112] are 3D-ordered superstructures formed *via* the non-classical particle mediated crystallization pathway. These specific morphologies are composed of a few to thousands of nanoscaled hierarchically self-assembled primary units (1-1000 nm in size) and appear as single crystalline, isooriented structures with or without organic additives as defects. Mesocrystals have been firstly reported in biominerals (nacres, corals, sea urchins) which are evolutionary highly optimized “real-life” structures, exhibiting curvature as a common feature despite their single crystal properties [113-116]. Recently, evidence of crystal growth by oriented aggregation has been frequently observed in the synthesis of metal oxides, selenides, or sulfides from initially homogeneous solutions [117-119].

In the classical view, a crystal is a solid body with a rigid lattice of molecules, atoms or ions in a characteristic location for the crystal and the unit cell as the smallest repeat unit. Therefore, classical colloidal crystal has a defined geometrical outer shape distinguished by smooth surfaces and layer-by-layer atom/ion/molecule adsorption growth mechanism. On the other hand, the formation of mesocrystals takes place through a second “reaction channel” which involves processes such as parallel crystallization, colloidal assembly and controlled structure formation from nonspherical nanoparticle building units [120] (Figure 4.1). In this way, crystallization gains the freedom to generate complex and esthetically appealing forms with unique chemical and physical properties. Biominerals have shapes that are seldom found in geological or synthetic minerals and which are adjusted to their specific functions resulting in remarkable mechanical, optical, and magnetic properties.

By realizing that we can further learn from natural organization schemes and biological structures, it can be expected that the mesocrystal synthesis as an interesting bottom-up approach mimicking the natural world, will play an important role in the field of functional materials research.

For instance, specific energy storage materials produced, as a highly hierarchical and porous mesocrystals, can be considered as a possible solution for future high rate capability electrodes for lithium-ion batteries. In this case, the internal framework of the mesocrystalline materials can provide high accessibility for the electrolyte and allows efficient charge/discharge cycles of Li^+ ions [27, 121, 122].

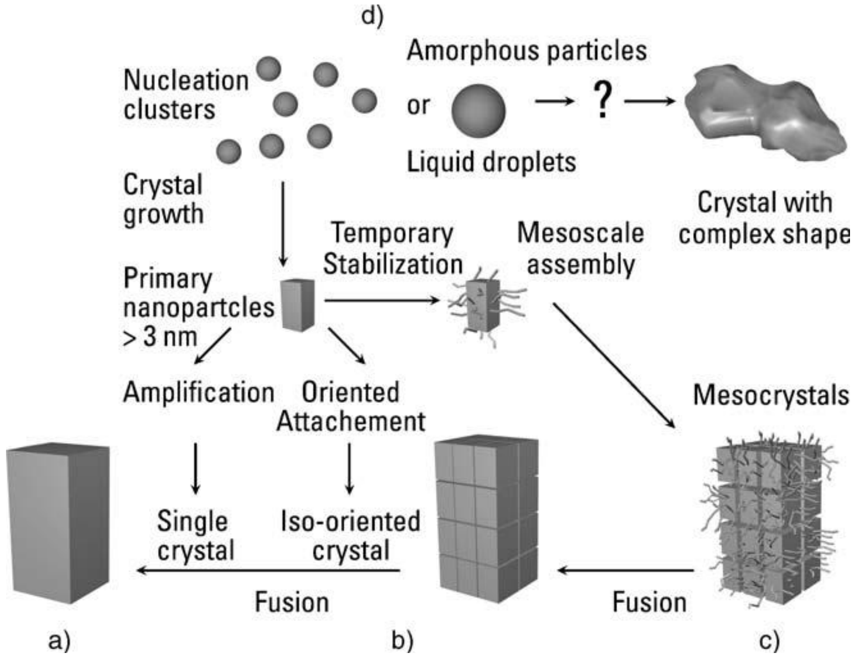

Figure 4.1 Schematic representations of different crystallization pathways: a) classical crystallization leading to the formation of single crystal, b) oriented attachment of primary nanoparticles into iso-oriented crystal, c) mesoscale assembly leading to the formation of mesocrystals, d) formation of complicated morphologies symbolized by the question mark through transformation of amorphous particles [120].

However, it is still challenging to transfer mesocrystals into applicable materials due to the fact that their formation processes are often poorly understood and/or expensive organic additives are needed for their stabilization which is not viable in large scale productions [110].

As already stated in the introduction of this thesis, the morphology of the $LiFePO_4$ is of primary importance for the electrochemical properties, as it eventually determines the rate performance, conductivity and capacity of the of lithium-ion battery cell.

The use of $LiFePO_4$ mesocrystalline hierarchical materials is a rarely adderessed issue and scarce reports published so far describe the use of poly (vinyl pyrrolidone) or other surfactants as growth-directing agents during the synthesis [123-125]. In this chapter, we present a first report of surfactant-free, one-step approach towards mesocrystaline, hierarchically structured urchin-like pristine $LiFePO_4$ and $LiFePO_4$ coated with a thin layer of nitrogen doped carbon as a promising candidate for Li-ion battery cathode material.

4.2 Synthesis

$LiFePO_4$ mesocrystals were synthesized by a one-step low-temperature solvothermal reaction as described below. The precursor solution was prepared by dissolving stoichiometric amounts (3 mmol) of LiOH (98 %, Aldrich), $FeCl_2{\cdot}4H_2O$ (99 %, Sigma-Aldrich) and H_3PO_4 (98 wt % solution in water, Sigma) in ethanol (20 mL) under vigorous mechanical stirring for half an hour. The obtained homogeneous, clear green solution was placed in a glass inlet of a Teflon® lined autoclave (Parr Instrument Company, 45 mL vessel size) which was then sealed and heated up in an oven to 200 °C under autogeneous pressure for 24 h. Precipitation of $LiFePO_4$ mesocrystals took place inside the autoclave during solvothermal process, and the reactor was allowed to cool down to room temperature in a water bath. The supernatant was carefully decanted; the collected green precipitate was washed thoroughly with water until the washings were colorless, and dried under vacuum at 60 °C overnight. In order to achieve *in situ* nitrogen doped carbon coating on the surface of $LiFePO_4$ mesocrystals, N-acetylglucosamine ($C_5H_{15}NO_6$, 98%, Alfa Aesar, 0.15 g) was added in the precursor solution before the autoclave treatment. No surfactants or other growth-directing agents were used during the synthesis.

To increase the crystallinity of synthesized materials and the conductivity of the carbon layer containing samples, some samples were fired in a muffle oven in nitrogen atmosphere with dwell time of 6 h at 700 ^{o}C. The final pristine $LiFePO_4$ mesocrystal powders were very fine and green, while the final $LiFePO_4$ carbon/mesocrystal composites were black in color and needed to be grinded manually for further characterization.

The influence of the Cl^- anions on the formation of the urchin-like mesocrystals of $LiFePO_4$ was investigated using the same synthesis procedure as described above by utilizing different Li and Fe precursors, lithium chloride (LiCl, 98%, Fluka) and iron (II) acetylacetonate ($Fe(acac)_{2,}$ 99%, Chemos).

Additionally, the same method was employed for the synthesis of pristine and carbon coated $LiCoPO_4$ and $LiMnPO_4$ mesocrystals using chlorides as metal (II) precursors ($CoCl_2·6H_2O$, 98%, Fluka and $MnCl_2·4H_2O$, 98%, Aldrich). The precursor solutions and obtained final materials of pristine $LiCoPO_4$ and $LiMnPO_4$ were purple and dark orange, respectfully, while the carbon coated mesocrystals were black in color.

4.3 Results and discussion

For convenience purposes the following notations will be used: $LiFePO_4$ solvothermally synthesized at 200°C =LFP_{200}; $LiFePO_4$ solvothermally synthesized at 200 °C in the presence of carbon precursor =$LFP@C_{200}$; $LiFePO_4$ solvothermally synthesized at 200 °C followed by further annealing =LFP_{700} and $LiFePO_4$ solvothermally synthesized at 200 °C in the presence of the carbon precursor followed by further annealing =$LFP@C_{700}$.

Figure 4.2 shows SEM micrographs of the LFP_{200} at different magnifications and angles of view. The resulting material is highly uniform and consists of monodispersed urchin-like mesocrystal spheres with an average centre diameter of ≈40 µm and different orientations (Figure 4.2b). A closer look at these spherical mesocrystals shows hierarchical morphology – they are formed by the self-assembly of primary $LiFePO_4$ sheets, oriented as in dipole field (e.g., the earth magnetic field) [126]. The length of the primary sheets forming the monodispersed spheres is not uniform and is in the range of several µm in the center of the mesocrystal to several hundred nm on its edges. A small amount of shorter platelet structures around the main mesocrystal are also observed, possibly due to material breakdown (sheet crumbling) during the isolation or characterization.

Higher magnification SEM micrograph (Figure 4.2d) shows the center of the mesocrystal sphere where the primary sheets of $LiFePO_4$ exhibit parallel alignment with an average thickness of ≈150 nm.

This morphology could facilitate Li^+ migration due to the shortened diffusion distance and simultaneously increase exchangeable Li^+ amount. This way, the amount of accessible active surface is higher, possibly offering good electrochemical characteristic of the material.

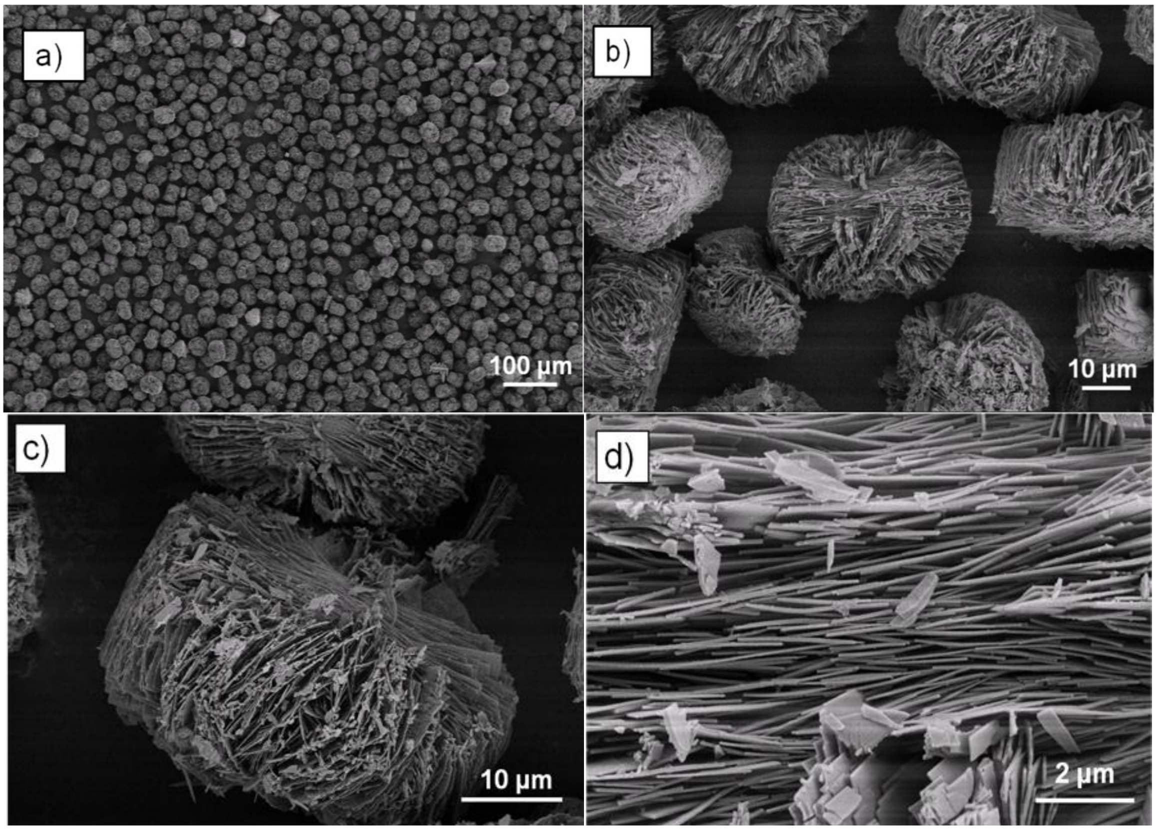

Figure 4.2 SEM images of pristine $LiFePO_4$ mesocrystals synthesized solvothermally at 200 °C (LFP_{200}): a) overview of the material, b) monodispersed urchin-like spheres, c) higher magnification image of one of the spheres oriented normally towards the electron beam, d) parallel alignment of $LiFePO_4$ primary sheets in the center of the mesocrystal sphere.

A very similar morphology has been observed in the case of carbon coated $LFP@C_{200}$ as shown in Figure 4.3. The size of urchin-like self-assembled mesocrystals in this case is smaller; with a main center diameter of ≈25 µm. The primary particles forming the mesocrystalline morphology in the case of $LFP@C_{200}$, are again smaller in the center of urchin-like sphere (oriented rods of ≈1 µm in length and 350 nm in width) in comparison to the ones on the borders.

During the synthesis of *in situ* carbon coated $LiFePO_4$, as two simultaneous processes take place inside the autoclave (formation of the $LiFePO_4$ phase from dissolved metal salts and solvothermal carbonization), smaller primary particles in $LFP@C_{200}$ are to be expected. This is confirmed by SEM and is as a consequence of the encapsulation and stabilization of the inorganic phase by the organic carbon phase.

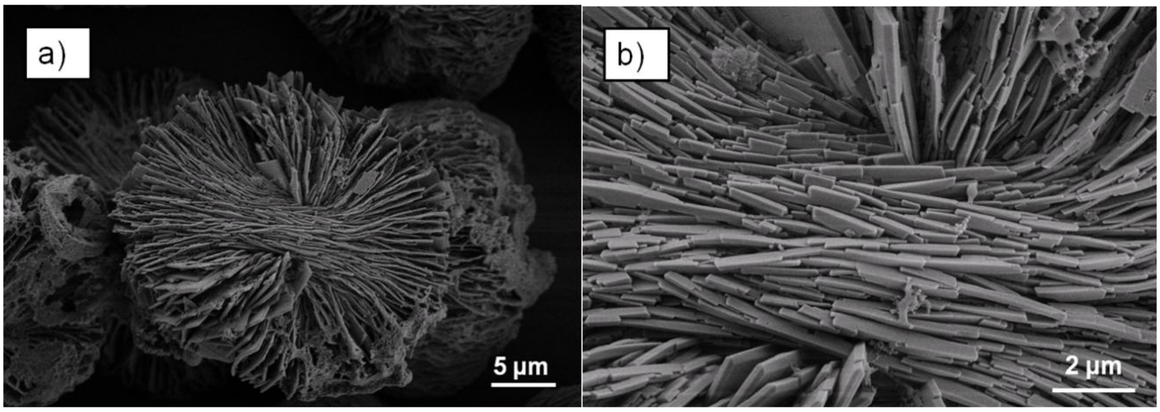

Figure 4.3 SEM images of carbon coated $LiFePO_4$ mesocrystals synthesized solvothermally at 200 °C ($LFP@C_{200}$): a) urchin-like sphere, b) higher magnification micrograph of the center of the urchin-like sphere showing oriented primary rod-like particles.

Remarkably, according to the SEM (Figure 4.4), the morphology of both pristine and carbon coated $LiFePO_4$ does not seem to be altered after further annealing at 700 °C under nitrogen flow, suggesting high stability of the obtained urchin-like, self-assembled mesocrystals.

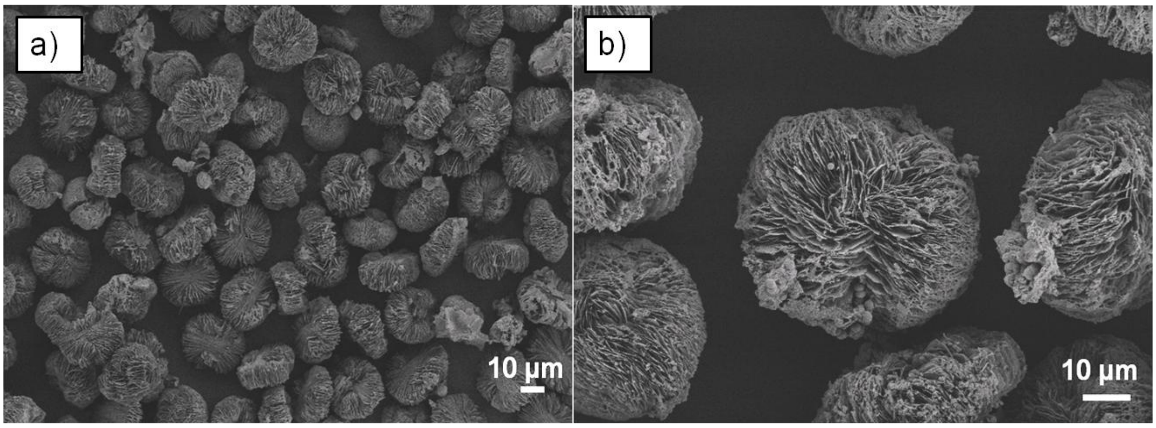

Figure 4.4 SEM images of carbon coated $LiFePO_4$ mesocrystals synthesized solvothermally and further annealed under nitrogen flow at 700 °C ($LFP@C_{700}$): a) overview of the material, b) higher magnification image showing monodispersed urchin-like spheres.

Both morphology and crystallinity of LFP_{200} were further investigated using TEM and HR-TEM (Figure 4.5). Figure 4.5a confirms that the hierarchical urchin-like mesocrystals of $LiFePO_4$ are indeed formed by the assembly of sheet-like structures. This supports the view that the solvothermal treatment at 200 °C is already sufficient to achieve the desired highly crystalline structure of $LiFePO_4$.

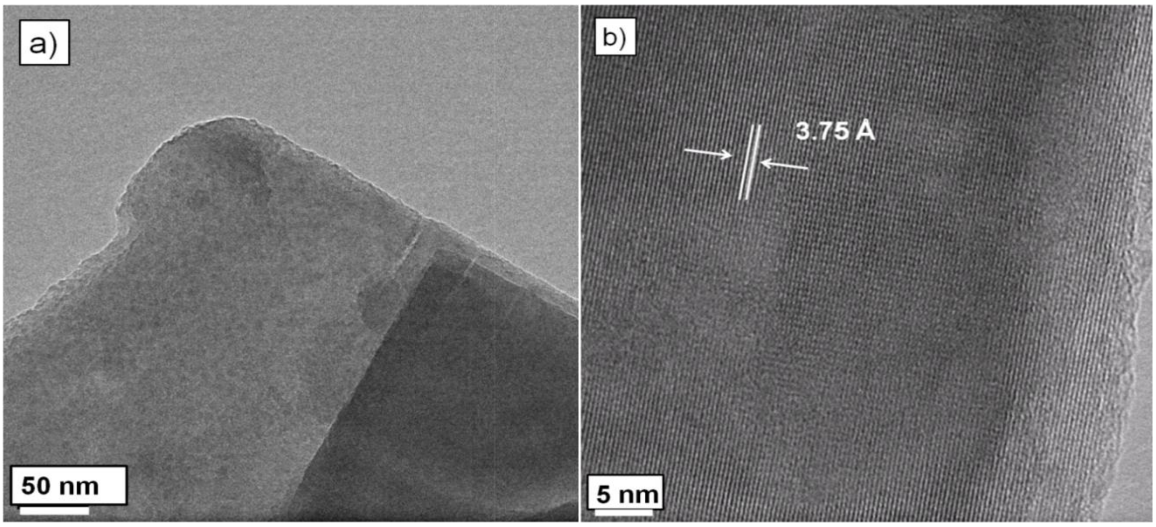

Figure 4.5 TEM (a) and HR-TEM (b) of pristine $LiFePO_4$ mesocrystals synthesized solvothermally at 200 °C (LFP_{200}).

In the case of $LFP@C_{700}$, a more detailed structural HR-TEM study has been performed (Figure 4.6). Figure 4.6a depicts one crumbled primary sheet of $LiFePO_4$ covered by an amorphous carbon coating (light brown) of a few nanometer thickness, as revealed magnified in Figure 4.6b. It can be observed that the existing coating is partially inhomogeneous (10-2 nm thickness) with carbon also present as bulky amorphous agglomerate, instead of a surface layer (Figure 4.6a, marked by number 2). The nitrogen containing carbon, both agglomerated and present as a coating, is formed *via* the solvothermal carbonization of N-acetylglucosamine during autoclave treatment of the precursor solution and its existence has been confirmed by all EA, EDX, XPS and Raman spectroscopy. The width of neighboring lattice fringes in Figures 4.6b and 4.6c (3.5 Å and 3.7 Å) corresponds to (111) and (011) planes of olivine $LiFePO_4$, respectively. The holes seen in Figure 4.6c are present in all the parts of the sample and most probably arise as a result of solvent evaporation during synthesis. The olivine crystallinity matching $LiFePO_4$ is further confirmed by the SAED pattern shown on Figure 4.6d.

The regular rectangular diffraction spot array indicates that the primary sheets forming the final mesocrystal are single crystalline. The (011) and (020) reciprocal lattice vectors of olivine $LiFePO_4$ span the reciprocal lattice and specify that this SAED pattern is taken close to the [100] zone axis, which means that the primary $LiFePO_4$ sheets are observed from the [100] - direction, i.e., the thin side of the sheet is lying along the [100] - direction.

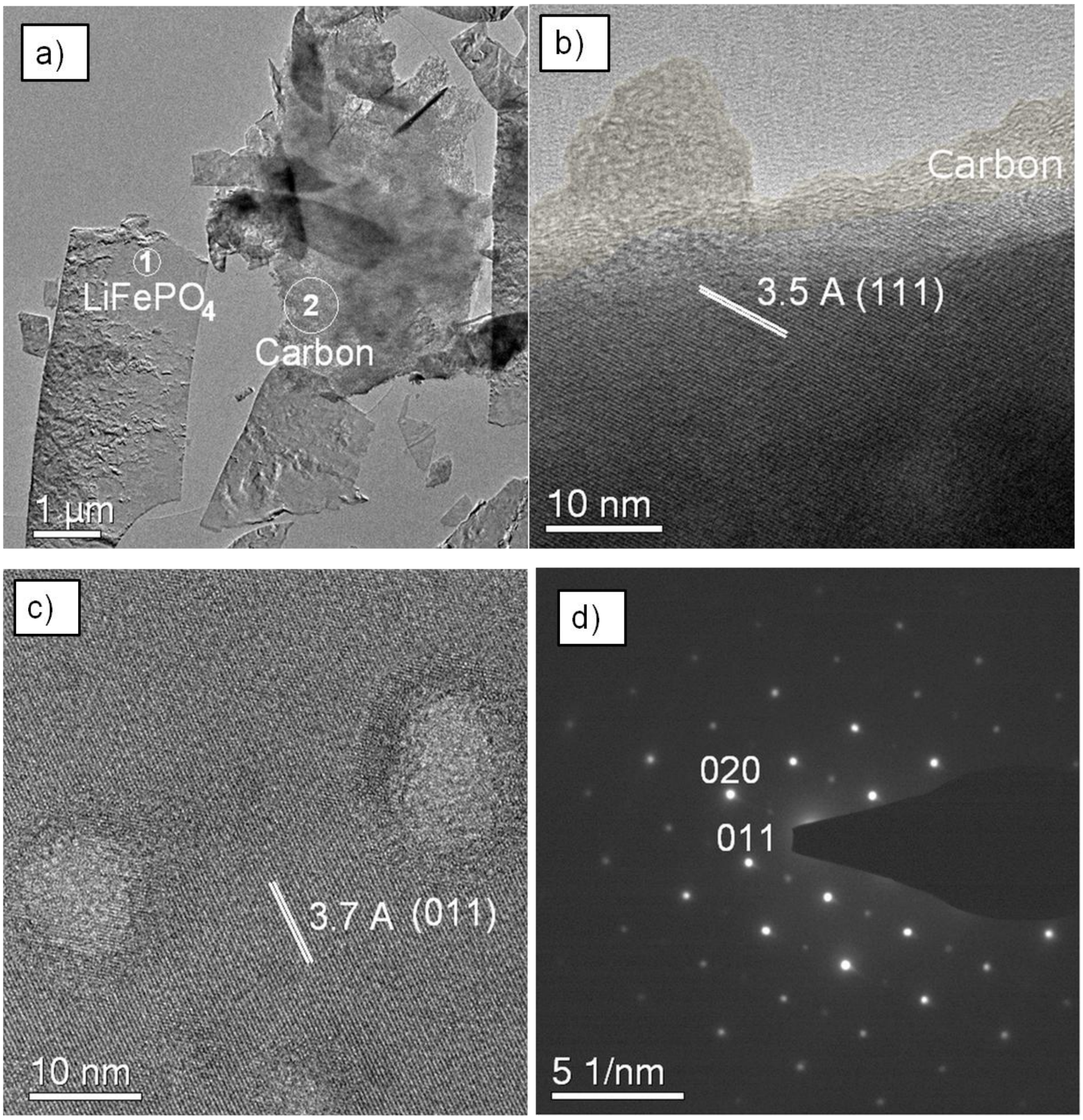

Figure 4.6 HR-TEM of carbon coated $LiFePO_4$ mesocrystal synthesized solvothermally and further annealed under nitrogen flow at 700 °C (LFP@C_{700}): a) overview of the material with visible primary sheet of $LiFePO_4$ and bulky agglomerated carbon, b) non-uniform carbon coating on the surface of the primary sheet of $LiFePO_4$, c) center of the sheet, d) SAED pattern of the primary $LiFePO_4$ sheet shown in a).

However, the SAED pattern in Figure 4.6d exhibits weak spots which do not correspond to the olivine $LiFePO_4$ reciprocal lattice; thus, they are related to another phase. This phase has not been determined so far, but the usual impurity phases in olivine $LiFePO_4$, such as: Li_3PO_4, FeP and $FePO_4$ can be excluded, since they could not be indexed using the observed SAED diffraction spots. Moreover, the reported impurity phase has been observed only on some of the investigated areas of the sample and not in the XRD of the bulk, so its small amount is most likely insignificant.

Using EDX chemical mapping on the selected parts of the LFP@C_{700} sample, previously shown in the Figure 4.6a, the presence of both bulky carbon aggregates (Figure 4.7a) and crystalline $LiFePO_4$ covered with carbon has been confirmed once more (Figure 4.7b).

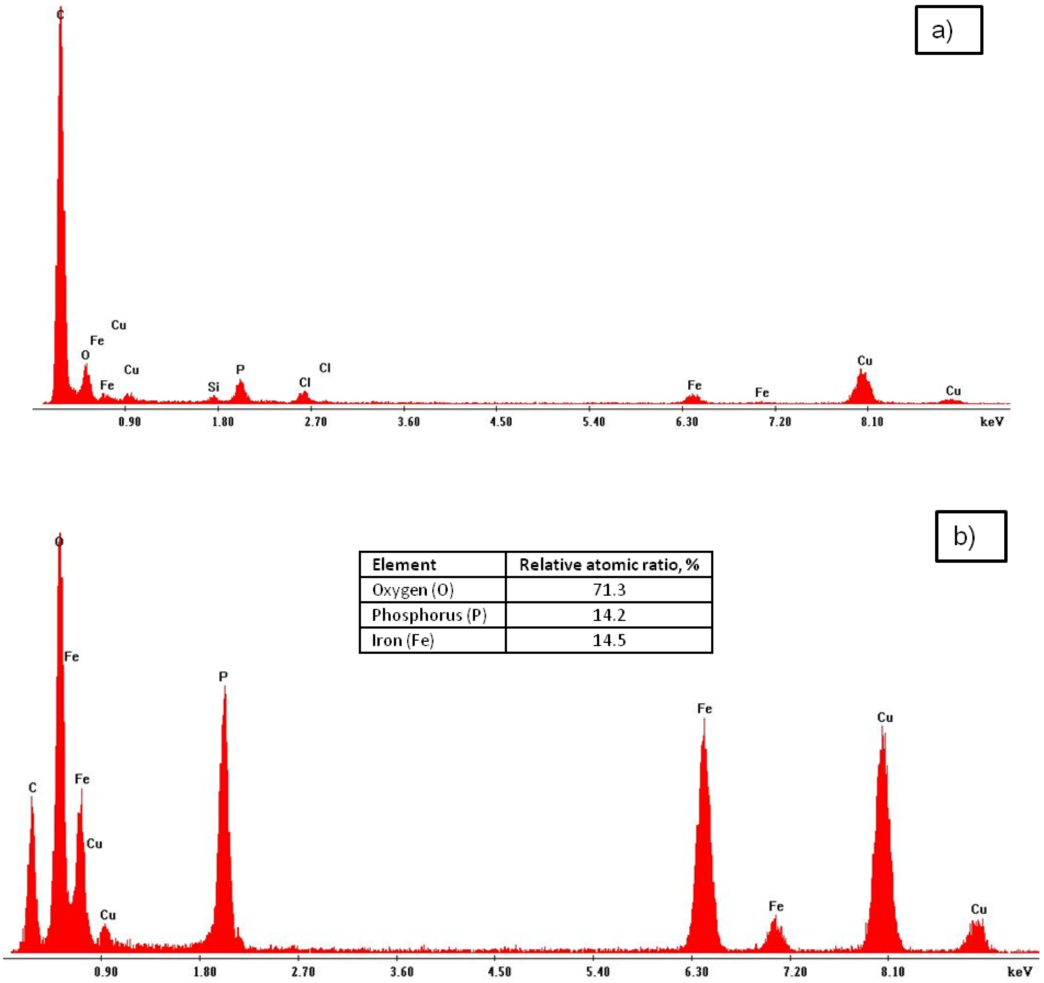

Element	Relative atomic ratio, %
Oxygen (O)	71.3
Phosphorus (P)	14.2
Iron (Fe)	14.5

Figure 4.7 EDX of carbon coated $LiFePO_4$ mesocrystals synthesized solvothermally and further annealed under nitrogen flow at 700 °C (LFP@C_{700}): (a) agglomerated bulky carbon part of the sample previously marked by number 2 in Figure 4.6a, (b) $LiFePO_4$ primary sheet coated with carbon previously marked by number 1 in Figure 4.6a.

Furthermore, a small amount of chlorine (peak close to 2.70 kEV) has also been reported, predominantly within the bulky carbon agglomerates (Figure 4.7a). This is a commonly reported impurity phase in the $LiFePO_4$ synthesized at low temperatures when using chloride-based lithium or iron precursors. Unfortunately, the presence of chlorine can strongly affect the cycling performance of $LiFePO_4$ as will be further discussed further in the subchapter dedicated to electrochemical performance of $LiFePO_4$ mesocrystals.

The XRD patterns of the pristine LFP_{200} (green line) and LFP_{700} (black line) mesocrystals are shown in Figure 4.8. Both patterns clearly show single-phase formation of $LiFePO_4$ without any observable impurity phases.

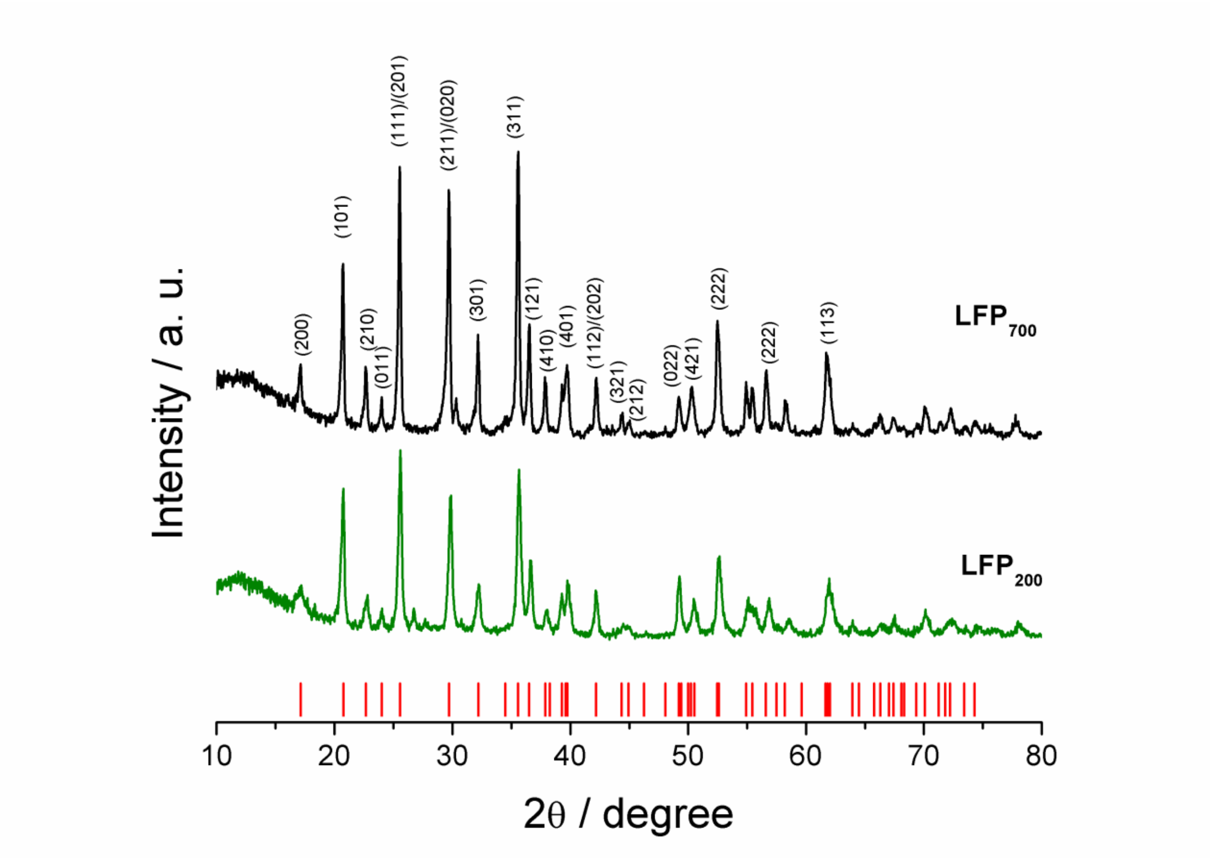

Figure 4.8 XRD patterns of pristine $LiFePO_4$ mesocrystals synthesized solvothermally at 200 °C (LFP_{200}) and further annealed under nitrogen flow at 700 °C ($LFP@C_{700}$)

All of the reported peaks could be indexed to an orthorhombic olivine space group, *Pnma* (ICDD PDF No. 40-1499, represented by red vertical ticks). The profiles of the reflection peaks are narrow and symmetric, indicating high crystallinity of the $LiFePO_4$.

Again, it is very important to note that the full crystallinity of mesocrystals develops already for powders obtained immediately after the solvothermal process at temperature as low as 200 °C.

In comparison to the as-synthesized pristine $LiFePO_4$, the XRD pattern of LFP_{700} exhibits more narrow peaks of higher intensity, presumably due to the sintering effects at higher temperatures. Another important characteristic of the XRD patterns, shown in Figure 4.8, is the intensity ratio of the I(200)/I(020) peaks. Kanamura *et al.* and later Vittal *et al.* have shown that if the intensity of the (020) peak is larger than the (200) peak, which is the case here, platelet or sheet-like structures can be expected [87, 121].

Comparison of the experimental and calculated XRD pattern for the $LFP@C_{700}$ has been performed by full profile matching using Fullprof® software (Figure 4.9) and shows good agreement with the theoretical data, confirming the presence of $LiFePO_4$ as a single crystalline phase in the final powder. No impurity phase could be detected on the macroscopic scale. The experimental intensity data are shown by a gray dotted line, while the solid black line corresponds to the calculated pattern of $LiFePO_4$. The bottom blue line represents the difference between the observed and calculated pattern of $LiFePO_4$.

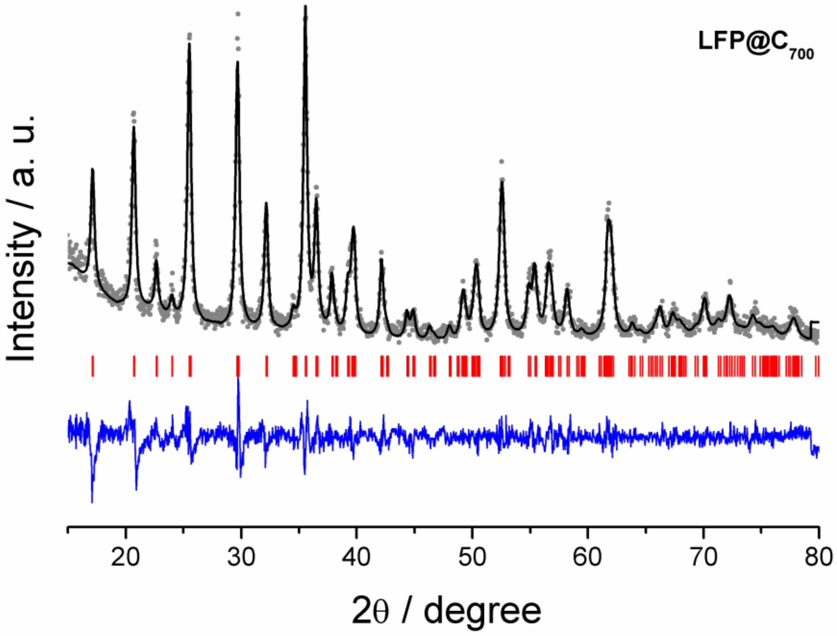

Figure 4.9 XRD profile matching refinement of the carbon coated $LiFePO_4$ mesocrsystals synthesized solvothermally at 200 °C and further annealed under nitrogen flow at 700 °C ($LFP@C_{700}$). Experimental data is represented by gray dots. Blue line corresponds to the difference between observed and calculated pattern of $LFP@C_{700}$.

The red vertical ticks denote the Bragg positions of orthorhombic $LiFePO_4$ (ICDD PDF No. 40-1499). The calculated lattice parameters are: a = 10.34180 Å, b = 6.01060 Å, c = 4.70820 Å, with a final unit volume of 292.66 $Å^3$, which is similar to the previous reports for $LiFePO_4$ synthesized using high-temperature solid-state method [36]. Additionally, there is no evidence of the presence of carbon related peaks in the XRD pattern, due to its amorphous nature, as visualized in HR-TEM, and its small quantity with the respect to the dominant $LiFePO_4$ phase.

The oxidation state of iron (Fe^{2+} and/or Fe^{3+}) in $LiFePO_4$ as well as the type of carbon (sp^2 and/or sp^3) deposited on its surface plays an important role for the electrochemical behavior of this type of $LiFePO_4$/carbon composite. Therefore, high resolution XPS analysis, EELS spectroscopy, Raman spectroscopy and elemental analysis have been conducted to examine the surface and the bulk of the LFP@C_{700} composite.

XPS is a non-destructive technique frequently used as an evaluation analysis of valence states of metal/non-metal ions in cathodes for Li-ion batteries [70, 127]. C 1s and Fe 2p high resolution XPS spectra together with their corresponding energies (BE) are shown in the Figure 4.10.

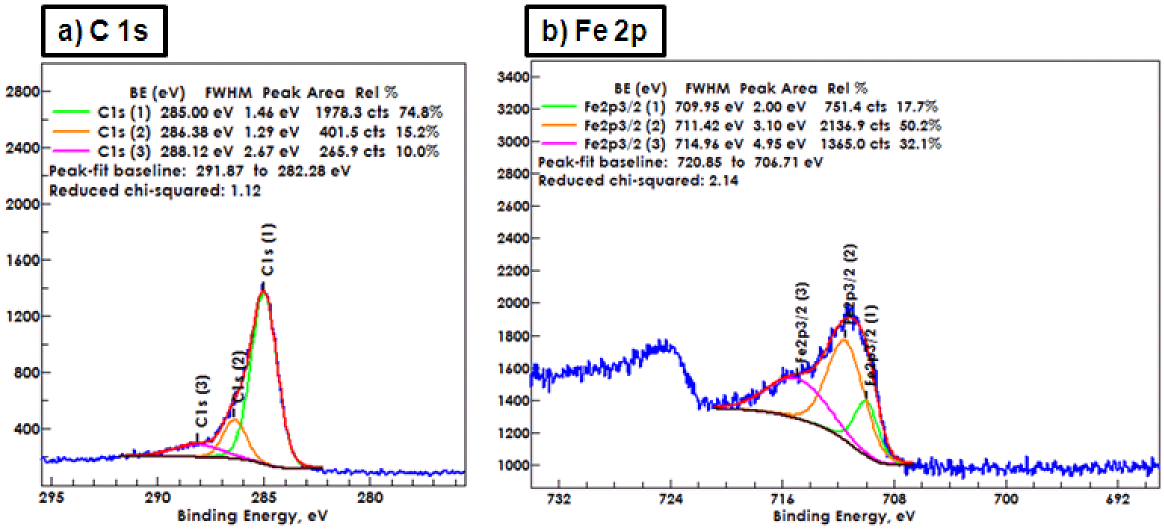

Figure 4.10 HR-XPS spectra of the carbon coated $LiFePO_4$ mesocrystals synthesized solvothermally at 200 °C (LFP_{200}) and further annealed under nitrogen flow at 700 °C (LFP@C_{700}): a) C 1(s) and (b) Fe 2(p) envelopes.

From the C 1s spectra (Figure 4.10a), it is clear that the carbon phase in the composite material is predominately sp^2 hybridized carbon (BE = 285.00 eV, C 1s (1)) with oxygenated surface groups such as C-O (BE = 286.38 eV, C 1s (2)) and C=O (BE = 288.45 eV, C 1s (3)) present in less significant quantity, as expected for carbons synthesized under hydrothermal/solvothermal conditions [128]. On the other hand, the spectrum of Fe $2p_{3/2}$ (Figure 4.10b), can be deconvoluted into a component at BE = 709.95 eV (Fe $2p_{3/2}$ (1)) corresponding to Fe^{2+} and a component at BE = 711.42 eV (Fe $2p_{3/2}$ (2)), indicating the presence of Fe^{3+} ions on the surface of LFP@C_{700} composite. The energy separation between these two peaks is in good agreement with the literature, while the peak intensities indicate that there is more Fe^{3+} then Fe^{2+} species present at the surface of the synthesized material [129].

An additional study of the oxidation state of iron in the LFP@C_{700} composite has been performed using EELS. Figure 4.11 shows the iron L-edge, calibrated by reference measurements on Fe_2O_3. Both, the L_3 and the L_2 edges show a characteristic shape for the Fe^{2+} valence state of iron, which has a strong first peak followed by a shoulder of lower intensity. Even though it is close to the energetic position of the Fe^{3+} valence state, such a shoulder has been also observed for solitary Fe^{2+} containing phases in several materials and is attributed to the site dependence effect [57].

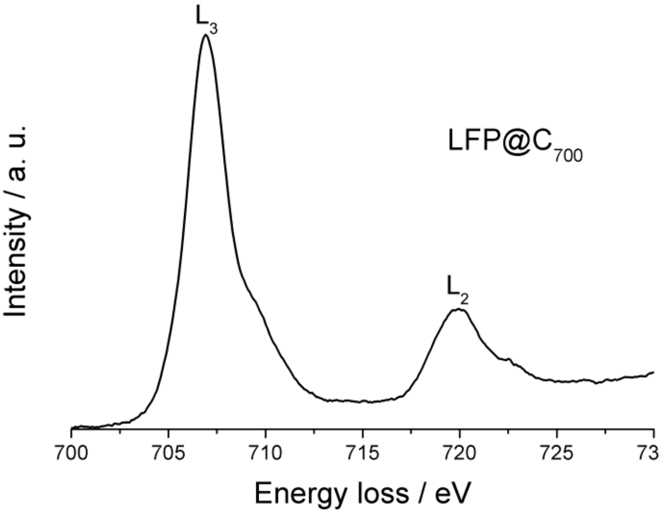

Figure 4.11 EELS spectra of the carbon coated $LiFePO_4$ mesocrystals synthesized solvothermally at 200 °C and further annealed under nitrogen flow at 700 °C (LFP@C_{700}).

Consequently, from the EELS observations, it can be concluded that Fe^{2+} is the predominant iron valence state in the synthesized $LiFePO_4$, while Fe^{3+} is absent or present in very small or undetectable amounts. This finding opposes the result established from the photoelectron spectra, but can be explained by the different surface sensitivities of the two techniques. While the penetration depth of HR-XPS is only a few nanometers, the EELS signal originates from the whole primary sheet of $LiFePO_4$ with the thickness of about 150 nm. Accordingly, the final conclusion is that the synthesized $LFP@C_{700}$ composite contains predominantly Fe^{2+} in the bulk whilst terminates with Fe^{3+} on its surface.

The elemental analysis of $LFP@C_{700}$ showed 12 wt % C and 2 wt % N (more than one measurement in the bulk).

Raman spectroscopy is an excellent analytical tool to re-confirm the presence of carbon in the $LiFePO_4$ composite. Nevertheless, high energy excitation of the laser used in Raman spectroscopy could damage the inorganic-organic composite material. Figure 4.12 shows Raman spectra of LFP_{700} as well as $LFP@C_{700}$.

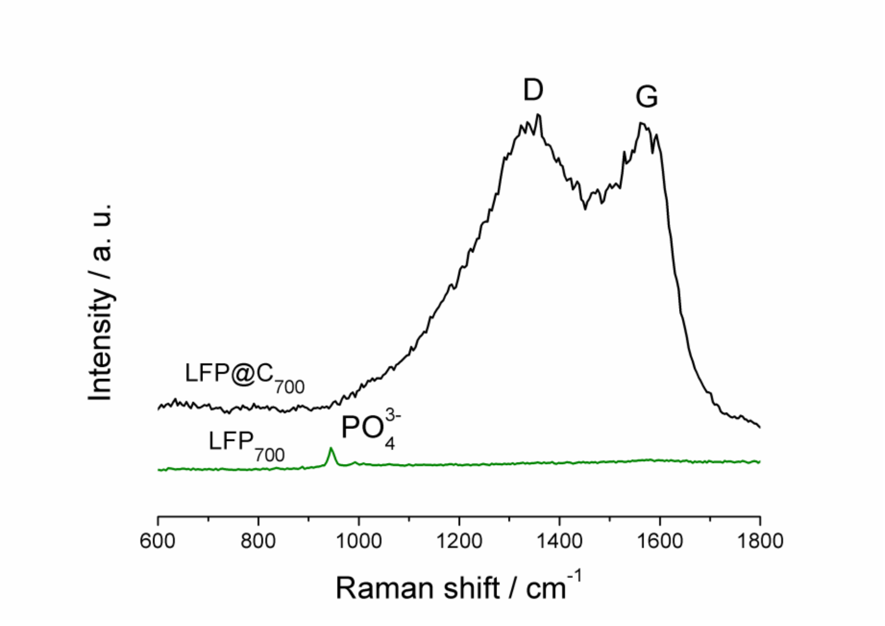

Figure 4.12 Raman spectra of the pristine LFP_{700} and carbon coated $LFP@C_{700}$ mesocrystals.

In the case of $LFP@C_{700}$, only two broad bands can be observed, corresponding to the A_{1g} mode of the disordered carbon (D-band, sp^2) and the E_{2g} mode of the ordered graphitic carbon (G-band, sp^3) [130]. The I_D/I_G intensity ratio represents the degree of surface disordering of carbon coating/aggregated carbon.

As visible from Figure 4.12, $I_D/I_G \approx 1$ for LFP@C_{700}, indicating equal presence of disordered and graphitic carbon in the coating of $LiFePO_4$ sheets. This is in opposition to the XPS findings, suggesting that during Raman measurements under high intensity laser beam, amorphous carbon in synthesized mesocrystalls undergoes further graphitization and higher I_G is recorded.

Additionally, in Raman spectra of LFP@C_{700}, no peaks can be detected in the region 600-1100 cm^{-1} as it would be expected for the intra-molecular stretching modes of the PO_4 groups in $LiFePO_4$. This is possibly due to the rather full coverage of the inorganic phase by the organic phase. In the case of LFP_{700}, a small band is visible at 945 cm^{-1} corresponding to PO_4 groups [71].

In order to test the possible mesoporosity of the synthesized mesocrystals suggested by their morphology, nitrogen adsorption/desorption experiments have been performed (Figure 4.13).

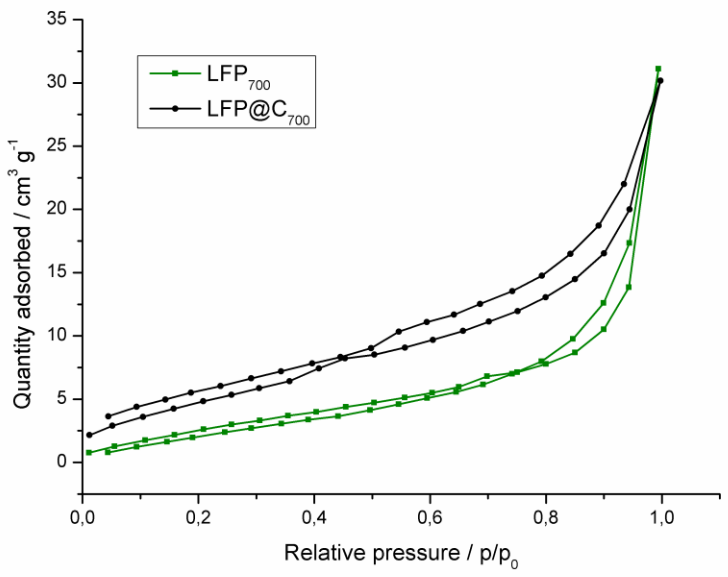

Figure 4.13 BET nitrogen sorption isotherms of the pristine LFP_{700} and carbon coated LFP@C_{700} mesocrystals.

Unfortunately, both LFP_{700} and LFP@C_{700} show undeveloped porosity with a type IV physisorption isotherms according to the IUPAC classification. The type IV isotherms posses a common hysteresis loop: the lower part representing the progressive adsorption of gas at increasing relative pressure, while the upper part denoting the progressive withdrawal or desorption of the adsorbate.

In this case, limited hysteresis of both materials suggests low microporosity. Calculated BET surface areas for LFP_{700} and $LFP@C_{700}$ are as low as $S_{BET} = 11\ m^2\ g^{-1}$ and $S_{BET} = 18\ m^2\ g^{-1}$, respectively.

4.4 Proposed formation mechanism

All of the materials described so far were synthesized using $FeCl_2·4H_20$ as iron precursor due to its solubility in ethanol, low cost and the ability to produce a pure phase $LiFePO_4$ material. Following the same procedure as described in the experimental part except for changing the iron (II) precursor from chloride to acetylacetonate, the formation of mesocrystals was no longer occurring. Instead, nanostructured $LiFePO_4$ and carbon coated $LiFePO_4$ nanoparticles were obtained (as it will be described in the Chapter 5).

It has already been documented that the counter anion of metal salt precursor has a significant effect on the final morphology of the inorganic material prepared *via* solution chemistry, especially in the case of Cl^- anion [109, 131, 132]. Thus, in order to ascertain the possible influence of Cl^- anion, another test reaction was performed by changing the Li precursor from LiOH to LiCl and Fe (II) precursor from $FeCl_2·4H_20$ to iron (II) acetylacetonate, without the presence of the carbon precursor in the reaction solution.

Indeed, the results of this reaction show that urchin-like mesocrystals of $LiFePO_4$ are now again easily obtainable, giving evidence that Cl^- anions truly act as the morphology directing agent (Figure 4.14).

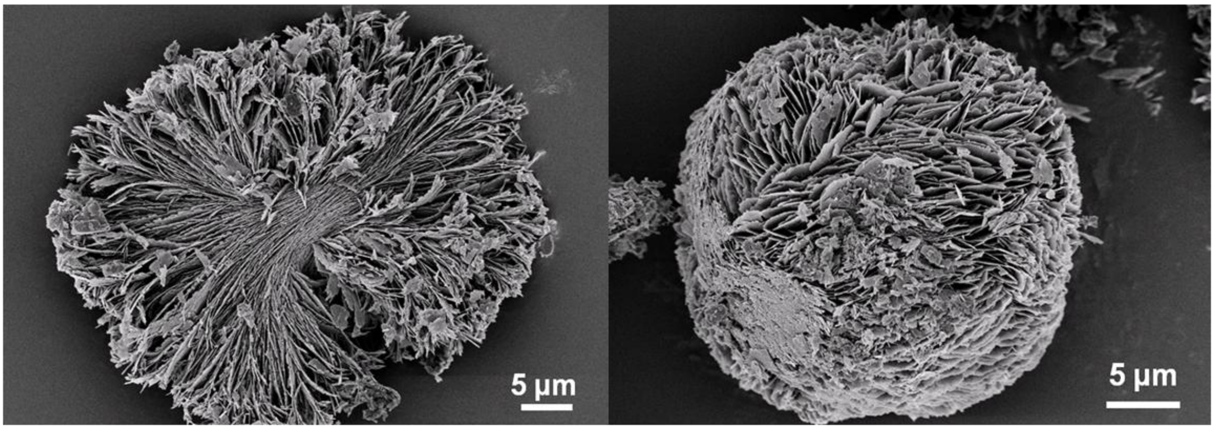

Figure 4.14 SEM images of two different mesocrystals of $LiFePO_4$ obtained from iron (II) acetylacetonate as iron source and lithium chloride as lithium source *via* the solvothermal synthesis at 200 °C.

The XRD pattern of the $LiFePO_4$ mesocrystals obtained from iron (II) acetylacetonate as iron source and lithium hydroxide as lithium source *via* the solvothermal synthesis at 200 ^{o}C is shown in Figure 4.15. Syntesized mesocrystals could be indexed as pure orthorhombic olivine $LiFePO_4$, space group *Pnma* (ICDD PDF No. 40-1499, red ticks in Figure 4.15).

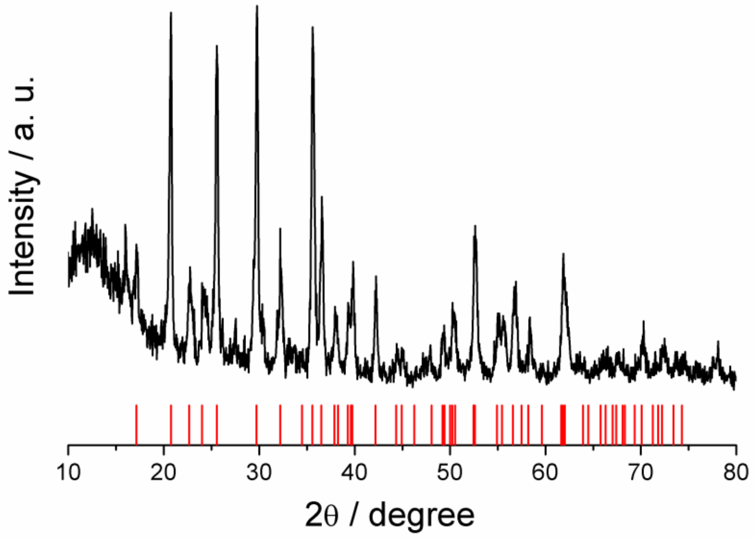

Figure 4.15 XRD pattern of $LiFePO_4$ obtained from iron (II) acetylacetonate as iron source and lithium hydroxide as lithium source *via* the solvothermal synthesis at 200 °C.

Again, high crystallinity (narrow and sharp peaks) of the obtained material develops immediately after the solvothermal process at temperature as low as 200 °C. Finally, it can be concluded that indeed Cl^- anion plays a key role in the formation of sheet-like structures and self-assembly, while the carbon precursor does not have major influence on the morphology of the final material. However, detailed and controlled time-dependent crystal growth experiments need to be performed in order to assess the possible formation mechanism of $LiFePO_4$ sheet growth and self-assembly. It can be assumed that in this case the Cl^- anion acts as a linker ligand forming coordination complexes with dissolved Fe^{2+} and/or Li^+ and oxygen in the precursor solution.

At the beginning of the solvothermal reaction, the complexed precursor decomposes and the nuclei of $LiFePO_4$ are formed under elevated temperature and auto-geneous pressure in the autoclave vessel. These nuclei grow in the form of primary sheets through the processes of mass diffusion and Ostwald ripening based on their inner crystallographic orientation.

As suggested by the SEM of the amorphous precipitate obtained after 6 h (Figure 4.16), poorly crystalline (confirmed by XRD, data not shown) anisotropic dumbbell-like particles with smooth surfaces are an intermediate "seed" stage towards highly crystalline final urchin-like spheres.

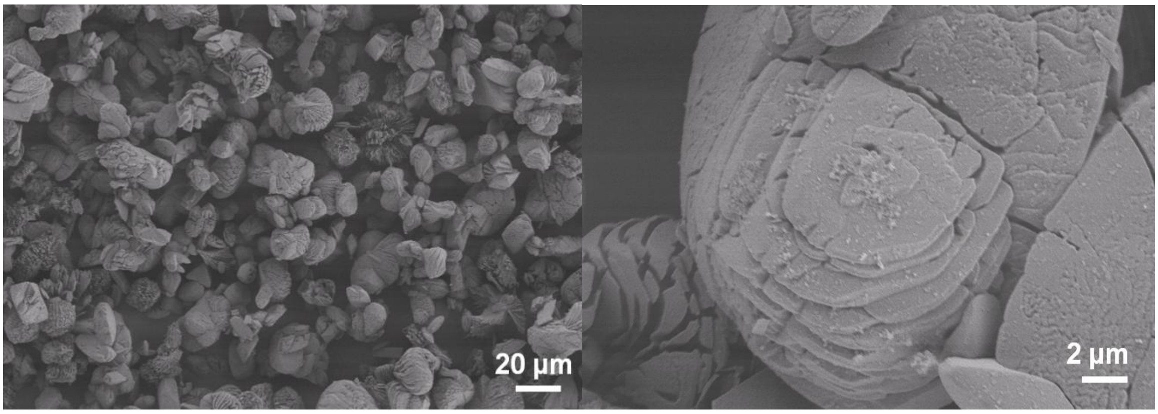

Figure 4.16 SEM image of the amorphous product obtained *via* solvothermal reaction using equimolar amounts LiOH, $FeCl_2·4H_20$ and H_3PO_4 after 6 hours.

In the case of the mesocrystals synthesized in the presence of N-acetylglucosamine, it is believed that the decomposition of carbon precursor in solvothermal carbonization is a process simultaneous to the formation of the inorganic phase. As previously reported by Titirici *et. al.* [133], solvothermal/hydrothermal carbonization of nitrogen-containing carbohydrates (in this case N-acetylglucosamine) at temperatures higher than 180 ^{o}C proceeds through complex Maillard-type reactions between hydroxymethylfurfural (HMF, containing an aldehyde group) as an initial sugar dehydration step product and the amine which lead towards nitrogen-containing heterocycle intermediates. These nitrogen-containing heterocycle intermediates finally produce the amorphous carbonaceous material with incorporated nitrogen by polymerization/aromatization reactions.

In conclusion, the dependence of the morphology and structure on the experimental conditions (concentration of the reactants, temperature, reaction time, different anions of the given metal salt solution, etc.) needs to be investigated and optimized in order to design a controlled and easily up-scalable reaction for production of urchin-like $LiFePO_4$ mesocrystals.

4.5 Li^+ insertion/extraction measurements

The electrochemical properties of the pristine LFP_{700} and $LFP@C_{700}$ as cathodes for Li-ion batteries were investigated and compared to each other. In the conducted experiments, two-electrode Swagelok® cells and pure lithium foil as a counter/reference electrode were used.

Figure 4.17a shows the charge (Li extraction)/discharge (Li insertion) profiles of the pristine LFP_{700} mesocrystals for the 1st and 6th cycle in the cut-off voltage range between 2.0-4.3 V at 0.1 *C* current density (which corresponds to the current required to completely charge/discharge an electrode in 10 h, 1 *C* = 170 mA h g^{-1}). The observed polarization between the charge and discharge profiles is high ($\Delta V \approx 1$ V for the first cycle) (Figure 4.17a) indicating slow kinetics for this material. Additionally, the poor intrinsic electron conductivity of pristine LFP_{700} resulted in low charge and discharge capacities, ≈25 mA h g^{-1} (Figure 4.17b) which is far beyond any practical applicability. Compared to LFP_{700}, the charge and discharge capacities of the $LFP@C_{700}$ are much higher (Figure 4.17d) due to the fact that the slow kinetics of $LiFePO_4$ is enhanced by the electronic conductivity facilitated by the carbon coating.

A nice flat plateau at 3.4-3.5 V (Figure 4.17c) is observed during the charge/discharge process, indicating the typical two-phase nature of the lithium extraction and insertion reactions between $LiFePO_4$ and $FePO_4$, as described in literature. It must be pointed out that the capacity during the first lithium extraction is higher than the capacity recovered during the following discharge cycle, 121 and 87 mA h g^{-1} at 0.1 *C*, respectively. This corresponds to a capacity loss of 34 mA h g^{-1} (Figure 4.17c). Additionally, considerable polarization ($\Delta V = 46$ mV) between the two plateaus was observed.

Capacity loss at the first cycle is a common phenomenon for $LiFePO_4$ materials which can be linked to the fact that i) there is a possibility of existence of un-reacted $FePO_4$ in the center of large particles resulting in the irreversible capacity loss after the first charge which is well explained according to the model proposed by Anderson and Thomas [134], ii) carbon coated samples are subject to undergo an “activation” process during the first cycle [134, 135]. Additionally, the nature of non-uniform carbon coating and its contact with the boundary of the $LiFePO_4$ sheets could hinder Li^+ penetration.

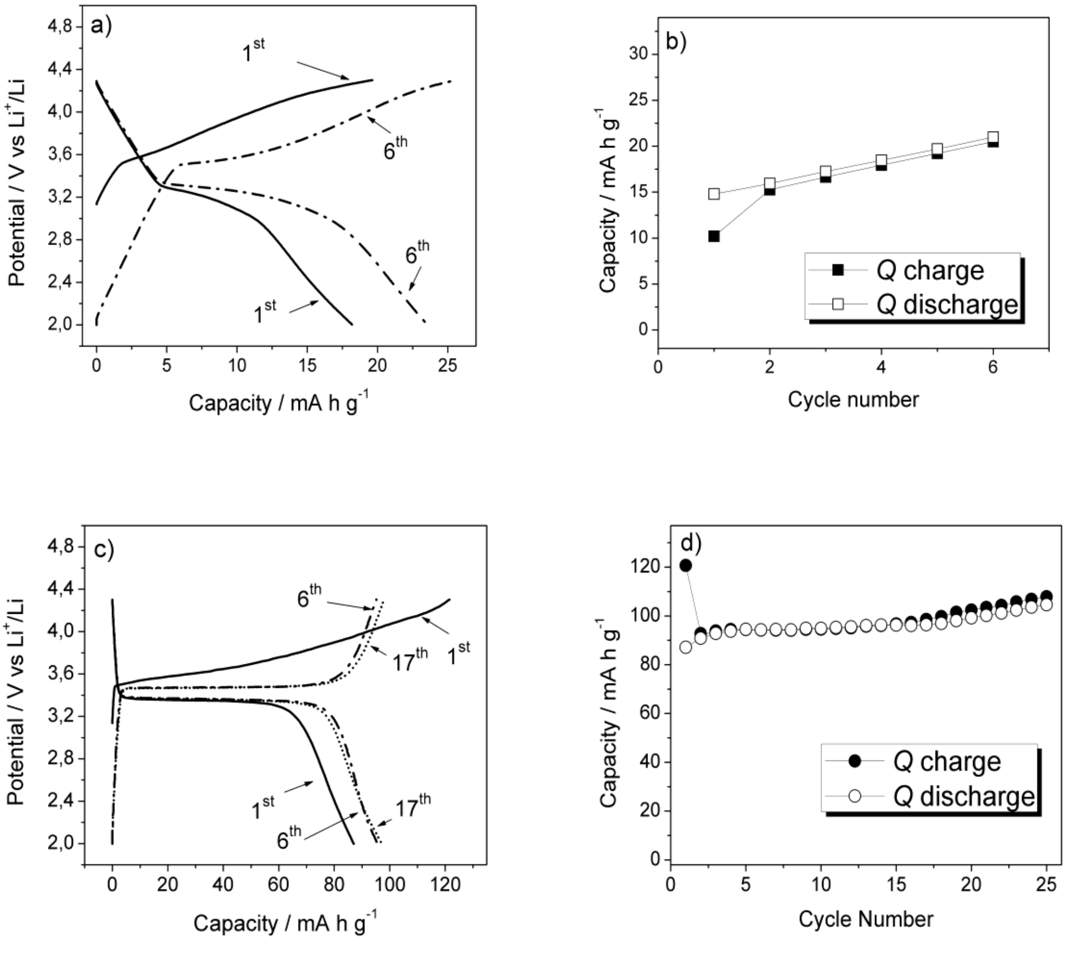

Figure 4.17 Electrochemical properties of pristine LFP_{700} and $LFP@C_{700}$: (a), (c) galvanostatic charge/discharge cycle curves for the Li insertion of the pristine LFP_{700} and $LFP@C_{700}$ at *C*/10 current density (b), (d) charge/discharge capacity vs. cycle number plot for pristine LFP_{700} and $LFP@C_{700}$.

After the first cycle, the gap between the charge - discharge plateau is reduced to ΔV ≈ 0.1 V (Figure 4.17c) by the lowered charging plateau (not by the elevated discharging plateau), which presumably shows that the activation is more favored on the charging phase. During subsequent cycles, a slight increase in capacity without any fading was found leading to ≈100 mA h g^{-1} values at 0.1 *C* current density. Figure 4.17d demonstrates good cycling stability of the hierarchically structured LFP@C_{700}.

Another point that needs to be highlighted is the unusual feature of the first charge profile of the LFP@C_{700}. This could be due to the presence of the chlorine impurity visualized by EDX. Chloride impurities can undergo oxidation at elevated voltage (≈3.9 V) resulting in the partial corrosion of the current collector. A further reason might lie in the nature of the nitrogen containing carbon coating of $LiFePO_4$. As previously stated, the performance of $LiFePO_4$ is highly dependent on the character of the deposited carbon on its surface. Additionally, a slight gain in capacity was observed when the electrode was discharged below 3 V which is presumably due to the presence of Fe^{3+} impurities. This finding is in good agreement with the XPS measurement (Figure 4.10).

The rate capability of the both LFP_{700} as well as LFP@C_{700} was characterized by applying different current densities during every six cycles (Figure 4.18).

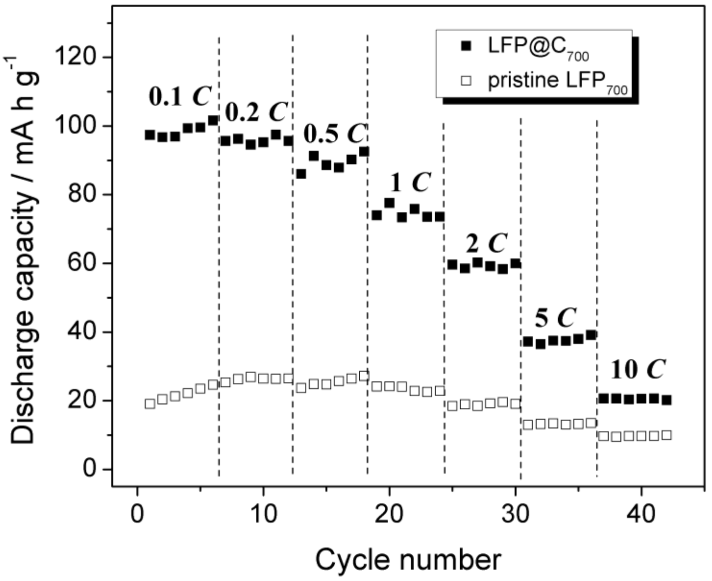

Figure 4.18 Cycling and rate performance of pristine LFP_{700} and LFP@C_{700} mesocrystals.

The capacity delivered from the composite is quite sensitive to the charging procedure. A gradual decrease of discharge capacity with increase in *C*-rate is evident, as it is generally the case for all electrodes. This is attributed to the slow diffusion of Li-ions to meet the fast reaction kinetics at higher *C*-rates. The rate performance test however indicates that carbon coated $LiFePO_4$ shows a much better rate capability in comparison to the pristine LFP_{700}. However, this micro-ranged carbon coated hierarchical material as well as $LiFePO_4$ material with a similar topography described in a recent publication [125] cannot reach the desired theoretical capacity (170 mA h g^{-1}) as compared to other nanostructured $LiFePO_4$ materials. This might be related to all the imperfections in its structure mentioned above, in particularly the inhomogeneous coating due to the large size of the mesocrystals. Each microcrystal is a hierarchical assembly of smaller nanoplates. Thus, individual coating of each nanoplate is a difficult case. Nevertheless, it is believed that such unique hierarchical nanosystems on several length scales will become promising materials for energy storage in the future.

4.6 Extension to other $LiMPO_4$ olivines

The above described synthetic procedures could also be employed to produce other lithium phosphor-olivine mesocrystals, using suitable chloride precursors and solvothermal synthesis at 200 °C. Such morphologies formed upon the influence of Cl^- anion as a growth directing agent have not been reported so far in literature for $LiCoPO_4$ and $LiMnPO_4$.

Figure 4.19a depicts one monodispersed mesocrystal of $LiCoPO_4$ with a center diameter of ≈50 µm. The mesocrystal is formed out of ≈25 µm long primary crystallites radiating from the same center (Figure 4.19a). It can be observed that the width of the crystallites gradually decreases from ≈1 µm in the center towards the end, forming needle-like morphology (Figure 4.19b and c). The surface of needle-like primary particles is not smooth, but it contains nano-sized holes which can be visible in the higher magnification micrographs (Figure 4.19d). No dipole field affecting the orientation of the primary particles has been detected as observed for $LiFePO_4$ mesocrystals previously described.

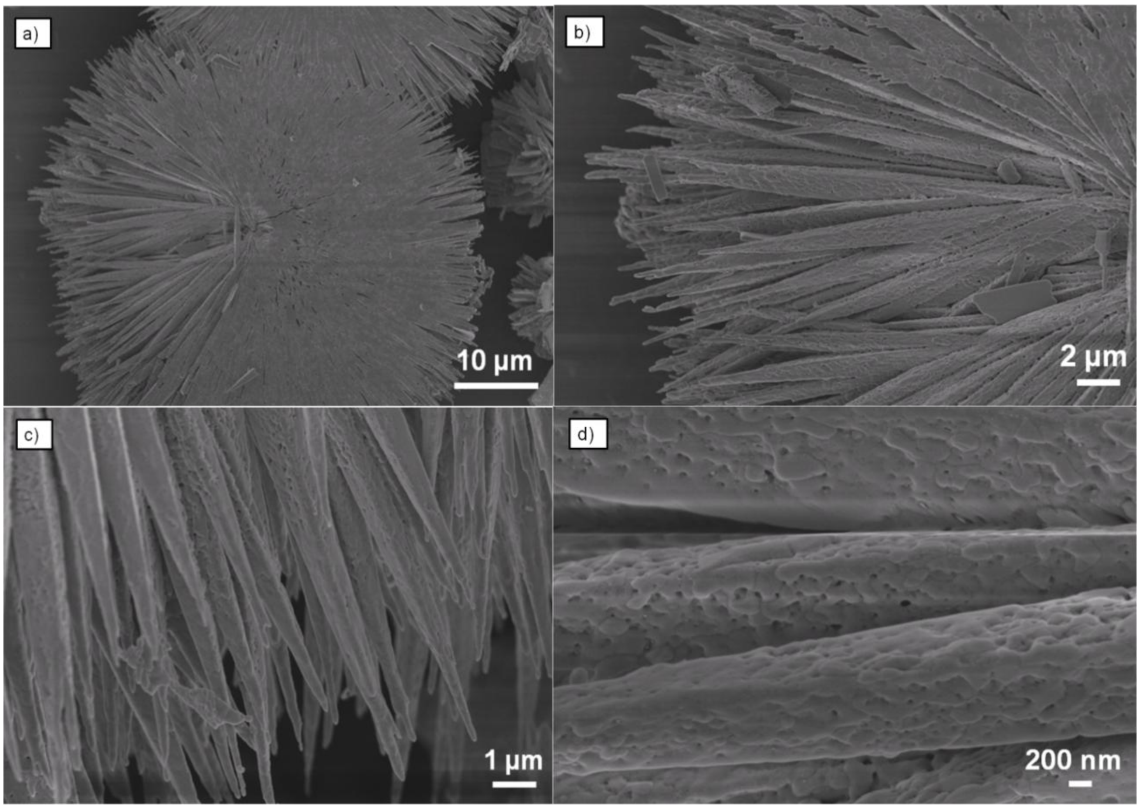

Figure 4.19 SEM images of pristine $LiCoPO_4$ mesocrystals synthesized solvothermally at 200 °C: a) monodispersed sphere of urchin-like mesocrystal, b), c) tips of the needle-like primary particles, d) higher magnification image showing the surface of the needle like particles shown in b).

On the other hand, $LiMnPO_4$ mesocrystals unfortunately do not exhibit uniform morphology throughout the entire sample. Figure 4.20a shows one type of mesocrystal morphology formed out of very thin sheet-like structures as primary particles.

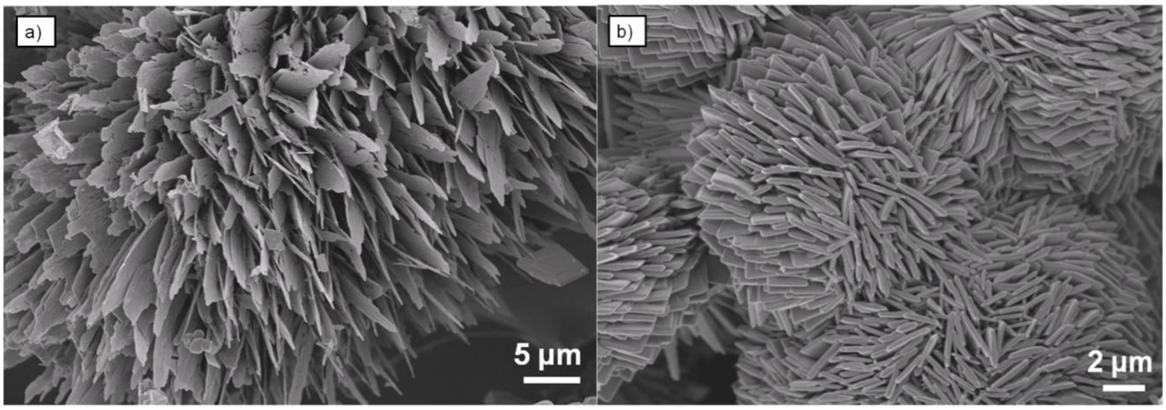

Figure 4.20 SEM images of two types of morphology of pristine $LiMnPO_4$ mesocrystals synthesized solvothermally at 200 °C.

These grass-like crystalline plates are curved towards their ends and self-assemble in agglomerates several tens of µm starting from the center. Figure 4.20b shows the second type of morphology found in $LiMnPO_4$ sample where mesocrystals are found as aggregated spheres with a central diameter of ≈20 µm. The spheres consist of differently oriented ≈500 nm thick uniform rectangular primary particles.

XRD patterns of the pristine $LiCoPO_4$ and $LiMnPO_4$ corresponding to the previous shown SEM images are represented in Figure 4.21.

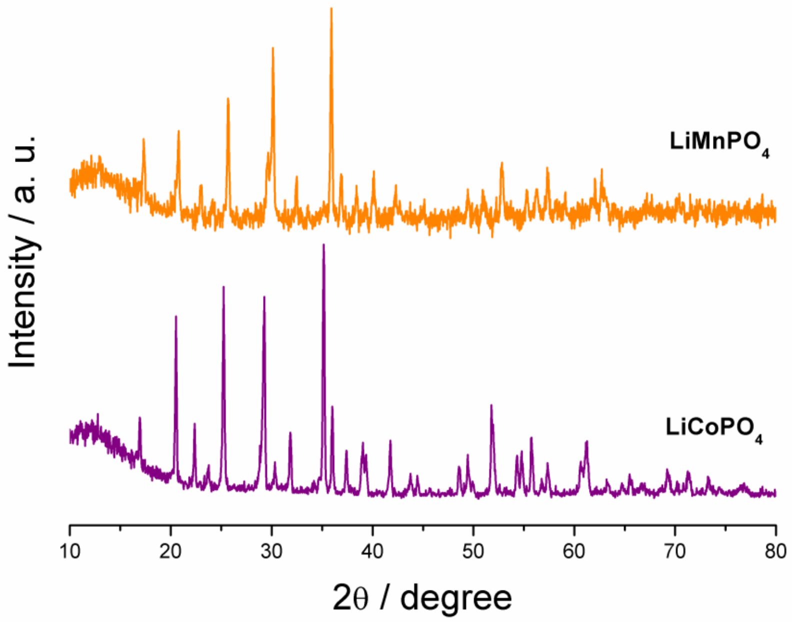

Figure 4.21 XRD patterns of pristine $LiCoPO_4$ and $LiMnPO_4$ mesocrystals synthesized solvothermally at 200 °C.

The sharp diffraction peaks without any impurity phases point out the formation of highly crystalline $LiMPO_4$ materials at a low temperature of 200 ^oC, very similar to their $LiFePO_4$ counterparts. All of the reflections could be indexed on the basis of the orthorhombic olivine-type structure with the *Pnma* space group. The reflections gradually shift to higher angles from Co to Mn due to decrease in ionic radii values. The colors used for marking XRD patterns in Figure 4.21 match the final colors of the obtained materials.

Additionally, it has been proven that $LiCoPO_4$ and $LiMnPO_4$ can also be successfully *in situ* coated using N-acetylglucosamine as the nitrogen-containing carbon precursor. Thick and uniform amorphous carbon coating (≈25 nm) was observed in the case of $LiCoPO_4$ as depicted in Figure 4.22. Figure 4.22a shows two aggregated needle-like primary particles forming the final mesocrystal, while Figure 4.22b shows the tip of one of the spike-like particle with black $LiCoPO_4$ in the center and gray carbon coating on the surface. Data concerning carbon coated $LiMnPO_4$ are not presented.

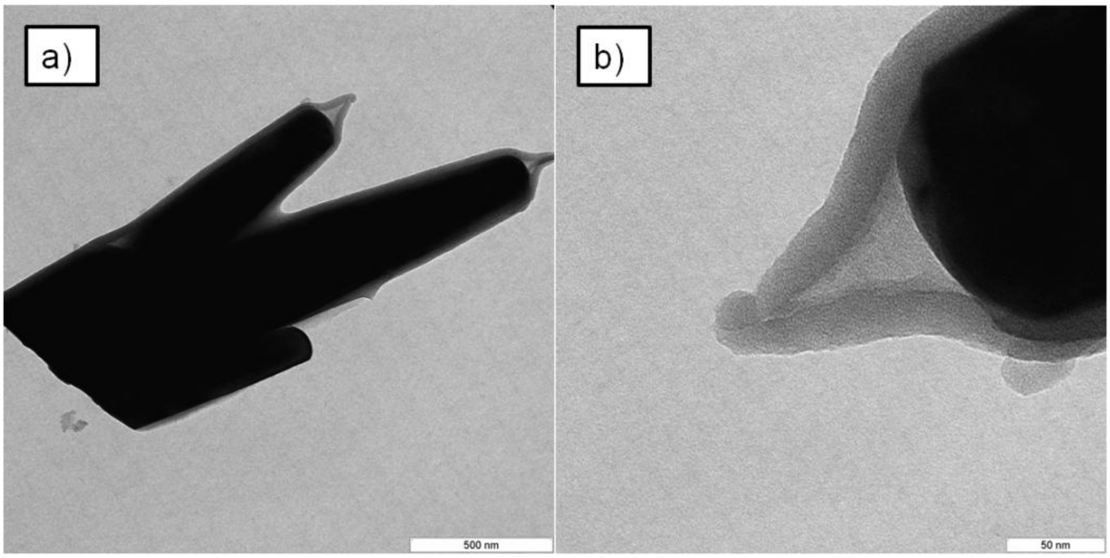

Figure 4.22 TEM images of carbon coated $LiCoPO_4$ mesocrystals: a) two primary needle-like $LiCoPO_4$ particles, b) thick carbon coating on the tip of one of the $LiCoPO_4$ particles.

4.7 Summary

In this chapter, a novel and simple template-free one-step solvothermal route for the fabrication of pristine and *in situ* carbon coated $LiFePO_4$ mesocrystals at low temperature (200 ^{o}C) has been described. Such a solvothermal method is easily scalable and could be a feasible and cost-effective substitution for the high-energy, multi-step solid-state technique commonly employed for the production of $LiFePO_4$. Moreover, the use of inexpensive and environmentally benign precursors offers a “green” manufacturing approach for large scale productions of $LiFePO_4$ cathodes.

All of the synthesized materials showed uniformity, high crystallinity and urchin-like morphologies. Such urchin-like morphology consisted of monodispersed spheres with a diameter ranging from 25 to 40 µm formed by micrometer sized self-assembled plate-like single crystalline primary particles with or without nano-sized carbon coating on their surface. N-acetylglucosamine has been found to be a suitable carbonizing agent for the coating of a nitrogen-containing amorphous conductive carbon layer. Additionally, it has been proven that this unusual and previously unreported morphology is directed simply by the presence of the Cl^- anions in the precursor solution and possibly occurred *via* solvothermal Ostwald ripening of amorphous dumbbell-like particles. Nevertheless, the final formation mechanism of the presented mesocrystals has not been fully developed, yet.

Suitable materials were selected and further treated under inert atmosphere at 700 ^oC for conductivity enhancement, followed by electrochemical testing as possible cathodes in lithium-ion batteries. The results showed that the carbon-coated $LiFePO_4$ mesocrystals delivered a stable specific capacity of ≈100 mA h g^{-1} at 0.1 *C* in comparison to a very low value of ≈25 mA h g^{-1} at 0.1 *C* for pristine $LiFePO_4$. Also, the polarization value between the charge and discharge curves for carbon-coated $LiFePO_4$ mesocrystals were notably lower in comparison to the pristine $LiFePO_4$. Thus, carbon coating plays the most important role in improving the electrochemical performance of the synthesized mesocrystals. However, the theoretical capacity and perfect cycling behaviour of $LiFePO_4$ could not be achieved due to materials imperfections such as inhomogeneous carbon coating, existence of Fe^{3+} as a substitute to preferable Fe^{2+} on the surface of the $LiFePO_4$ primary particles and chloride impurities in the bulk.

The original synthesis procedure described for $LiFePO_4$ could also be extended to the synthesis of other pristine and carbon coated phospho-olivines such as: $LiCoPO_4$ and $LiMnPO_4$, whose performance as lithium-ion cathode materials has not yet been fully explored.

5 Synthesis of nanostructured $LiFePO_4$

5.1 Introduction

Nanostructured materials and nanoparticles have triggered great excitement in the scientific community, especially in the last two decades, due to the unusual characteristics endowed by confined dimensions and the combination of bulk and surface properties to their overall behavior. In the context of energy applications, size reduction in nanocrystals leads to a variety of exciting occurrences as a result of improved surface-to-volume ratio and reduced scale of transport lengths for mass and charge, enabling high capacity, good Coulombic efficiency and high rate performance [136]. Recently, a lot of studies have been conducted towards the synthesis and application of nano active materials as electrodes in Li-ion batteries in order to increase the energy density beyond the currently achieved values [137, 138].

The advantages of using nanoparticles as electrode materials for Li-ion batteries are numerous. Firstly and most importantly, the reduced dimensions of nanoparticles shorten the Li^+ ion diffusion length which directly affects the rate capability and power density. The characteristic time constant for diffusion can be defined as $\tau = L^2/D_{\mathrm{Li}}$, where L is the Li^+ ion diffusion length reliant on the particle size, while D_{Li} is the diffusion coefficient dependant on the instinct of the intercalation material. Thus, as the time for the intercalation decreases with the square of the diffusion length, minimizing the particle size becomes an effective strategy for enhancing the rate of lithium insertion/removal [139]. On the other hand, as previously described for Li^+ ions, the electron transport in the intercalation material is additionally improved by the reduced dimensions of nanoparticles, which can affect the battery power performance [139]. Most of the cathode active materials are insulators, and generally a carbon additive is employed in order to improve the conductivity of the total electrode. If that is the case, the electron transport length L_e remains much higher than the particle size r, as only a few of the particles can obtain free electrons from the carbon additive due to the formation of particle agglomerates. Moreover, if carbon additives are used, the material's interface resistance remains quite high, as shown in Figure 5.1a.

The solution for electron transport problems therefore lies in combining nano-size particles with full conductive coating where agglomeration of the particles has no impact on the charge transport and $L_e = r$ (Figure 5.1b).

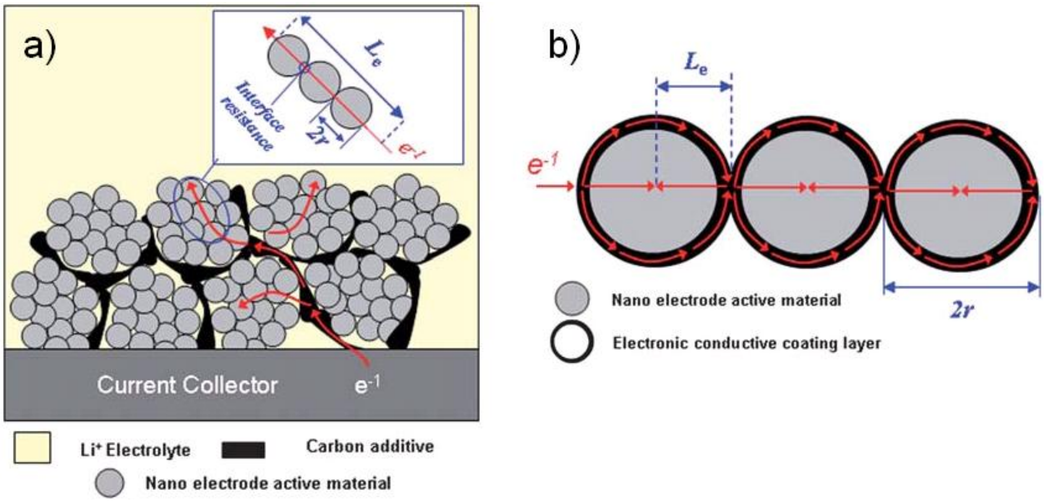

Figure 5.1 Schematic representations showing the electronic transport length L_e in nanoparticle based electrodes: a) carbon is used as a conductive additive, b) full conductive coating of a single nanoparticle is employed [137].

Additional advantages of using nanomaterials as Li-ion battery electrodes include high Li^+ ion flux across the interface between the electrolyte and the intercalation material due to high surface area, change of the reaction thermodynamics and electrode potential as a result of the modified chemical potential of nanoparticles and better accommodation of the intercalation strain allowing good cycling stability [140-142]. Finally, the employment of nanoparticles can enable electrode reactions that usually cannot take place in materials composed of the micrometer-sized particles [143].

However, there are certain drawbacks of using nanoparticles as electrodes in lithium-ion batteries. The majority of such nanoparticulate materials are synthesized using complicated multi-step high-temperature routes that cannot be easily extended to economically feasible industrial production. Moreover, the low densities of nanostructured electrode powders can limit the volumetric energy density of the final battery which is a very important property for their possible usage in lithium-batteries for electric vehicles (EVs) and hybrid electric vehicles (HEVs).

Furthermore, with nanostructured electrodes, there is a high possibility of undesired surface reactions, such as poor stability in the air atmosphere. All of the previously stated problems need to be asserted separately for each type of potential electrode material [144].

In the case of $LiFePO_4$, *ab*-initio calculations and atomistic studies showed that Li^+ ions move preferably along the *b*-axis rather than along *a*- or *c*-axes of the orthorhombic *Pnma* crystal [40, 41]. As recognized in theory, the Li^+ ion mobility in the intercalation compound determines the effective specific capacity through the volume ratio defined as $\eta = 1 - (1- L/r)^n$, where n is the dimension of the Li^+ ion mobility ($n = 1$ for LFP) [145]. Thus, for $LiFePO_4$ the reduction in particle size, especially along the *b*- or *c*-axis is a necessity for reaching theoretical capacity and high power energy storage. Moreover, as proven by Yamada *et. al.* [146, 147], $LiFePO_4$ exhibits size-dependent miscibility gap which is a general phenomenon related to the compounds with two-phase intercalation reactions.

In the last 10 years, a substantial effort has been done on improvement of the electrochemical performance of the $LiFePO_4$ cathode materials by implementing the ideas of tailored particle size and conductive coating. As early as in 2001, Nazar *et. al.* [49] prepared $LiFePO_4$/carbon nanocomposite *via* the solid-state reaction at high temperature which achieved ≈95% of the theoretical capacity at 0.1 *C* current rate. In 2006, Kim *et al.* [90] reported a polyol method for the synthesis of 50 nm long and 20 nm wide pristine nanoparticles of $LiFePO_4$ that exhibited ≈70% of the theoretical capacity at high current rate of 15 *C.* Furthermore, in 2008 Zhou *et al.* [45] reported an interesting *in situ* polymerization restriction method for synthesis of core-shell structures (20 nm in diameter) of $LiFePO_4$/carbon nanocomposite that achieved ≈55% of the theoretical capacity at a current rate of 60 *C* enabling high power performances. Most recently, in 2009, Ceder *et. al.* synthesized $LiFePO_4$ nanoparticles smaller than 50 nm coated with thin amorphous layer of $Li_4P_2O_7$ by ball-milling at high temperature with consequent remarkable full battery discharge in 10-20 s [148].

The following chapter presents a novel solvothermal synthesis route for acquiring pristine nanostructured $LiFePO_4$ and nanostructured $LiFePO_4$ *in situ* coated with a thin layer of carbon originating from different carbohydrate sources.

The obtained materials were characterized and compared by X-ray powder diffraction (XRD), Scanning electron microscopy (SEM), Transmission electron microscopy (TEM), and electrochemical charge-discharge measurements.

5.2 Synthesis

$LiFePO_4$ materials were synthesized using a solvothermal method similar to the one reported for $LiFePO_4$ mesocrystals (subchapter 4.2). In a typical procedure, firstly an appropriate amount (3 mmol) of granular metallic lithium (99%, Fluka) was dissolved in ethanol (20 mL) under mild mechanical stirring. During this step, precaution needs to be taken since lithium is highly reactive and the occurring dissolution reaction is exothermic. Subsequently, equimolar amounts (3 mmol) of Fe(II) acetylacetonate ($C_{10}H_{14}FeO_4$, 99%, Chemos) and H_3PO_4 (98 wt % solution in water, Sigma) were added to the previously cooled solution under vigorous mechanical stirring for half an hour. The obtained homogeneous, reddish-brown turbid solution was placed in a glass inlet of a Teflon® lined autoclave (Parr Instrument Company, 45 mL vessel size) which was then sealed and heated up in an oven to 200 ^{0}C for 24 h. The reactor was allowed to cool down to room temperature in a water bath and the supernatant was carefully decantated. The collected light brown precipitate was washed thoroughly with water until washings were colorless, followed by drying under vacuum at 60 ^{0}C overnight.

The nanostuctured $LiFePO_4$ materials could also be coated *in situ* with a thin layer of amorphous carbon using different carbon precursors – D-(+)-glucose monohydrate ($C_6H_{12}O_6 \cdot H_2O$, 99.5%, Roth, 0.30 g) and Chitosan (Poly-β(1→4)-N-acetylglucosamine, medium molecular weight, Aldrich, 0.15 g). In order to increase the crystallinity of the synthesized materials and the conductivity of the carbon containing samples, materials were fired in a muffle oven under nitrogen atmosphere with dwell time of 6 h at 700 ^{0}C. The final pristine nanostructured $LiFePO_4$ powder was fine and light brown, while the final $LiFePO_4$/carbon composites were solid chunks, hard and black in color. Carbon containing materials needed to be grinded manually for further characterization.

Additionally, the described solvothermal method was further extended to facilitate the synthesis of nanostructured $LiCoPO_4$ and $LiMnPO_4$ using Co(II) acetylacetonate ($C_{10}H_{14}CoO_4$, 99%, Alfa Aesar) and Mn(II) acetylacetonate ($C_{10}H_{14}MnO_4$, 99%, Alfa Aesar), respectfully.

5.3 Results and discussion

For convenience purposes the following notations will be used: nanostructured $LiFePO_4$ solvothermally synthesized at 200 ^oC and further annealed under nitrogen flow at 700 ^oC =nanoLFP$_{700}$; nanostructured $LiFePO_4$ solvothermally synthesized at 200 ^oC and further annealed under nitrogen flow at 700 ^oC in the presence of glucose as carbon precursor =nanoLFP@G$_{700}$; nanostructured $LiFePO_4$ solvothermally synthesized at 200 ^oC and further annealed under nitrogen flow at 700 ^oC in the presence of chitosan as carbon precursor =nanoLFP@Ch$_{700}$.

TEM micrographs of the nanoLFP$_{700}$ are presented in Figure 5.2 and reveal sheet-like structure, similarly to the previously reported primary sheets of the solvothermally synthesized mesocrystals of pristine $LiFePO_4$ (Chapter 4, Figure 4.5a).

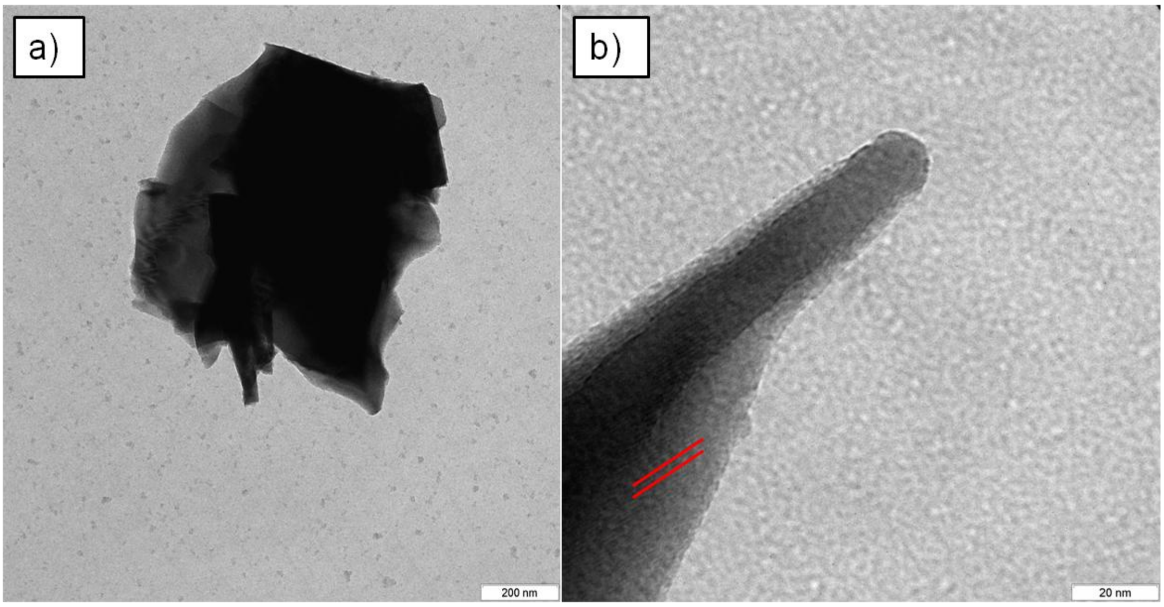

Figure 5.2 TEM images of pristine nano-sized $LiFePO_4$ synthesized solvothermally at 200 ^oC and further annealed under nitrogen flow at 700 ^oC (nanoLFP$_{700}$): a) overview of the aggregated sheet-like material, b) higher magnification image.

However, in this case, such obtained thin structures are smaller (less than 1 µm long and wide) and, more importantly, there is no 3D hierarchical ordering as proven by SEM (data not presented). Also, the sheets are agglomerated (stacked on top of each other) as visualized in Figure 5.2a, possibly due to sintering at higher temperatures. Looking at higher magnification micrograph of the nano-sheet edge (Figure 5.2b), clear lattice fringes can be observed, indicating high crystallinity of the material as confirmed later by XRD.

In the case of nanoLFP@G_{700}, a slightly different morphology has been been observed (Figure 5.3).

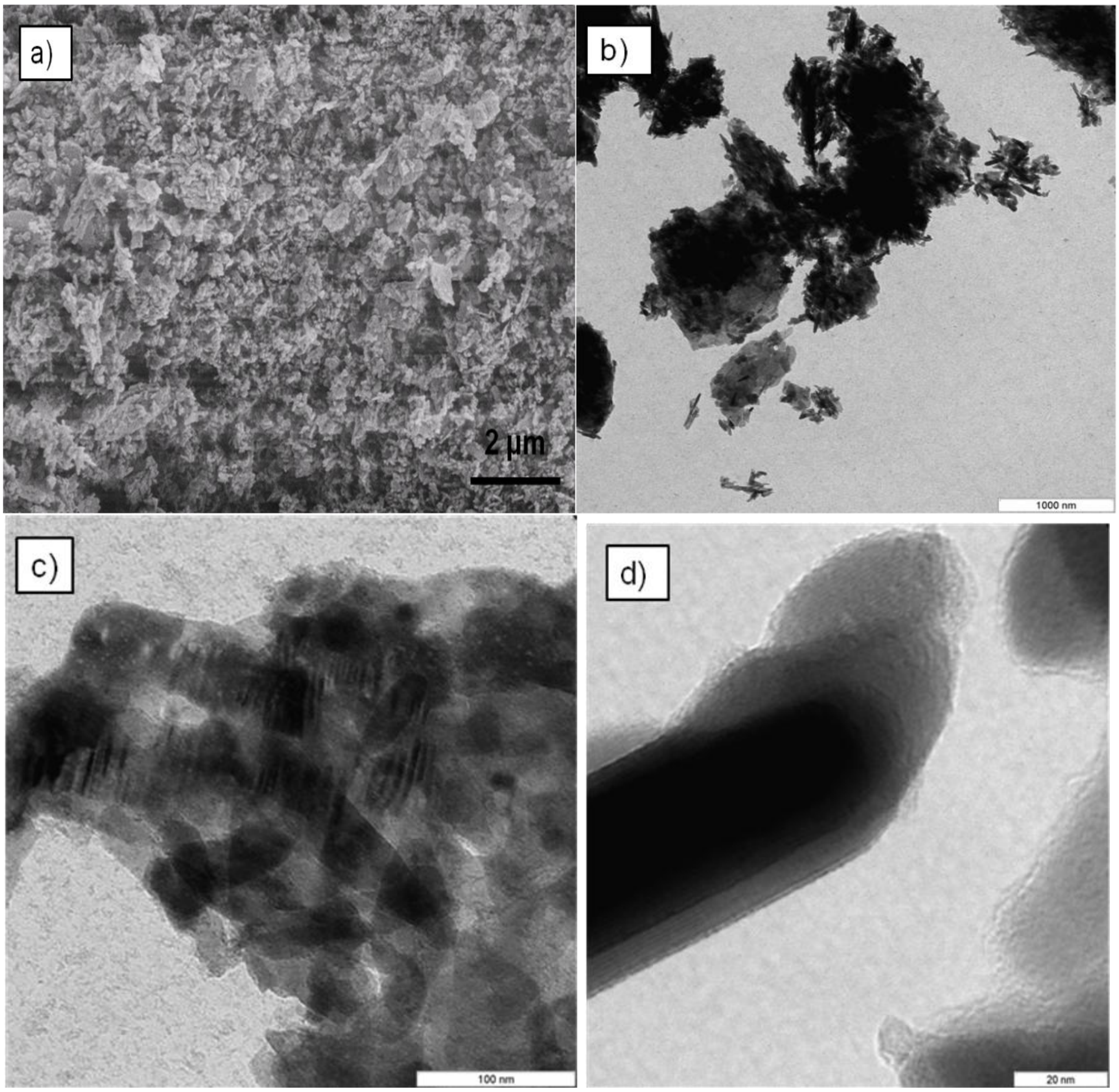

Figure 5.3 SEM and TEM micrographs of carbon containing (glucose originating) $LiFePO_4$ synthesized solvothermally at 200 ^oC and further annealed under nitrogen flow at 700 ^oC (nanoLFP@G_{700}): (a), (b) overview, (c) flake-like sheet structure, (d) carbon coated rod-like nanoparticle.

Again, this material does not self-assemble and has no micrometer-size ordering (Figure 5.3a) but consists of a mixture of randomly oriented and aggregated nanoparticles and thin flake-like sheets (Figure 5.3b). As seen for pristine $LiFePO_4$, the sheets of nanoLFP@G_{700} are mostly stacked on top of each other, thus Moire patterns are visible in higher magnification TEM micrographs due to their different orientations (Figure 5.3c).

No micrometer sized spherical particles can be observed in either SEM or TEM as it is common for amorphous carbons obtained *via* hydrothermal/solvothermal carbonization, suggesting that the carbon originating from glucose is located on the surface of the thin sheets/nanoparticles. This can be further assumed from the TEM micrograph of the rod-like nanoparticle at higher magnification (Figure 5.3d), from which amorphous carbon layer (gray in color) can be observed on its surface. The amorphous carbon coating has been confirmed by elemental analysis (12 wt %, more than one measurement in bulk suggesting evenly distributed coating). Also, it can be assumed that the amorphous carbon in nanoLFP@G_{700} acts as a repelling layer against sintering and thus not only sheet-like structures but also nanoparticles are formed.

X-ray diffractograms retreived for these materials are shown in the Figure 5.5.

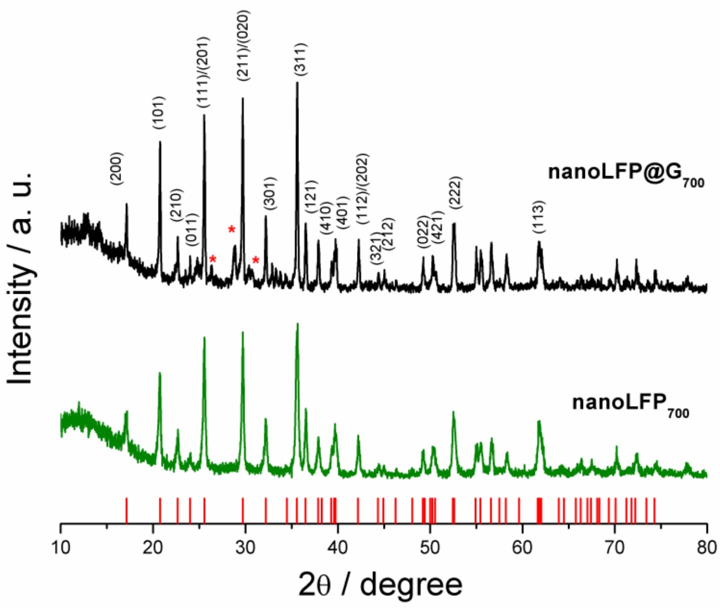

Figure 5.5 XRD patterns of pristine nanostructured $LiFePO_4$ and carbon coated (glucose originating) nanostructured $LiFePO_4$ materials synthesized solvothermally at 200 ^oC and further annealed under nitrogen flow at 700 ^oC.

The recorded Bragg diffraction peaks could be indexed on the basis of the orthorhombic *Pnma* space group indicating $LiFePO_4$ phase (red ticks denote the ICDD PDF No. 40.1499). In the case of pristine nanostructured $LiFePO_4$ (nanoLFP$_{700}$) no impurity phase has been detected. However, in the case of carbon coated (glucose originating, nanoLFP@G$_{700}$) sample additional peaks have been reported (denoted by the red asterisk) which correspond to the Li_3PO_4 phase typically appearing as a result of solvothermal/hydrothermal route. No carbon reflection peaks have been observed for the nanoLFP@G$_{700}$ due to its amorphous nature and low content in comparison to the $LiFePO_4$ phase. An important feature of the presented XRD patterns is the intensity ratio of the peaks which corresponds to the preferred crystal alignment of the $LiFePO_4$ particles [149]. In both cases the (311) peak intensity was the strongest.

It is worth mentioning that the uncalcined materials (straight after solvothermal treatment for 24h at 200 ^oC) also exhibit pure and well developed crystallinity (narrow peaks of high intensity) as well as the nanostructured morphology. This data is not presented in this thesis given that those materials have not been tested as potential lithium-ion battery cathodes.

Figure 5.6 shows SEM micrographs of the nanoLFP@Ch$_{700}$ at two different magnifications. The material consists of randomly aggregated clusters of small nanoparticles (Figure 5.6b).

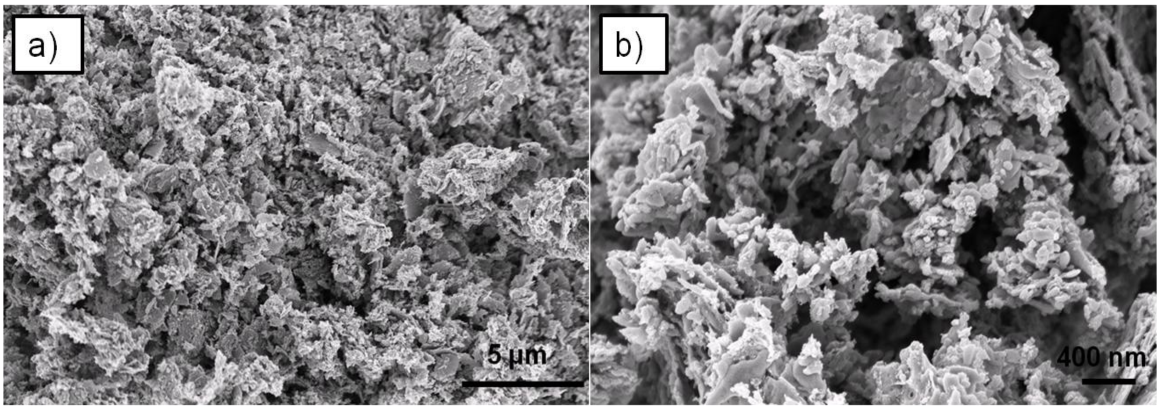

Figure 5.6 SEM micrographs of carbon coated (chitosan originating) $LiFePO_4$ synthesized solvothermally at 200 ^oC and further annealed under nitrogen flow at 700 ^oC (nanoLFP@Ch$_{700}$): a) overview of the material, b) aggregated nanoparticles.

This material showed better morphology and discrete rod-like morphology, therefore a more detailed structural study has been performed.

From the TEM images (Figure 5.7a and b) it is clear that the aggregated nanoparticles of $LiFePO_4$ are arbitrarily oriented and uniform. The morphology of nanoLFP@Ch_{700} is considerably different from the previously shown pristine nanostructured $LiFePO_4$ (LFP_{700}) with homogeneous, well-defined and regular rod-like particles.

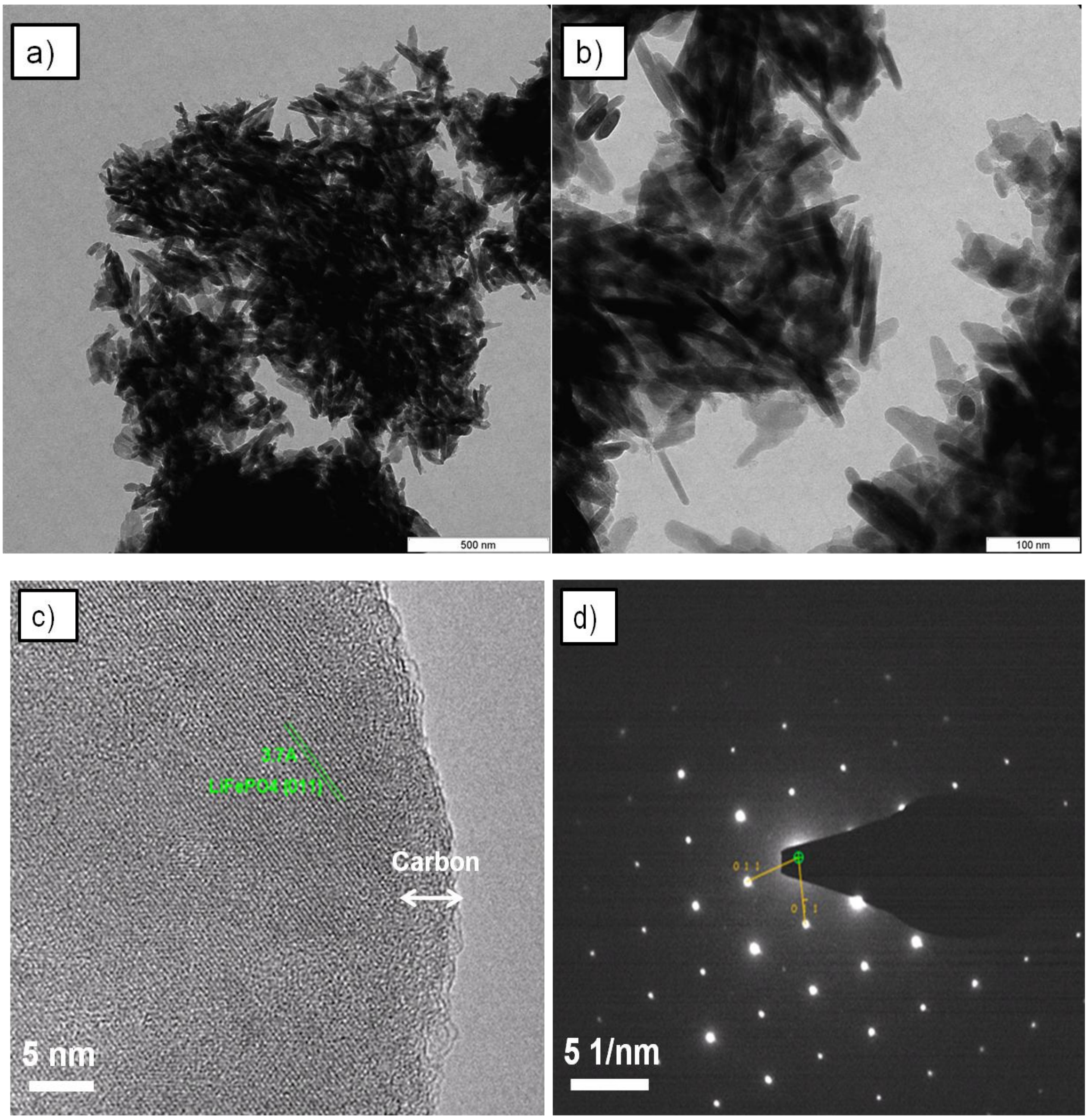

Figure 5.7 TEM and HR-TEM of carbon coated (chitosan originating) $LiFePO_4$ synthesized solvothermally at 200 ^{0}C and further annealed under nitrogen flow at 700 ^{0}C (nanoLFP@Ch_{700}): a) overview of the material, b) aggregated rod-like nanoparticles of $LiFePO_{4,}$ c) uniform carbon coating on the surface of one of the rod-like nanoparticles shown in b), d) SAED of one of the rod-like nanoparticles shown in b).

As stated in the case of nanoLFP@G_{700}, carbon acts as a repelling layer towards sintering of the nanostructured material. In the case of nanoLFP@Ch_{700} the tendency of a formation of more dispersed particles is similar. However, potentially present nitrogen-containing groups on the surface of the amorphous carbon coating (originating from chitosan) could be even more successful in stabilization of the nanorod particles. Such nanorod-like morphology is very attractive to achieve fast Li^+ ion diffusion for high rate capability [44]. More detailed account on the formation of carbon layer on the surface of $LiFePO_4$ nanorods will be given later on (Chapter 5.3).

Higher magnification TEM (Figure 5.7b) reveals that the rod-like nanoparticles are mostly 100 nm long and approximately 10 nm wide, with a minor amount of smaller nanoparticles noticable (50 nm long, 15-20 nm wide). In addition, it can be also concluded from the TEM micrograph on the Figure 5.7b that the nanoparticles are very thin and can be considered two-dimensional.

Figure 5.7c is a HR-TEM micrograph of the surface and inner core of one rod-like nanoparticle and clearly shows uniform, ≈5 nm thick amorphous carbon coating layer. The existence of nitrogen-doped carbon coating has been further confirmed by elemental analysis (12 wt % C and 1.5 wt % N, more than one measurement in the bulk, suggesting good coating) and XPS analysis (Figure 5.9). The distance between the lattice fringes, *d*, visible in Figure 5.7c is calculated to be 3.7Å and corresponds to (011) plane of olivine $LiFePO_4$.

The olivine structure is confirmed by the SAED pattern shown on Figure 5.7d where rectangular diffraction spot array signify that the rod-like nanoparticles are indeed single crystalline. All of the diffraction spots could be indexed to the olivine $LiFePO_4$ reciprocal lattice. No impurity phase has been detected as confirmed by XRD later on (Figure 5.9). The SAED pattern is taken close to the [100] zone axis which means that the thin side of the nanoparticle is along the [100] – direction, which is similar to the orientation of the primary sheets of $LiFePO_4$ mesocrystals reported shown in Chapter 4 (Figure 4.6). This is possibly due to the analogous synthesis route.

However, here presented thin, rod-like nanoparticles are in comparison to the primary sheets of $LiFePO_4$ mesocrystals smaller in size (100 nm vs. several tens of µm), highly pure (no chlorine or Li_3PO_4 related impurities), have uniform carbon layer on their surface (5 nm vs. 10 nm) and do not exhibit structural holes as a result of solvent evaporation during solvothermal reaction.

EDX chemical mapping has been performed to evaluate the elemental content of nanoLFP@Ch_{700}. Figure 5.8 shows presence of atoms which are all related to the carbon coated $LiFePO_4$ nanocomposite.

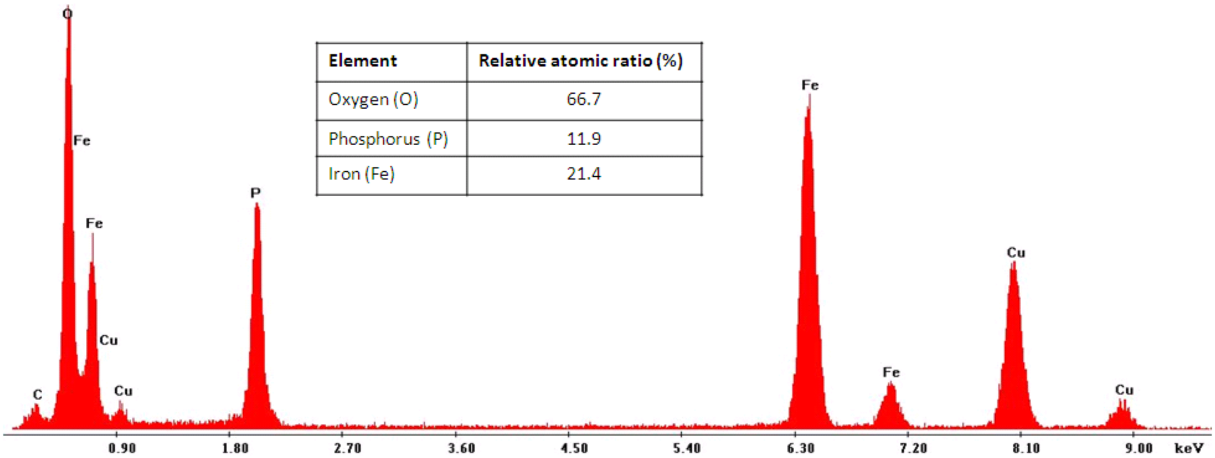

Element	Relative atomic ratio (%)
Oxygen (O)	66.7
Phosphorus (P)	11.9
Iron (Fe)	21.4

Figure 5.8 EDX of carbon coated (chitosan originating) $LiFePO_4$ nanoparticle synthesized solvothermally at 200 ^{0}C and further annealed under nitrogen flow at 700 ^{0}C (nanoLFP@Ch_{700}).

Nevertheless, relative atomic ratios of oxygen, phosphorus and iron are slightly off stoichiometry (O : P : Fe = 66.7% : 11.9% : 21.4%), possibly due to the instrument imprecision. The copper peak which does not correspond to the as synthesized material is visible as a result of placing the nanoLFP@Ch_{700} sample on a TEM copper containing grid as a sample holder.

The XRD patterns of carbon (chitosan originating) coated $LiFePO_4$ synthesized solvothermally at 200 ^{0}C (nanoLFP@Ch_{200}, green line) and further annealed under nitrogen flow at 700 ^{0}C (nanoLFP@Ch_{700}, black line) are presented in the Figure 5.9.

As it can be seen from the figure, all presented peaks could be indexed to an orthorhombic olivine *Pnma* space group (ICDD PDF No. 40.1499, represented by red vertical ticks), with no impurity phases present.

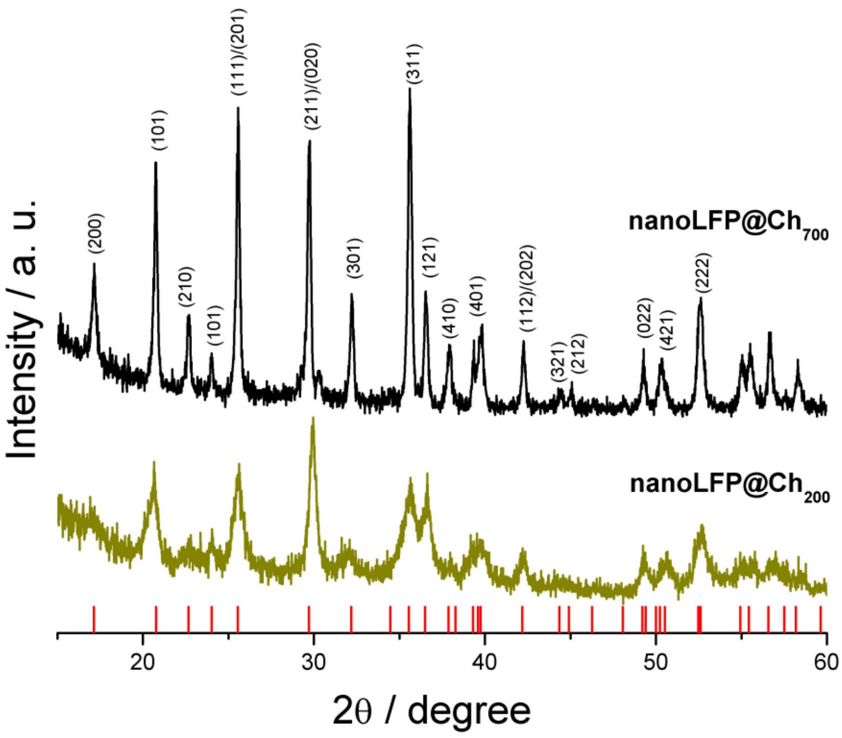

Figure 5.9 XRD patterns of carbon coated (chitosan originating) $LiFePO_4$ synthesized solvothermally at 200 ^oC (nanoLFP@Ch_{200}) and further annealed under nitrogen flow at 700 ^oC (nanoLFP@Ch_{700}).

The full crystallinity of the rod-like nanoparticles develops after a 24 hour long solvothermal process at a low temperature of 200 ^oC. The XRD peaks of nanoLFP@Ch_{200} are broader and of lower intensity suggesting smaller particle size, while the reflection peaks of nanoLFP@Ch_{700} are narrower and of higher intensity due to the sintering effects at higher temperatures.

Comparing the intensity of the Bragg's diffraction peaks of nanoLFP@Ch_{200} and nanoLFP@Ch_{700}, it can be observed that the preferred orientation of the crystals changes during the post-treatment ((111), (020) and (311) peaks).

Interestingly, as previously pointed out for mesocrystalline LFP_{200} and LFP_{700} (Figure 4.8), the intensity ratio of I(200)/I(020) peaks once more suggests sheet-like structures as it is confirmed by TEM of aggregated nanoparticles (Figure 5.7b). No visible carbon peaks have been recorded, due to its amorphous nature and low content.

Full profile matching of the $nanoLFP@Ch_{700}$ using Fullprof® software showed no impurities and good agreement with the theoretical data (Figure 5.10).

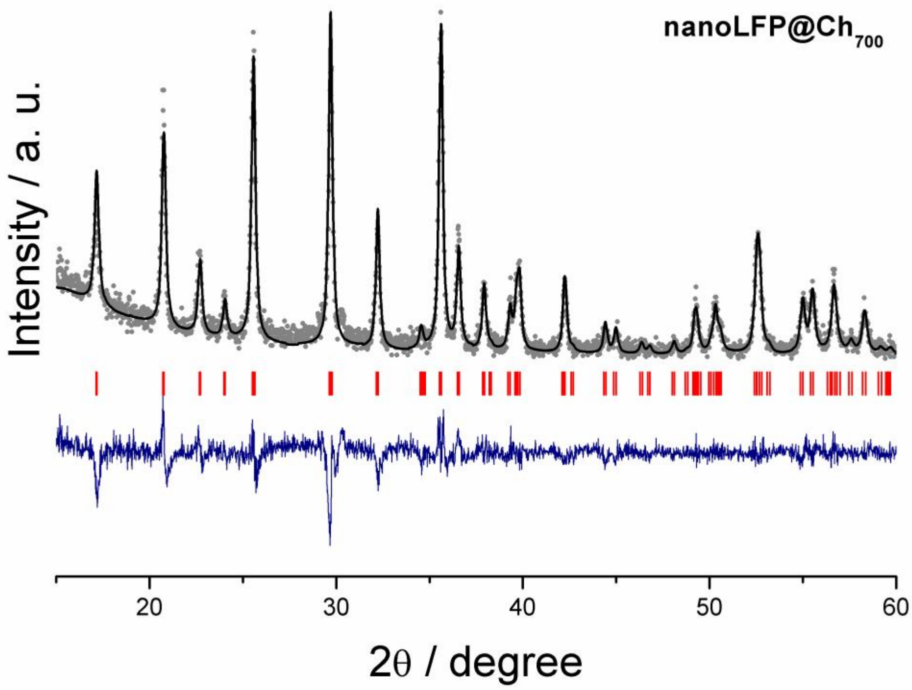

Figure 5.10 XRD profile matching refinement of carbon coated of carbon coated (chitosan originating) $LiFePO_4$ synthesized solvothermally at 200 ^0C and further annealed under nitrogen flow at 700 ^0C ($nanoLFP@Ch_{700}$). Experimental data is represented by gray dots. Blue line corresponds to the difference between observed and calculated pattern of $nanoLFP@Ch_{700}$.

The experimental intensity data are shown by the gray dotted line. Solid black line corresponds to the calculated pattern of $LiFePO_4$. The bottom blue line matches up with the difference between the observed and calculated pattern of $LiFePO_4$. Red vertical ticks denote the Bragg positions of $LiFePO_4$ (ICDD PDF No. 40-1499).

The calculated lattice parameters are: a = 10.32237 Å, b = 6.00089 Å, c = 4.69588 Å, with a final unit volume of V = 290.87 $Å^3$ which is slightly lower than of the mesocrystalline carbon coated counterpart (Chapter 4, Figure 4.9) and closer to the theoretical values for the fully stoichiometric, non-defective $LiFePO_4$ [150].

A notable difference between mesocrystalline LFP@C_{700} and nanoLFP@Ch_{700} can be observed comparing the intensity of the (211) peak located around $2\theta = 30^o$ and the orientation of the blue line on both graphs (Fugure 4.9 and Figure 5.10).

As previously pointed out, the oxidation state of iron in $LiFePO_4$ (Fe^{2+} vs. Fe^{3+}) as well as the type of carbon deposited on its surface (sp^2 vs. sp^3) plays a very important role for the battery performance of this type of material. Additionally, important question needs to be answered regarding the way nitrogen is incorporated into the carbon structure.

Figure 5.11 shows C 1s, Fe 2p and N 1s high resolution XPS spectra together with their corresponding energies (BE) for nanoLFP@Ch_{700}. From the C 1s spectra (Figure 5.11a), it can be concluded that the carbon phase in the composite material is predominately sp^2 hybridized carbon (BE = 284.99 eV) as previously reported for solvothermally synthesized carbon coated $LiFePO_4$ mesocrystals in the Chapter 4 (Figure 4.10). Oxygenated surface groups are also present here (BE = 286.41 eV). The main and important difference is however the detection of nitrogen in the C 1s XPS spectra in the form of N-C=O groups (BE = 288.30 eV).

The spectrum of Fe $2p_{3/2}$ (Figure 5.11b), can be deconvoluted into a component at BE = 710.01 eV (Fe $2p_{3/2}$ (1)) corresponding to Fe^{2+} and a component at BE = 711.64 eV (Fe $2p_{3/2}$ (2)), indicating the presence of Fe^{3+} ions on the surface of LFP@Ch_{700} composite. The energy separation between these two peaks is in good agreement with the literature, while the peak intensities indicate that there is more Fe^{3+} then Fe^{2+} species present at the surface of the synthesized material. These findings are almost identical to the ones presented in Chapter 4 (Figure 4.10).

To additionally prove the existence of nitrogen in the $LiFePO_4$/C composite, N 1s spectra was obtained. As seen from Figure 5.11 the spectrum of N 1s contains multiple components due to the coexistence of different chemical states of nitrogen.

Thus, it can be deconvoluted into three peaks: the peaks at binding energies of 398.96 eV (N1s(1)), 401.25 eV (N1s(2)), and 403.50 eV (N1s(3) which can be attributed to the C–N, C=N, and N–O bonds, respectively. Additionally, the possibility of the existence of the C≡N bond cannot be excluded, because its binding energy is close to that of the C–N bond. These results are similar to the findings from a recent publication dealing with $Li_4Ti_5O_{12}$ coated with nitrogen-doped carbon originating from ionic liquids [151].

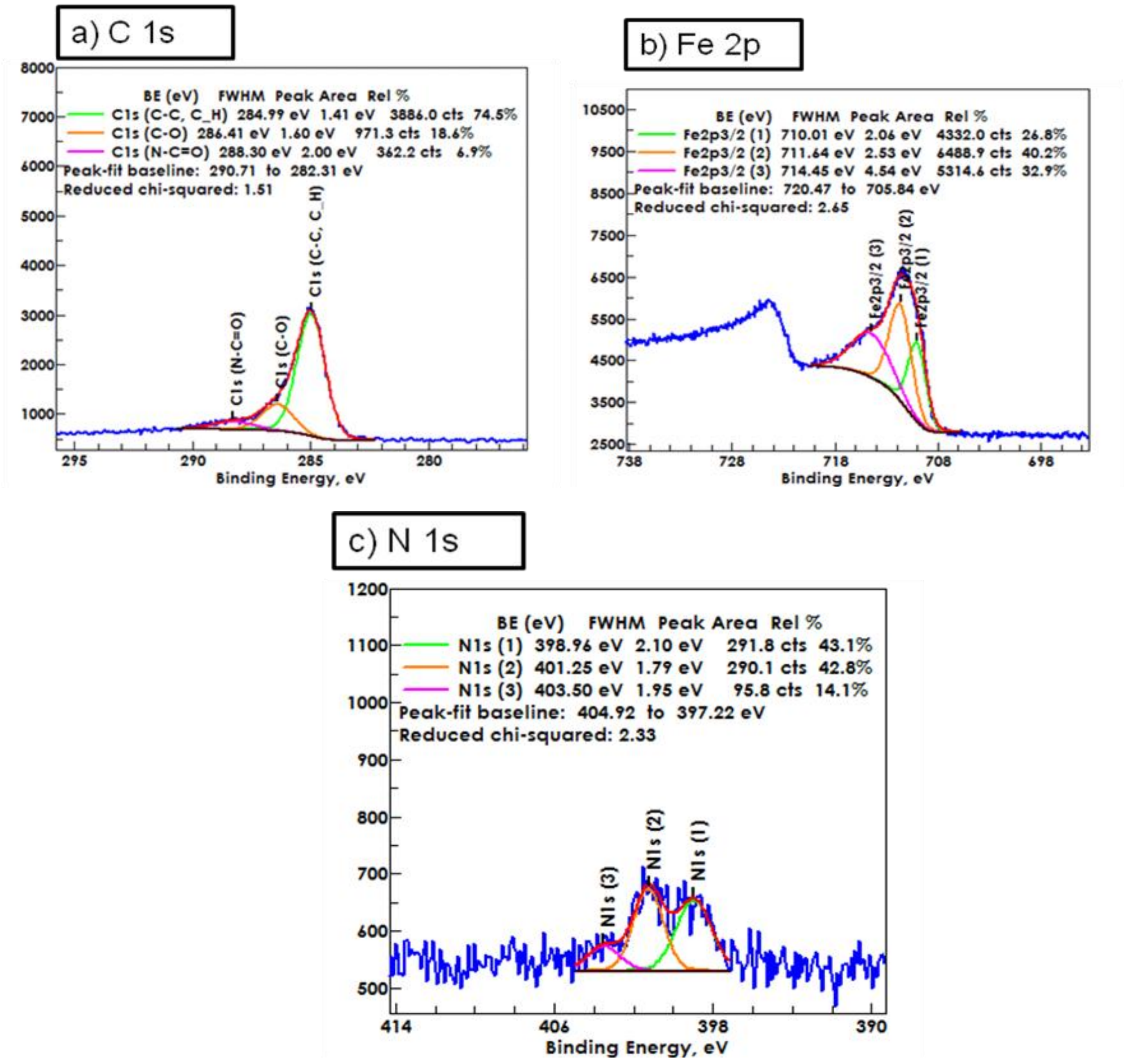

Figure 5.11 HR-XPS of the nitrogen-doped carbon coated LiFePO$_4$ mesocrystals synthesized solvothermally at 200 °C (LFP$_{200}$) and further annealed under nitrogen flow at 700 °C (LFP@Ch$_{700}$: a) C 1(s), (b) Fe 2(p) and (c) N 1(s) envelopes.

Finally, the porosity of synthesized nanoLFP@Ch_{700} has been tested using nitrogen adsorption/desorption experiments. The BET isotherm (Figure 5.12) shows porosity typically seen in the case of aggregated randomly oriented nanoparticles (Type IV with low hysteresis, IUPAC). The calculated BET surface area is S_{BET} = 58 m^2 g^{-1}, which is considerably higher than the BET surface area of the previously reported mesocrystalline LFP@C_{700} (S_{BET} = 18 m^2 g^{-1} from the Figure 4.13, Chapter 4). The theoretical density of $LiFePO_4$ is 3.6 g cm^{-3}.

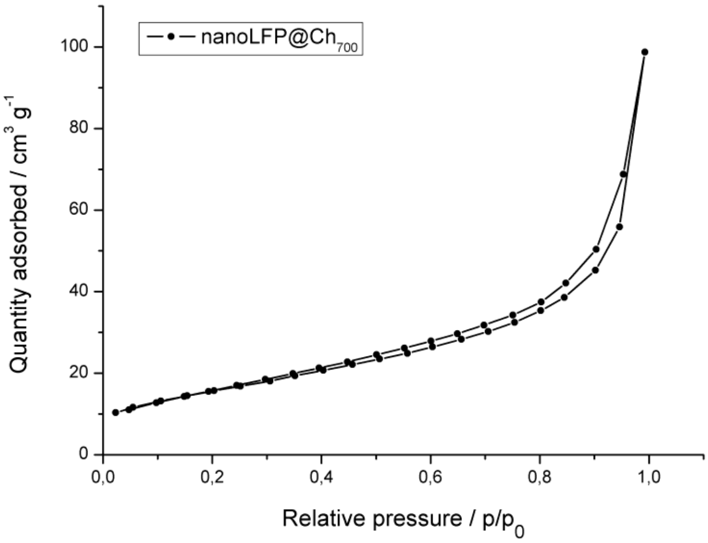

Figure 5.12 BET nitrogen sorption isotherm of carbon coated of carbon coated (chitosan originating) $LiFePO_4$ synthesized solvothermally at 200 ^oC and further annealed under nitrogen flow at 700 ^oC (nanoLFP@Ch_{700}).

It is important to state that the yield of $LiFePO_4$, calculated as the conversion ratio of Fe^{2+} from Fe(II) acetylacetonate precursor, was more than 90% in the case of all of the materials reported in this chapter. The yield is highly dependent on the acidic conditions of the primary solution as published for hydrothermal synthesis of $LiFePO_4$ by Kanamura *et al.* [149]. For the presented materials, the value of pH in the precursor solution both with and without carbon precursor was ≈5, which is over the critical pH = 4 where the solubility of $LiFePO_4$ is considerably high on elevated temperatures.

This is an improvement in comparison to the yield of mesocrystals of $LiFePO_4$ reported in the Chapter 4 which exhibited an yield as low as 50% due to very low pH values in the precursor solution (pH ≈ 1.5, measured in ethanol) as a consequence of utilizing highly acidic $FeCl_2 \cdot 4H_2O$ as a Fe^{2+} precursor.

5.4 The proposed mechanism of carbon coating formation

The importance of the carbon coating nature and its quality for the electrochemical performance of $LiFePO_4$ is considerable and has been assessed in the theoretical introduction of this thesis (Chapter 2). For the synthesis of novel nanostructured $LiFePO_4$ *in situ* coated with amorphous carbon *via* the solvothermal carbonization, two different precursors have been used (Figure 5.13).

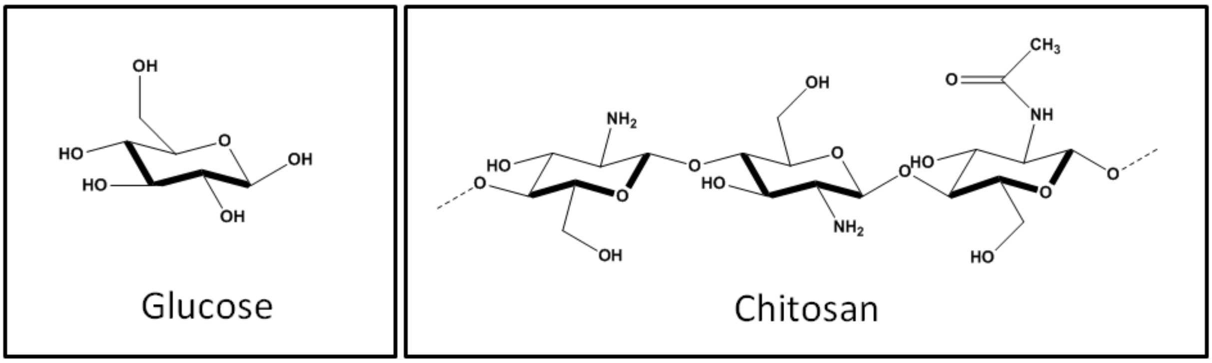

Figure 5.13 Carbon containing precursors used for *in situ* coating of nanostructured $LiFePO_4$.

Firstly, glucose was chosen as a most abundant monosaccharide and a reducing sugar suitable as a model carbon-coating system. It has been already documented by Titirici group at Max Planck Institute of Colloids and Interfaces that during hydrothermal carbonization (HTC = autoclave treatment in aqueous solution at 180 ^{o}C under inborn pressure of ≈10 bar) glucose undergoes dehydration leading to 5-hydroxymethylfurfural-2-furaldehyde (HMF). Further on, HMF separates from the solution and disperses, forming nuclei of oligomers which grow to larger particles in a process similar to emulsion polymerization [152].

As a result of polymerization process, the final hydrothermal carbonaceous material originating from glucose consists of uniform interconnected spheres.

Here, however, carbonization of glucose is held in another solvent (ethanol) and an additional faster reaction is taking place (crystallization of $LiFePO_4$ from dissolved LiOH, Fe(II) acetylacetonate and H_3PO_4). Thus, the dehydration of glucose into HMF is only promoted by the 3 water molecules released from glucose at 180 ^{0}C, under acidic conditions. Therefore, the amount of HMF is much lower but enough to coat a thin layer of carbon around the particles instead of forming individual carbonaceous particles as usually seen in hydrothermal/solvothermal carbonization. Consequently, carbonaceous coating outlines the preformed $LiFePO_4$ and allows intimate contact between inorganic and organic phase on a nano level which is required for good ionic and electronic conductivity of the $LiFePO_4$/carbon composite materials.

However, the usage of glucose did not facilitate fabrication of desirable uniform monodispersed particles but a mixture of large sheet-like structures and nanoparticles. This possibly happens due to the fact that the previously described carbon coating has polar functional groups on the surface which can interact with each other by H-bonding and lead to slight aggregation.

Finally, chitosan has been employed as an inexpensive and readily available nitrogen containing polysaccharide derived from chitin which is a structural element in the exoskeleton of crustaceans (crabs, shrimp, lobster, etc.). Under hydrothermal conditions, unlike glucose, chitosan forms HMF in smaller amount and nitrogen containing heterocycles (amines) in larger amount due to release of ammonia to the HTC solution [76]. The transformation process of chitosan towards nitrogen containing amorphous carbon is more complex and involves Maillard-type reactions as well as polymerization and aromatization.

In the presented solvothermal synthesis of nanoLFP@Ch_{700}, it appears that the dehydratation of chitosan formed in the first step of its carbonization process stabilizes initially formed nanoparticles of $LiFePO_4$ and suppresses their growth to sheet-like structure.

The presence of small amount of nitrogen in the final material (1.5 wt%) and N-C=O groups in the amorphous carbon coating as shown by XPS direct the formation of uniform and small nanorod-like particles.

5.5 Li^+ insertion/extraction measurements

A detailed study of the electrochemical properties of pristine $nanoLFP_{700}$, $nanoLFP@G_{700}$ and $nanoLFP@Ch_{700}$ as cathodes for lithium-ion batteries was performed. For the electrochemical experiments, two-electrode Swagelok-type™ cells and pure lithium foil as a counter/reference electrode were used.

Figure 5.14 a), c) and e) shows the results of galvanostatic cycling experiments for the pristine $nanoLFP_{700}$, $nanoLFP@G_{700}$ and $nanoLFP@Ch_{700}$ so as to address the effect of morphology, texture and carbon content on the voltage-composition curves. All of the voltage-composition profiles match up to the first cycle of the charge/discharge in the cut-off voltage 2.0-4.3 V at 0.1 *C* current density (which corresponds to the current required to completely charge/discharge an electrode in 10 h, 1 *C* = 170 mA h g^{-1}). In all cases, typical $LiFePO_4$ voltage-composition curve is visible, with two very flat plateaus for both charge and discharge. This electrochemical behavior corresponds to the Li^+ ion extraction/insertion from/into crystallographic structure of $LiFePO_4$ with the redox of $Fe^{2+/3+}$, suggesting two-phase intercalation mechanism [146].

From the Figure 5.14a, a relatively high polarization for the first cycle is evident ($\Delta V \approx 0.25$ V), indicating slow kinetics of the pristine $nanoLFP_{700}$. This symmetrical hysteretic behavior is due to the fact that in an assembled Swagelok cell® we have many individual particles that are connected to each other so fast exchange of lithium between them is possible [108]. The polarization value in the first cycle is however reduced to ΔV = 0.115 V in $nanoLFP@G_{700}$ and ΔV = 0.0075 V in $nanoLFP@Ch_{700}$ (Figure 5.14c and e). This is possibly the consequence of enhanced conductivity of the nano-sized $LiFePO_4$ by introducing *in situ* synthesized amorphous carbon on its surface. In the case of $nanoLFP@G_{700}$, which has a mixed morphology (nano-sheets and nanoparticles, Figure 5.4), carbon coating generated by solvothermal carbonization of glucose is possibly not homogeneous.

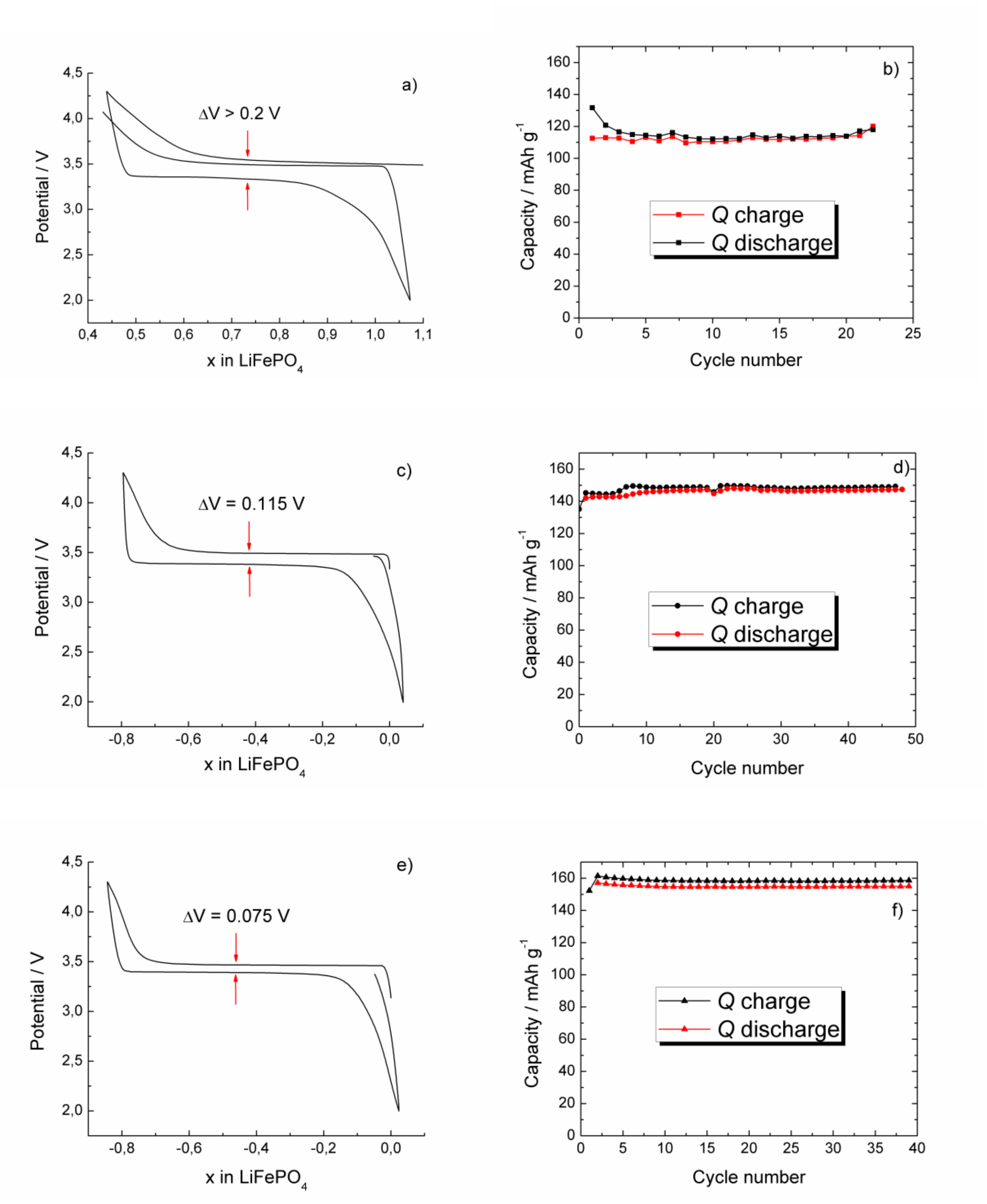

Figure 5.14 Electrochemical properties of nanoLFP$_{700}$, nanoLFP@G$_{700}$ and nanoLFP@Ch$_{700}$: (a), (c), (e) voltage-composition profiles for the first Li insertion cycle of the nanoLFP$_{700}$, nanoLFP@G$_{700}$ and nanoLFP@Ch$_{700}$ at C/10 current density, (b), (d), (f) charge-discharge capacity vs. cycle number for nanoLFP$_{700}$, nanoLFP@G$_{700}$ and nanoLFP@Ch$_{700}$.

On the other hand, nanoLFP@Ch_{700} consists of highly uniform aggregated thin rod-like nanoparticles with full nitrogen-containing carbon coating of every particular nanoparticle produced by solvothermal carbonization of chitosan. These ≈5 nm thick carbon layers around the particles act as ionic and electronic "wires" for improved kinetics of Li^+ intercalation/deintercalation and electron transport. It is not clear whether the small amount of nitrogen (1.5 wt %) increases the conductivity of the nanoLFP@Ch_{700} or simply helps obtaining more uniform morphology, the second case being more probable. Also, it can be estimated that the polarization value of nanoLFP@Ch_{700} is very low due to the existence of 2 wt % of nitrogen incorporated in the carbon outer shell of every single nanoparticle. Thus, the voltage-composition profile of nanoLFP@Ch_{700} becomes very close to the desirable theoretical profile of the perfectly crystalline $LiFePO_4$ with zero polarization.

After evaluating charge/discharge capacities (Figure 5.14 b), d) and f)), it can observed that the capacity of the pristine nanoLFP$_{700}$ is ≈120 mA h g^{-1} at 0.1 *C* (71% of the theoretical capacity) which is incomparably better then of the pristine mesocrystalline LFP$_{700}$ shown in the Chapter 4 (Figure 4.16) with the capacity of ≈25 mA h g^{-1} at 0.1 *C* (15% of the theoretical capacity). This is above all due to the smaller particle size (nano in comparison to micro) which has a considerable effect on the Li^+ ion mobility. Moreover, in the case of nanoLFP$_{700}$ prolonged cycling is possible, the difference between charge and discharge capacity is negligible and the obtained capacity is stable.

Carbon containing nano $LiFePO_4$ exhibits improved charge/discharge capacities in comparison to the pristine $LiFePO_4$ and no "activation" process can be observed in the first cycle as for the mesocrystalline LFP@C_{700} (Figure 5.14 d) and f)). The capacity of nanoLFP@G_{700} is ≈150 mA h g^{-1} at 0.1 *C* (88% of the theoretical capacity, Figure 5.14d), with a nicely flat charge/discharge curves proving good cyclability. In the case of nanoLFP@Ch_{700}, nearly theoretical capacity is reached with values of ≈160 mA h g^{-1} at 0.1 *C* (94% of the theoretical capacity, Figure 5.14f) with perfect cyclability. This material offers a good prospect to be used as a potential improved cathode for lithium-ion batteries. However, additional and more detailed electrochemical experiments such as rate performance need to be performed to assess possible commercial application of the nanoLFP@Ch_{700}.

In conclusion, the presented electrochemical tests of nanoLFP$_{700}$, nanoLFP@G$_{700}$ and nanoLFP@Ch$_{700}$ clearly show the importance of nano-size for the cycling capability of $LiFePO_4$, the importance of uniform core-shell morphology as well as the possible influence of nitrogen-doping of the carbon coating on the almost theoretical performance of the nanoLFP@Ch$_{700}$.

5.6 Extension to other $LiMPO_4$

As in the previous chapter, the here presented solvothermal route at 200 ^{o}C can also be extended towards the synthesis of other nanoparticulate $LiMPO_4$ using suitable transition metal acetylacetonates as M^{2+} sources.

Figure 5.15 shows TEM micrographs of nanoparticulate $LiCoPO_4$ straight after the solvothermal treatment. There are no visible larger sheets of crystalline material as seen for the nanostructured $LiFePO_4$. The pristine $LiCoPO_4$ (Figure 5.15a and b) consists of aggregated thumb-like, non-uniform and flake-like nanoparticles that are less than 100 nm long and 50 nm wide. From here presented TEMs, it is visible that the nanoparticles end with a thin layer of amorphous phase (≈5 nm) which is confirmed by XRD further on (Figure 5.17).

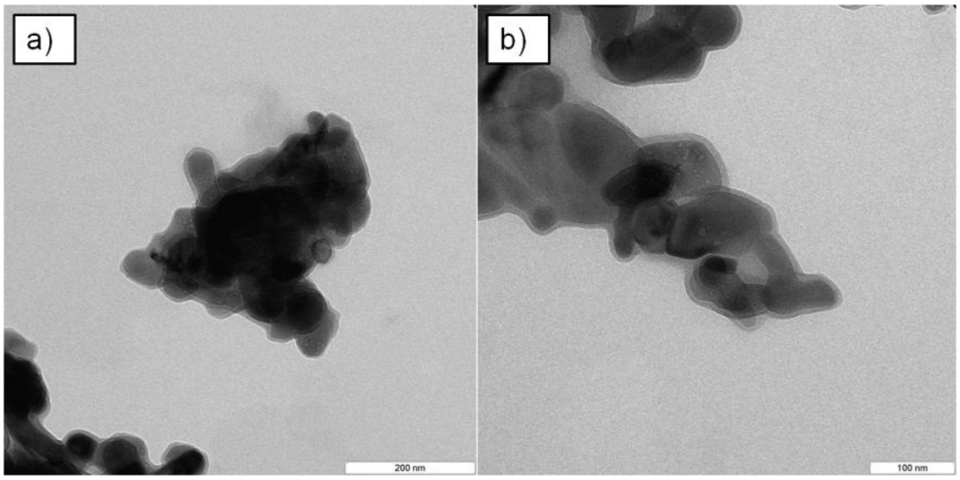

Figure 5.15 TEM images of pristine nanostructured $LiCoPO_4$ synthesized solvothermally at 200 ^{o}C.

TEM micrographs of the pristine $LiMnPO_4$ reveal sheet-like particles with rather non-uniform morphology (Figure 5.16). Most of the sheets are of a several hundred nm in size with some smaller nanoparticles 50-200 nm in size also present (Figure 5.16b). On the surface of the sheets, small holes (diameter of 10 nm and less) are visible, possibly as a consequence of the synthesis technique (evaporation of the solvent during solvothermal synthesis).

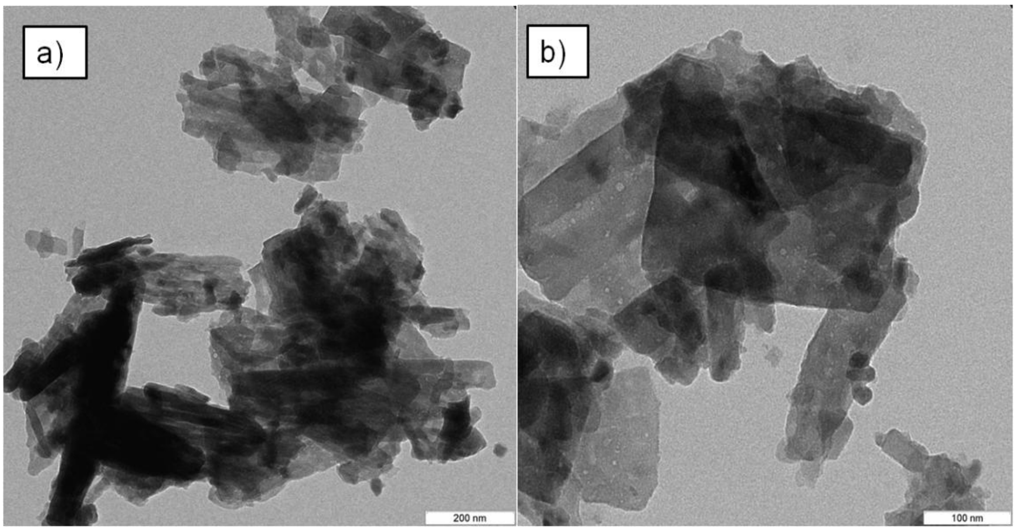

Figure 5.16 TEM images of pristine $LiMnPO_4$ synthesized solvothermally at 200 ^oC and two different magnifications.

Figure 5.17 shows the corresponding XRD patterns of the previously visualized pristine $LiCoPO_4$ and $LiMnPO_4$ after solvothermal treatment at 200 ^oC. All of the obtained peaks are sharp and narrow indicating highly crystalline material. The peaks could be indexed on the basis of the orthorhombic olivine structure, Pnma space group with no crystalline impurity phases visible. At approximately $2\theta = 12.5^o$, broad peaks are detected for both $LiCoPO_4$ and $LiMnPO_4$ indicating existence of an amorphous phase. The reflections gradually shift to higher angles ongoing from Co to Mn due to increase in ionic radii values, as previously reported for $LiCoPO_4$ and $LiMnPO_4$ mesocrystals (Figure 4.21).

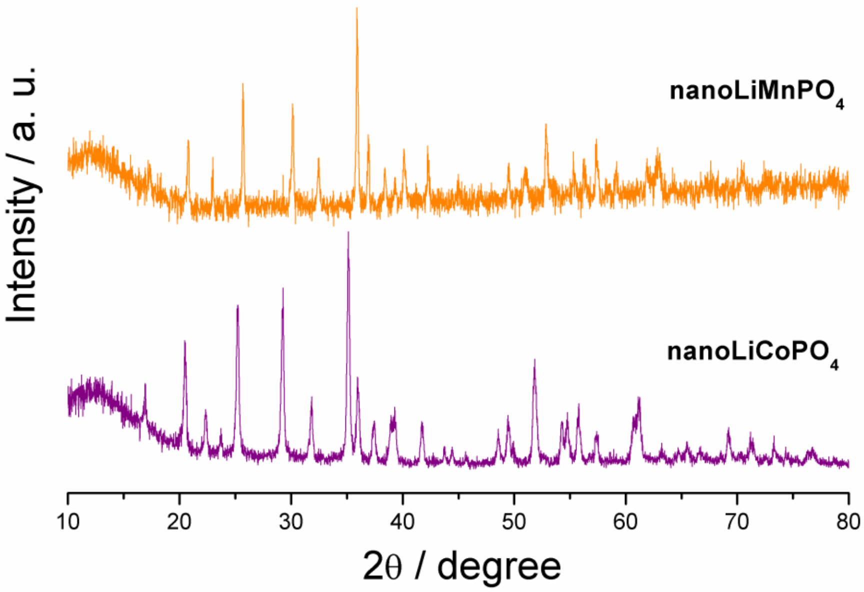

Figure 5.17 XRD patterns of pristine nanostructured $LiCoPO_4$ and $LiMnPO_4$ synthesized solvothermally at 200 °C.

5.7 Summary

In summary a novel, simple and scalable solvothermal synthesis approach has been shown to be an effective way to attain single crystalline and nanostructured, pristine $LiFePO_4$ (sheets smaller than 200 nm). Subsequently, introducing different carbohydrates (glucose, chitosan) in the precursor solution allowed the synthesis of *in situ* carbon coated nanostructured $LiFePO_4$ *via* the solvothermal carbonization reaction. It has been observed that the presence of carbohydrates plays a critical role on the morphology of the final $LiFePO_4$ material acting as an encapsulating agent and in some cases (using chitosan) enables the synthesis of highly uniform, crystalline and pure nano-rod type core-shell structures. Also, for the first time, the idea of introducing nitrogen species in the $LiFePO_4$ carbon coating for enhanced electron transport and conductivity has been successfully employed.

Electrochemical study of the selected synthesized materials revealed that they offer relatively low polarization values suggesting good kinetics, high capacity and excellent cycling capabilities. Even in the case of pristine nanostructured $LiFePO_4$ specific capacity is as high as ≈120 mA h g^{-1} at 0.1 *C* which is a significant improvement in comparison to very low ≈25 mA h g^{-1} at 0.1 *C* of the pristine $LiFePO_4$ mesocrystals. Furthermore, it is found that the existence of nitrogen in the carbon coating of nanostructured $LiFePO_4$ lowers the polarization values under 0.001 V, with almost perfect voltage-composition curves of such material. The capacity of n-doped carbon/$LiFePO_4$ composite synthesized using chitosan exhibited capacity ≈160 mA h g^{-1} at 0.1 *C* which is approximately 94% of the theoretical capacity for this type of material due to its highly uniform rod-like core-shell morphology, good carbon coverage and possible influence of 2wt% of nitrogen incorporated in the nanoparticulate shell.

Finally, easy solvothermal route presented in this chapter has been extended for synthesis of nanostructured $LiCoPO_4$ and $LiMnPO_4$ with high purity and crystallinity at temperatures as low as 200 ^{o}C.

6 Conclusions and outlook

In this thesis, novel morphologies of $LiFePO_4$ as possible cathode materials for lithium-ion batteries have been synthesized, characterized, and tested. The materials were synthesized using solvothermal methods. The reactions are single-step processes and are taking place in an autoclave at significantly lower temperature (200 ^oC) compared to the conventional solid-state method (multiple-step and up to 800 ^oC). The synthesis method used in this work could easily be scaled-up providing a feasible and cost-effective substitution for the high-energy solid-state technique. The use of inexpensive environmentally benign precursors offers a green manufacturing approach for a large scale production. Moreover, ethanol is used as a reaction medium to control crystal growth, allowing formation of mesocrystals and nanostructures. As carbon coating is the most efficient way to improve electronic conductivity of $LiFePO_4$, an additional carbon layer was also applied. Carbon-coated $LiFePO_4$ materials are obtained by adding a carbohydrate in the precursor solution. The carbohydrate transforms to carbon *via* solvothermal carbonization. This reaction is simultaneous to inorganic formation of $LiFePO_4$, forming carbon coating *in situ* and allowing intimate contact between the inorganic and the organic phase. In this work, nitrogen-doped carbon coating of $LiFePO_4$ was proposed for the first time.

The mesocrystals synthesized in this work exhibited uniformity, high crystallinity and beautiful urchin-like morphology. The morphology has been shown to consist of monodispersed spheres (25 to 40 µm; Figures 4.2 to 4.4) formed by micrometer sized self-assembled primary particles. It has been proven that this unusual and previously unreported morphology is directed by the presence of Cl^- anions in the precursor solution and without a need for templates. This simplification of the process is a result of employment of chloride salts ($FeCl_2 \cdot 4H_20$, LiCl) as reagents. The mesocystalline primary particles are both plate-like and single crystalline. These plate-like structures are beneficial because they could facilitate Li^+ ion migration as a result of the shortened diffusion distance and also simultaneously increase exchangeable Li^+ ion amount due to better accessible active surfaces of the particles. In addition, N-acetylglucosamine has been found to be a suitable carbonizing agent for the coating of a nitrogen-containing amorphous carbon layer.

The formation mechanism of mesocrystals is not yet fully understood. It is speculated that urchin-like spherical mesocrystals form *via* solvothermal Ostwald ripening from amorphous dumbbell-like particles.

The nanostructured $LiFePO_4$ synthesized in this thesis were obtained using a similar procedure to the one used for mesocrystals, however with Fe(II) acetylacetonate as the source of iron. It has been proven that the presence of carbohydrates in the precursor solution plays a critical role on the morphology of the final nanostructured $LiFePO_4$ material, acting as an encapsulating agent. A pristine nanostructured $LiFePO_4$ takes a sheet-like morphology while the glucose originating carbon coated $LiFePO_4$ consists of aggregated flake-like sheets and nanoparticles. By using chitosan as a carbon source, highly uniform nano-rod type core-shell structures of $LiFePO_4$ were obtained (100 nm long, 10 nm wide; Figure 5.7).

Suitable materials were selected and further treated under inert atmosphere at 700 ^oC for conductivity enhancement, followed by electrochemical testing to validate potential of the materials to be used as cathodes in lithium-ion batteries. The results showed that the carbon-coated $LiFePO_4$ mesocrystals delivered a stable specific capacity of ≈100 mA h g^{-1} at current density of 0.1 *C* (59% of theoretical capacity) in comparison to a very low value of ≈25 mA h g^{-1} at current density of 0.1 *C* for pristine $LiFePO_4$ (15% of theoretical capacity) which confirms the importance of *in situ* carbon coating (Figure 4.17). The theoretical capacity and perfect cycling behavior of $LiFePO_4$/carbon mescrystals could not be reached due to imperfections such as inhomogeneous carbon coating (seen with HR-TEM; Figure 4.6), existence of Fe^{3+} as a substitute to preferable Fe^{2+} on the surface of the $LiFePO_4$ primary particles and chloride impurities in the bulk. The electrochemical testing of nanostructured $LiFePO_4$ materials showed good kinetics, high capacities and excellent cycling stabilities. Even in the case of pristine $LiFePO_4$ the capacity was ≈120 mA h g^{-1} at current density of 0.1 *C* (71% of theoretical capacity) due to enhanced Li^+ ion and electron transport in smaller particles. The capacities of carbon coated LiFePO4 (glucose originating) and nitrogen-containing carbon coated LiFePO4 (chitosan originating) are ≈150 mA h g^{-1} (88% of theoretical capacity) and 160 (94% of theoretical capacity), respectively (Figure 5.14).

Numerous studies to further explore materials synthesized and processes used in this thesis remain out of scope of this work. For example, organized $LiFePO_4$ mesocrystal growth experiments with and without carbohydrate present in the precursor solution can be conducted in order to fully understand the formation mechanism. For nanostructured $LiFePO_4$, different non-nitrogen containing and nitrogen-containing carbohydrate can be employed to evaluate their effect on the morphology of carbon-coated $LiFePO_4$ with a possibility of synthesis of uniform, very small nanoparticles with theoretical specific capacity.

In conclusion, this thesis presents a major progress in the development of $LiFePO_4$ as a cathode material for lithium-ion batteries. Using simple procedures, a completely novel morphology has been synthesized (mesocrystals; Chapter 4) and excellent electrochemical behavior was recorded (nanostructures; Chapter 5). These newly developed experimental procedures for both mesocrystals and nanostructures of $LiFePO_4$ can be extended to other phospho-olivine materials, such as $LiCoPO_4$ and $LiMnPO_4$. Also, the results of this thesis indicate that solvothermal synthesis combined with solvothermal carbonization could be a feasible production method for other *in situ* carbon coated inorganic materials suitable for energy applications (such as $LiMn_2O_4$, $Li_4Ti_{15}O_{12}$, $Li_3V_2(PO_4)_3$, MnO_2, SnO_2, TiO_2, Fe_3O_2). The carbon coated rod-like nanoparticles of $LiFePO_4$ showed an excellent prospect to be used as a potential improved cathode in lithium-ion batteries due to an enhanced carbon coverage and possible influence of 2 wt % of nitrogen incorporated in their shell.

Acknowledgements

It is a pleasure to thank the many people who made this thesis possible.

Firstly, I would like to thank my principal supervisor Prof. Markus Antonietti for giving me the opportunity to work at MPI-KG, for granting me the freedom to develop my own scientific ideas and for being a primary source of energy in exciting environment of the Institute.

Immense thank you goes to my group leader Dr. Maria-Magdalena Titirici, for her support, advices and patience on both scientific and personal level from the first day of my PhD work until the very end.

I would like to acknowledge Dr. Rezan Demir-Cakan for performing irreplaceable electrochemical tests of my materials and for inviting me to the Amiens lab, so that I was able to learn first-hand about battery materials. Dr. Julian Tornow and Dr. Marta Sevilla are also acknowledged for performing valuable measurements on my materials.

I am most grateful to Dr. David Portehault for teaching me everything I know about powder diffraction, for his support, continuous scientific discussions and kind friendship.

Dr. Zoran Nikoloski is thanked for his friendship, scientific advices and for re-reading my thesis.

A special thanks goes to my fellow colleagues, office-mates, lunch-mates and coffee corner-mates and all friends from the Institute for a pleasant working atmosphere. Golm was a good place to be.

I wish to thank my extended “Berlin family” for making me feel at home, especially Dejan Bućin for bringing art into my life and for his affectionate friendship.

Lastly, but most importantly, I would like to thank my mother Vesna, father Milan and sister Aleksandra. They supported me, taught me and loved me. To them I dedicate this thesis.

Publications and presentations list

Publications

J. Popovic, R. Demir-Cakan, J. Tornow, M. Morcrette, D. Sheng-Su, R. Schlögl, M Antonietti and M.-M. Titirici.

“$LiFePO_4$ Mesocrystals for Lithium-Ion Batteries”, Small, 7, 8, 1127-1135, 2011

Presentations

“Biomass derived sustainable carbon materials for CO_2 sequestration and energy storage” (poster presentation)

Carbons for Energy Storage and Environment Protection (CESEP) 2009, Torremolinos, Spain

“Solvothermal synthesis of $LiFePO_4$ coated with nitrogen-doped carbon for lithium-ion batteries” (oral presentation)

The Annual World Conference on Carbon 2010, Clemson, SC, USA

“Solvothermal synthesis of highly hierarchical urchin-like $LiFePO_4$ mesocrystals and $LiFePO_4$/C composites” (poster presentation)

Materials Research Society (MRS) Fall meeting 2010, Boston, MA, USA

“Novel urchin-like mesocrystals of $LiFePO_4$ coated with nitrogen-doped carbon for Li-ion batteries” (oral presentation)

Materials Research Society (MRS) Fall meeting 2010, Boston, MA, USA

References

[1] Cheng, F.; Liang, J.; Tao, Z.; Chen, J., Functional materials for rechargeable batteries. *Advanced Materials* **2011,** 23, (15), 1695-1715.

[2] Whittingham, M. S., Materials challenges facing electrical energy storage. *MRS Bulletin* **2008,** 33, 411-419.

[3] Goodenough, J. B.; Kim, Y., Challenges for rechargeable Li batteries. *Chemistry of Materials* **2009,** 22, (3), 587-603.

[4] Tarascon, J. M.; Armand, M., Issues and challenges facing rechargeable lithium batteries. *Nature* **2001,** 414, (6861), 359-367.

[5] Nagaura, T. T., K., Lithium ion recheargable battery. *Progress in Batteries & Solar Cells* **1990,** 9, 209.

[6] Scrosati, B.; Garche, J., Lithium batteries: Status, prospects and future. *Journal of Power Sources* **2010,** 195, (9), 2419-2430.

[7] Wakihara, M., Yamamoto, O., *Lithium ion batteries: fundamentals and performance*. Wiley-VCH Verlag Gmbh, Kodansha Ltd.: 1998.

[8] Van Schalkwijk, W., Scrosati, B., *Advances in Lithium-ion batteries*. Kluwer Academic, Plenum: New York, 2002.

[9] Ozawa, K., *Lithium ion recheargable batteries*. Wiley-VCH Verlag GmbH & Co., Weinheim: 2009.

[10] Whittingham, M. S., Lithium Batteries and Cathode Materials. *Chemical Reviews* **2004,** 104, (10), 4271-4302.

[11] Bruce, P. G.; Scrosati, B.; Tarascon, J.-M., Nanomaterials for Rechargeable Lithium Batteries. *Angewandte Chemie International Edition* **2008,** 47, (16), 2930-2946.

[12] Goodenough, J. B.; Kim, Y., Challenges for Rechargeable Li Batteries *Chemistry of Materials* **2009,** 22, (3), 587-603.

[13] Kaskhedikar, N. A.; Maier, J., Lithium storage in carbon nanostructures. *Advanced Materials* **2009,** 21, (25-26), 2664-2680.

[14] Cabana, J.; Monconduit, L.; Larcher, D.; Palacin, M. R., Beyond intercalation-based Li-ion batteries: The state of the art and challenges of electrode materials reacting through conversion reactions. *Advanced Materials* **2010,** 22, (35), E170-E192.

[15] Poizot, P.; Laruelle, S.; Grugeon, S.; Dupont, L.; Tarascon, J. M., Nano-sized transition-metaloxides as negative-electrode materials for lithium-ion batteries. *Nature* **2000,** 407, (6803), 496-499.

[16] Park, J. C.; Kim, J.; Kwon, H.; Song, H., Gram-Scale Synthesis of Cu2O Nanocubes and Subsequent Oxidation to CuO Hollow Nanostructures for Lithium-Ion Battery Anode Materials. *Advanced Materials* **2009,** 21, (7), 803-+.

[17] Ban, C. M.; Wu, Z. C.; Gillaspie, D. T.; Chen, L.; Yan, Y. F.; Blackburn, J. L.; Dillon, A. C., Nanostructured Fe_3O_4/SWNT electrode: Binder-free and high-rate Li-ion anode. *Advanced Materials* **2010,** 22, (20), E145-+.

[18] Doh, C. H.; Kalaiselvi, N.; Park, C. W.; Jin, B. S.; Moon, S. I.; Yun, M. S., Synthesis and electrochemical characterization of novel high capacity $Si_{3-x}Fe_xN_4$ anode for rechargeable lithium batteries. *Electrochemistry Communications* **2004,** 6, (10), 965-968.

[19] Cabana, J.; Stoeva, Z.; Titman, J. J.; Gregory, D. H.; Palacin, M. R., Towards new negative electrode materials for Li-ion batteries: Electrochemical properties of LiNiN. *Chemistry of Materials* **2008,** 20, (5), 1676-1678.

[20] Ducrosa, J. B.; Bach, S.; Pereira-Ramos, J. P.; Willmann, P., Layered lithium cobalt nitrides: A new class of lithium intercalation compounds. *Journal of Power Sources* **2008,** 175, (1), 517-525.

[21] Bach, S.; Pereira-Ramos, J. R.; Ducros, J. B.; Willmann, R., Structural and electrochemical properties of layered lithium nitridocuprates $Li_{3-x}Cu_xN$. *Solid State Ionics* **2009,** 180, (2-3), 231-235.

[22] Li, H.; Wang, Z.; Chen, L.; Huang, X., Research on advanced materials for Li-ion batteries. *Advanced Materials* **2009,** 21, (45), 4593-4607.

[23] Kim, H.; Seo, M.; Park, M. H.; Cho, J., A critical size of silicon nano-anodes for lithium rechargeable batteries. *Angewandte Chemie-International Edition* **2010,** 49, (12), 2146-2149.

[24] Lou, X. W.; Li, C. M.; Archer, L. A., Designed synthesis of coaxial SnO_2@carbon hollow nanospheres for highly reversible lithium storage. *Advanced Materials* **2009,** 21, (24), 2536-+.

[25] Martin, C.; Alias, M.; Christien, F.; Crosnier, O.; Belanger, D.; Brousse, T., Graphite-grafted silicon nanocomposite as a negative electrode for Lithium-ion batteries. *Advanced Materials* **2009,** 21, (46), 4735-+.

[26] Chan, C. K.; Patel, R. N.; O'Connell, M. J.; Korgel, B. A.; Cui, Y., Solution-grown silicon nanowires for Lithium-ion battery anodes. *Acs Nano* **2010,** 4, (3), 1443-1450.

[27] Magasinski, A.; Dixon, P.; Hertzberg, B.; Kvit, A.; Ayala, J.; Yushin, G., High-performance lithium-ion anodes using a hierarchical bottom-up approach. *Nature Materials* **2010,** 9, (4), 353-358.

[28] Demir-Cakan, R.; Hu, Y. S.; Antonietti, M.; Maier, J.; Titirici, M. M., Facile one-pot synthesis of mesoporous SnO_2 microspheres via nanoparticles assembly and lithium storage properties. *Chemistry of Materials* **2008,** 20, (4), 1227-1229.

[29] Hu, Y.-S.; Demir-Cakan, R.; Titirici, M.-M.; Müller, J.-O.; Schlögl, R.; Antonietti, M.; Maier, J., Superior storage performance of a Si@SiO_x/C nanocomposite as anode material for Lithium-ion batteries. *Angewandte Chemie International Edition* **2008,** 47, (9), 1645-1649.

[30] Venkatraman, S.; Shin, Y.; Manthiram, A., Phase relationships and structural and chemical stabilities of charged $Li_{1-x}CoO_{2-delta}$ and $Li_{1-x}Ni_{0.85}Co_{0.15}O_{2-delta}$ cathodes. *Electrochemical and Solid-State Letters* **2003,** 6, (1), A9-A12.

[31] Dahn, J. R.; Fuller, E. W.; Obrovac, M.; Vonsacken, U., Thermal- stability of Li_xCoO_2, Li_xNiO_2 and lambda-MnO_2 and consequences for the safety of Li-ion cells. *Solid State Ionics* **1994,** 69, (3-4), 265-270.

[32] Dahn, J. R.; Vonsacken, U.; Juzkow, M. W.; Aljanaby, H., Recheargable $LiNiO_2$ carbon cells *Journal of the Electrochemical Society* **1991,** 138, (8), 2207-2211.

[33] Armstrong, A. R.; Bruce, P. G., Synthesis of layered $LiMnO_2$ as an electrode for rechargeable lithium batteries. *Nature* **1996,** 381, (6582), 499-500.

[34] Padhi, A. K.; Nanjundaswamy, K. S.; Goodenough, J. B., Phospho-olivines as positive-electrode materials for rechargeable lithium batteries. *Journal of The Electrochemical Society* **1997,** 144, (4), 1188-1194.

[35] Padhi, A. K.; Nanjundaswamy, K. S.; Masquelier, C.; Okada, S.; Goodenough, J. B., Effect of structure on the Fe^{3+}/Fe^{2+} redox couple in iron phosphates. *Journal of the Electrochemical Society* **1997,** 144, (5), 1609-1613.

[36] Andersson, A. S.; Kalska, B.; Haggstrom, L.; Thomas, J. O., Lithium extraction/insertion in $LiFePO_4$: an X-ray diffraction and Mossbauer spectroscopy study. *Solid State Ionics* **2000,** 130, (1-2), 41-52.

[37] Martin, J. F.; Yamada, A.; Kobayashi, G.; Nishimura, S. I.; Kanno, R.; Guyomard, D.; Dupre, N., Air exposure effect on $LiFePO_4$. *Electrochemical and Solid State Letters* **2008,** 11, (1), A12-A16.

[38] Cuisinier, M.; Martin, J. F.; Dupre, N.; Yamada, A.; Kanno, R.; Guyomard, D., Moisture driven aging mechanism of $LiFePO_4$ subjected to air exposure. *Electrochemistry Communications* **2010,** 12, (2), 238-241.

[39] Takahashi, M.; Tobishima, S.; Takei, K.; Sakurai, Y., Characterization of $LiFePO_4$ as the cathode material for rechargeable lithium batteries. *Journal of Power Sources* **2001,** 97-8, 508-511.

[40] Morgan, D.; Van der Ven, A.; Ceder, G., Li conductivity in Li_xMPO_4 (M = Mn, Fe, Co, Ni) olivine materials. *Electrochemical and Solid State Letters* **2004,** 7, (2), A30-A32.

[41] Islam, M. S.; Driscoll, D. J.; Fisher, C. A. J.; Slater, P. R., Atomic-scale investigation of defects, dopants, and lithium transport in the $LiFePO_4$ olivine-type battery material. *Chemistry of Materials* **2005,** 17, (20), 5085-5092.

[42] Chung, S. Y.; Bloking, J. T.; Chiang, Y. M., Electronically conductive phospho-olivines as lithium storage electrodes. *Nature Materials* **2002,** 1, (2), 123-128.

[43] Yamada, A.; Chung, S. C.; Hinokuma, K., Optimized $LiFePO_4$ for lithium battery cathodes. *Journal of the Electrochemical Society* **2001,** 148, (3), A224-A229.

[44] Muraliganth, T.; Murugan, A. V.; Manthiram, A., Nanoscale networking of LiFePO4 nanorods synthesized by a microwave-solvothermal route with carbon nanotubes for lithium ion batteries. *Journal of Materials Chemistry* **2008,** 18, (46), 5661-5668.

[45] Wang, Y. G.; Wang, Y. R.; Hosono, E. J.; Wang, K. X.; Zhou, H. S., The design of a LiFePO4/carbon nanocomposite with a core-shell structure and its synthesis by an in situ polymerization restriction method. *Angewandte Chemie-International Edition* **2008,** 47, (39), 7461-7465.

[46] Ravet, N. G., J. B.; Besner, S.; Simoneau, M.; Hovington P. and Armand M., In *The Electrochemical Society and The Electrochemical Society of Japan Meeting Abstracts*, Honolulu, HI, 1999.

[47] Park, K. S.; Schougaard, S. B.; Goodenough, J. B., Conducting-Polymer/Iron-Redox-Couple Composite Cathodes for Lithium Secondary Batteries. *Advanced Materials* **2007,** 19, (6), 848-851.

[48] Hu, Y. S.; Guo, Y. G.; Dominko, R.; Gaberscek, M.; Jamnik, J.; Maier, J., Improved electrode performance of porous $LiFePO_4$ using RuO_2 as an oxidic nanoscale interconnect. *Advanced Materials* **2007,** 19, (15), 1963-+.

[49] Huang, H.; Yin, S. C.; Nazar, L. F., Approaching theoretical capacity of $LiFePO_4$ at room temperature at high rates. *Electrochemical and Solid State Letters* **2001,** 4, (10), A170-A172.

[50] Dominko, R.; Bele, M.; Gaberscek, M.; Remskar, M.; Hanzel, D.; Pejovnik, S.; Jamnik, J., Impact of the carbon coating thickness on the electrochemical performance of $LiFePO_4$/C composites. *Journal of The Electrochemical Society* **2005,** 152, (3), A607-A610.

[51] Bilecka, I.; Hintennach, A.; Rossell, M. D.; Xie, D.; Novak, P.; Niederberger, M., Microwave-assisted solution synthesis of doped $LiFePO_4$ with high specific charge and outstanding cycling performance. *Journal of Materials Chemistry* **2011,** 21, (16), 5881-5890.

[52] Yu, F.; Zhang, J.-J.; Yang, Y.-F.; Song, G.-Z., Up-scalable synthesis, structure and charge storage properties of porous microspheres of $LiFePO_4$@C nanocomposites. *Journal of Materials Chemistry* **2009,** 19, (48), 9121-9125.

[53] Zhou, Y.; Wang, J.; Hu, Y.; O'Hayre, R.; Shao, Z., A porous $LiFePO_4$ and carbon nanotube composite. *Chemical Communications* **2010,** 46, (38), 7151-7153.

[54] Liu, J.; Conry, T. E.; Song, X.; Doeff, M. M.; Richardson, T. J., Nanoporous spherical $LiFePO_4$ for high performance cathodes. *Energy & Environmental Science* **2011,** 4, (3), 885-888.

[55] Saravanan, K.; Balaya, P.; Reddy, M. V.; Chowdari, B. V. R.; Vittal, J. J., Morphology controlled synthesis of $LiFePO_4$/C nanoplates for Li-ion batteries. *Energy & Environmental Science* **2010,** 3, (4), 457-464.

[56] Srinivasan, V.; Newman, J., Discharge model for the lithium iron-phosphate electrode. *Journal of the Electrochemical Society* **2004,** 151, (10), A1517-A1529.

[57] Laffont, L.; Delacourt, C.; Gibot, P.; Wu, M. Y.; Kooyman, P.; Masquelier, C.; Tarascon, J. M., Study of the $LiFePO_4$/$FePO_4$ two-phase system by high-resolution electron energy loss spectroscopy. *Chemistry of Materials* **2006,** 18, (23), 5520-5529.

[58] Delmas, C.; Maccario, M.; Croguennec, L.; Le Cras, F.; Weill, F., Lithium deintercalation in $LiFePO_4$ nanoparticles via a domino-cascade model. *Nat Mater* **2008,** 7, (8), 665-671.

[59] Ramana, C. V.; Mauger, A.; Gendron, F.; Julien, C. M.; Zaghib, K., Study of the Li-insertion/extraction process in $LiFePO_4$/$FePO_4$. *Journal of Power Sources* **2009,** 187, (2), 555-564.

[60] Yuan, L. X.; Wang, Z. H.; Zhang, W. X.; Hu, X. L.; Chen, J. T.; Huang, Y. H.; Goodenough, J. B., Development and challenges of $LiFePO_4$ cathode material for lithium-ion batteries. *Energy & Environmental Science* **2011,** 4, (2), 269-284.

[61] Liu, S. Q.; Gong, B. L.; Huang, K. L.; Zhang, G.; Li, S. C., Synthesis of $LiFePO_4$/C composite cathode materials by a novel carbothermal reduction method and its performance. *Journal of Inorganic Materials* **2007,** 22, (2), 283-286.

[62] Murugan, A. V.; Muraliganth, T.; Manthiram, A., Comparison of microwave assisted solvothermal and hydrothermal syntheses of $LiFePO_4$/C nanocomposite cathodes for lithium ion batteries. *Journal of Physical Chemistry C* **2008,** 112, (37), 14665-14671.

[63] Murugan, A. V.; Muraliganth, T.; Manthiram, A., One-pot microwave-hydrothermal synthesis and characterization of carbon-coated $LiMPO_4$ (M=Mn, Fe, and Co) cathodes. *Journal of the Electrochemical Society* **2009,** 156, (2), A79-A83.

[64] Wang, S. P.; Zhou, C. G.; Zhou, Q. A.; Ni, G.; Wu, J. P., Preparation of $LiFePO_4$/C in a reductive atmosphere generated by windward aerobic decomposition of glucose. *Journal of Power Sources* **2011,** 196, (11), 5143-5146.

[65] Spong, A. D.; Vitins, G.; Owen, J. R., A solution-precursor synthesis of carbon-coated $LiFePO_4$ for Li-ion cells. *Journal of the Electrochemical Society* **2005,** 152, (12), A2376-A2382.

[66] Roberts, M. R.; Spong, A. D.; Vitins, G.; Owen, J. R., High throughput screening of the effect of carbon coating in $LiFePO_4$ electrodes. *Journal of the Electrochemical Society* **2007,** 154, (10), A921-A928.

[67] Zhang, D.; Yu, X.; Wang, Y. F.; Cai, R.; Shao, Z. P.; Liao, X. Z.; Ma, Z. F., Ballmilling-assisted synthesis and electrochemical performance of $LiFePO_4$/C for lithium-ion battery adopting citric acid as carbon precursor. *Journal of the Electrochemical Society* **2009,** 156, (10), A802-A808.

[68] Ravet, N.; Gauthier, M.; Zaghib, K.; Goodenough, J. B.; Mauger, A.; Gendron, F.; Julien, C. M., Mechanism of the Fe^{3+} reduction at low temperature for $LiFePO_4$ synthesis from a polymeric additive. *Chemistry of Materials* **2007,** 19, (10), 2595-2602.

[69] Dominko, R.; Bele, M.; Goupil, J. M.; Gaberscek, M.; Hanzel, D.; Arcon, I.; Jamnik, J., Wired porous cathode materials: A novel concept for synthesis of $LiFePO_4$. *Chemistry of Materials* **2007,** 19, (12), 2960-2969.

[70] Rho, Y. H.; Nazar, L. F.; Perry, L.; Ryan, D., Surface chemistry of $LiFePO_4$ studied by mossbauer and X-ray photoelectron spectroscopy and its effect on electrochemical properties. *Journal of the Electrochemical Society* **2007,** 154, (4), A283-A289.

[71] Doeff, M. M.; Hu, Y. Q.; McLarnon, F.; Kostecki, R., Effect of surface carbon structure on the electrochemical performance of $LiFePO_4$. *Electrochemical and Solid State Letters* **2003,** 6, (10), A207-A209.

[72] Zaghib, K.; Mauger, A.; Gendron, F.; Julien, C. M., Surface effects on the physical and electrochemical properties of thin $LiFePO_4$ particles. *Chemistry of Materials* **2008,** 20, (2), 462-469.

[73] Wang, X.; Li, X.; Zhang, L.; Yoon, Y.; Weber, P. K.; Wang, H.; Guo, J.; Dai, H., N-doping of graphene through electrothermal reactions with ammonia. *Science* **2009,** 324, (5928), 768-771.

[74] Wei, D.; Liu, Y.; Wang, Y.; Zhang, H.; Huang, L.; Yu, G., Synthesis of N-doped graphene by chemical vapor deposition and its electrical properties. *Nano Letters* **2009,** 9, (5), 1752-1758.

[75] Reddy, A. L. M.; Srivastava, A.; Gowda, S. R.; Gullapalli, H.; Dubey, M.; Ajayan, P. M., Synthesis of nitrogen-doped graphene films for lithium battery application. *ACS Nano* **2010,** 4, (11), 6337-6342.

[76] Zhao, L.; Baccile, N.; Gross, S.; Zhang, Y.; Wei, W.; Sun, Y.; Antonietti, M.; Titirici, M.-M., Sustainable nitrogen-doped carbonaceous materials from biomass derivatives. *Carbon* **2010,** 48, (13), 3778-3787.

[77] Jugovic, D.; Uskokovic, D., A review of recent developments in the synthesis procedures of lithium iron phosphate powders. *Journal of Power Sources* **2009,** 190, (2), 538-544.

[78] Yang, S. F.; Song, Y. N.; Ngala, K.; Zavalij, P. Y.; Whittingham, M. S., Performance of $LiFePO_4$ as lithium battery cathode and comparison with manganese and vanadium oxides. *Journal of Power Sources* **2003,** 119, 239-246.

[79] Koltypin, M.; Aurbach, D.; Nazar, L.; Ellis, B., More on the performance of $LiFePO_4$ electrodes - The effect of synthesis route, solution composition, aging, and temperature. *Journal of Power Sources* **2007,** 174, (2), 1241-1250.

[80] Herle, P. S.; Ellis, B.; Coombs, N.; Nazar, L. F., Nano-network electronic conduction in iron and nickel olivine phosphates. *Nature Materials* **2004,** 3, (3), 147-152.

[81] Chiang, Y. M., Gozdz, A.S., Payne, M.W. Nanoscale ion storage materials. US 2007/0190418, 2008.

[82] Saidi, M. M., Huang, H. Synthesis of metal phosphates. US 7060238 B2, 2006.

[83] Yamada, A.; Hosoya, M.; Chung, S. C.; Kudo, Y.; Hinokuma, K.; Liu, K. Y.; Nishi, Y., Olivine-type cathodes achievements and problems. *Journal of Power Sources* **2003,** 119, 232-238.

[84] Byrappa, K., Yoshimura, M., *Handbook of hydrothermal technology: A technology for crystal growth and materials processing*. Noyes Publications, New Jersey, USA / William Andrew Publishing, New York, USA: 2001.

[85] Demir-Cakan, R. Synthesis, characterization and applications of nanostructured materials using hydrothermal carbonization. University of Potsdam, Potsdam, 2009.

[86] Yang, S. F.; Zavalij, P. Y.; Whittingham, M. S., Hydrothermal synthesis of lithium iron phosphate cathodes. *Electrochemistry Communications* **2001,** 3, (9), 505-508.

[87] Dokko, K.; Koizumi, S.; Nakano, H.; Kanamura, K., Particle morphology, crystal orientation, and electrochemical reactivity of $LiFePO_4$ synthesized by the hydrothermal method at 443 K. *Journal of Materials Chemistry* **2007,** 17, (45), 4803-4810.
[88] Ellis, B.; Kan, W. H.; Makahnouk, W. R. M.; Nazar, L. F., Synthesis of nanocrystals and morphology control of hydrothermally prepared $LiFePO_4$. *Journal of Materials Chemistry* **2007,** 17, (30), 3248-3254.
[89] Zhu, S. M.; Zhou, H. S.; Miyoshi, T.; Hibino, M.; Honma, I.; Ichihara, M., Self-assembly of the mesoporous electrode material $Li_3Fe_2(PO4)_3$ using a cationic surfactant as the template. *Advanced Materials* **2004,** 16, (22), 2012-+.
[90] Dong-Han, K.; Jaekook, K., Synthesis of $LiFePO_4$ nanoparticles in polyol medium and their electrochemical properties. *Electrochemical and Solid-State Letters* **2006,** 9, (9), A439-A442.
[91] Vadivel Murugan, A.; Muraliganth, T.; Manthiram, A., Rapid microwave-solvothermal synthesis of phospho-olivine nanorods and their coating with a mixed conducting polymer for lithium ion batteries. *Electrochemistry Communications* **2008,** 10, (6), 903-906.
[92] Saravanan, K.; Reddy, M. V.; Balaya, P.; Gong, H.; Chowdari, B. V. R.; Vittal, J. J., Storage performance of $LiFePO_4$ nanoplates. *Journal of Materials Chemistry* **2009,** 19, (5), 605-610.
[93] Yang, S.; Zhou, X.; Zhang, J.; Liu, Z., Morphology-controlled solvothermal synthesis of $LiFePO_4$ as a cathode material for lithium-ion batteries. *Journal of Materials Chemistry* **2010,** 20, (37), 8086-8091.
[94] Tarascon, J. M.; Recham, N.; Armand, M.; Chotard, J. N.; Barpanda, P.; Walker, W.; Dupont, L., Hunting for better Li-based electrode materials via low temperature inorganic synthesis. *Chemistry of Materials* **2010,** 22, (3), 724-739.
[95] Hsu, K.-F.; Tsay, S.-Y.; Hwang, B.-J., Synthesis and characterization of nano-sized $LiFePO_4$ cathode materials prepared by a citric acid-based sol-gel route. *Journal of Materials Chemistry* **2004,** 14, (17), 2690-2695.
[96] Lee, Y. J.; Belcher, A. M., Nanostructure design of amorphous $FePO_4$ facilitated by a virus for 3 V lithium ion battery cathodes. *Journal of Materials Chemistry* **2010,** 21, (4), 1033-1039.
[97] Lee, Y. J.; Yi, H.; Kim, W.-J.; Kang, K.; Yun, D. S.; Strano, M. S.; Ceder, G.; Belcher, A. M., Fabricating genetically engineered high-power Lithium-ion batteries using multiple virus genes. *Science* **2009,** 324, (5930), 1051-1055.
[98] Pecharsky, V. K., Zavalij, P.Y., *Fundamentals of powder diffraction and structural characterization of materials*. Springer: Boston, MA, 2005.
[99] Bragg, W. H., X-rays and crystals. *Nature* **1912,** 90, (360).
[100] Ewald, P. P., Zur Begründung der Kristalloptik. *Annalen der Physik* **1917,** 54, 519.
[101] Dinnebier, R. E.; Billinge, S. J. L., *Powder diffraction: Theory and practice*. RCS Publishing: Cambridge, UK, 2008.
[102] Le Bail, A.; Duroy, H.; Fourquet, J. L., Ab-initio structure determination of $LiSbWO_6$ by X-ray powder diffraction. *Materials Research Bulletin* **1988,** 23, (3), 447-452.
[103] Amelinckx, S.; van Dyck, D.; van Landuyt, J.; van Tendeloo, G., *Electron microscopy: Principles and fundamentals*. VCH Verlagsgesellschaft GmbH: Weinheim, 1997.
[104] Shindo, D.; Hiraga, K., *High-resolution electron microscopy for materials science*. Springer Verlag: Tokyo, 1998.
[105] Kirkland, A. I., Hutchinson, J.L., *Nanocharacterization*. RSC Publishing: Cambridge, UK, 2007.

[106] Wakihara, M.; Yamamoto, O., *Lithium ion batteries: Fundamentals and performance*. Wiley-VCH: Tokyo, 1998.

[107] Muñoz-Rojas, D.; Leriche, J.-B.; Delacourt, C.; Poizot, P.; Palacín, M. R.; Tarascon, J.-M., Development and implementation of a high temperature electrochemical cell for lithium batteries. *Electrochemistry Communications* **2007,** 9, (4), 708-712.

[108] Dreyer, W.; Jamnik, J.; Guhlke, C.; Huth, R.; Moskon, J.; Gaberscek, M., The thermodynamic origin of hysteresis in insertion batteries. *Nature Materials* **2010,** 9, (5), 448-453.

[109] Colfen, H.; Mann, S., Higher-order organization by mesoscale self-assembly and transformation of hybrid nanostructures. *Angewandte Chemie-International Edition* **2003,** 42, (21), 2350-2365.

[110] Colfen, H.; Antonietti, M., Mesocrystals: Inorganic superstructures made by highly parallel crystallization and controlled alignment. *Angewandte Chemie-International Edition* **2005,** 44, (35), 5576-5591.

[111] Yu, S. H.; Colfen, H.; Tauer, K.; Antonietti, M., Tectonic arrangement of $BaCO_3$ nanocrystals into helices induced by a racemic block copolymer. *Nature Materials* **2005,** 4, (1), 51-U5.

[112] Song, R. Q.; Colfen, H., Mesocrystals-ordered nanoparticle superstructures. *Advanced Materials* **2010,** 22, (12), 1301-1330.

[113] Addadi, L.; Weiner, S., Control and design principles in biological mineralization. *Angewandte Chemie-International Edition in English* **1992,** 31, (2), 153-169.

[114] Albeck, S.; Aizenberg, J.; Addadi, L.; Weiner, S., Interactions of various skeletal intercrystalline components with calcite crystals. *Journal of the American Chemical Society* **1993,** 115, (25), 11691-11697.

[115] Mann, S., Molecular tectonics in biomineralization and biomimetic materials. *Nature* **1993,** 365, (6446), 499-505.

[116] Zhou, L.; O'Brien, P., Mesocrystals: A new class of solid materials. *Small* **2008,** 4, (10), 1566-1574.

[117] Peng, Y.; Xu, A. W.; Deng, B.; Antonietti, M.; Colfen, H., Polymer-controlled crystallization of zinc oxide hexagonal nanorings and disks. *Journal of Physical Chemistry B* **2006,** 110, (7), 2988-2993.

[118] Yahiro, J.; Oaki, Y.; Imai, H., Biomimetic synthesis of wurtzite ZnO nanowires possessing a mosaic structure. *Small* **2006,** 2, (10), 1183-1187.

[119] Carbone, L.; Nobile, C.; De Giorgi, M.; Sala, F. D.; Morello, G.; Pompa, P.; Hytch, M.; Snoeck, E.; Fiore, A.; Franchini, I. R.; Nadasan, M.; Silvestre, A. F.; Chiodo, L.; Kudera, S.; Cingolani, R.; Krahne, R.; Manna, L., Synthesis and micrometer-scale assembly of colloidal CdSe/CdS nanorods prepared by a seeded growth approach. *Nano Letters* **2007,** 7, (10), 2942-2950.

[120] Colfen, H.; Antonietti, M., *Mesocrystals and nonclassical crystallization*. John Wiley & Sons, Ltd: 2008.

[121] Saravanan, K.; Ananthanarayanan, K.; Balaya, P., Mesoporous TiO_2 with high packing density for superior lithium storage. *Energy & Environmental Science* **2010,** 3, (7), 939-948.

[122] Xu, J. J.; Wang, K.; Zu, S. Z.; Han, B. H.; Wei, Z. X., Hierarchical nanocomposites of polyaniline nanowire arrays on graphene oxide sheets with synergistic effect for energy storage. *Acs Nano* **2010,** 4, (9), 5019-5026.

[123] Yang, H.; Wu, X. L.; Cao, M. H.; Guo, Y. G., Solvothermal synthesis of $LiFePO_4$ hierarchically dumbbell-like microstructures by nanoplate self-assembly and their

application as a cathode material in Lithium-ion batteries. *Journal of Physical Chemistry C* **2009,** 113, (8), 3345-3351.

[124] Rangappa, D.; Sone, K.; Kudo, T.; Honma, I., Directed growth of nanoarchitectured $LiFePO_4$ electrode by solvothermal synthesis and their cathode properties. *Journal of Power Sources* **2010,** 195, (18), 6167-6171.

[125] Teng, F.; Santhanagopalan, S.; Asthana, A.; Geng, X. B.; Mho, S. I.; Shahbazian-Yassar, R.; Meng, D. D., Self-assembly of $LiFePO_4$ nanodendrites in a novel system of ethylene glycol-water. *Journal of Crystal Growth* **2010,** 312, (23), 3493-3502.

[126] Popovic, J.; Demir-Cakan, R.; Tornow, J.; Morcrette, M.; Su, D. S.; Schlögl, R.; Antonietti, M.; Titirici, M.-M., $LiFePO_4$ mesocrystals for Lithium-ion batteries. *Small* **2011,** 7, (8), 1127-1135.

[127] Tan, K. S.; Reddy, M. V.; Rao, G. V. S.; Chowdari, B., High-performance $LiCoO_2$ by molten salt ($LiNO_3$: LiCl) synthesis for Li-ion batteries. *Journal of Power Sources* **2005,** 147, (1-2), 241-248.

[128] Titirici, M. M.; Thomas, A.; Yu, S. H.; Muller, J. O.; Antonietti, M., A direct synthesis of mesoporous carbons with bicontinuous pore morphology from crude plant material by hydrothermal carbonization. *Chemistry of Materials* **2007,** 19, (17), 4205-4212.

[129] Dedryvere, R.; Maccario, M.; Croguennec, L.; Le Cras, F.; Delmas, C.; Gonbeau, D., X-Ray Photoelectron Spectroscopy investigations of carbon-coated Li_xFePO_4 materials. *Chemistry of Materials* **2008,** 20, (22), 7164-7170.

[130] Tunistra, F.; Koenig, J. L., Raman spectrum of graphite. *Journal of Chemical Physics* **1970,** 53, 1126.

[131] Matijevic, E., Preparation and properties of uniform size colloids. *Chemistry of Materials* **1993,** 5, (4), 412-426.

[132] Zhang, Y. G.; Liu, Y.; Fu, S. Q.; Guo, F.; Qian, Y. T., Morphology-controlled synthesis of Co_3O_4 crystals by soft chemical method. *Materials Chemistry and Physics* **2007,** 104, (1), 166-171.

[133] Zhao, L.; Fan, L. Z.; Zhou, M. Q.; Guan, H.; Qiao, S. Y.; Antonietti, M.; Titirici, M. M., Nitrogen-Containing Hydrothermal Carbons with Superior Performance in Supercapacitors. *Advanced Materials* **2010,** 22, (45), 5202-+.

[134] Andersson, A. S.; Thomas, J. O., The source of first-cycle capacity loss in $LiFePO_4$. *Journal of Power Sources* **2001,** 97-8, 498-502.

[135] Prosini, P. P.; Zane, D.; Pasquali, M., Improved electrochemical performance of a $LiFePO_4$-based composite cathode. *Electrochimica Acta* **2001,** 46, (23), 3517-3523.

[136] Balaya, P., Size effects and nanostructured materials for energy applications. *Energy & Environmental Science* **2008,** 1, (6), 645-654.

[137] Wang, Y. G.; Li, H. Q.; He, P.; Hosono, E.; Zhou, H. S., Nano active materials for lithium-ion batteries. *Nanoscale* **2010,** 2, (8), 1294-1305.

[138] Bruce, P. G.; Scrosati, B.; Tarascon, J. M., Nanomaterials for rechargeable lithium batteries. *Angewandte Chemie-International Edition* **2008,** 47, (16), 2930-2946.

[139] Arico, A. S.; Bruce, P.; Scrosati, B.; Tarascon, J.-M.; van Schalkwijk, W., Nanostructured materials for advanced energy conversion and storage devices. *Nature Materials* **2005,** 4, (5), 366-377.

[140] Meethong, N.; Huang, H. Y. S.; Speakman, S. A.; Carter, W. C.; Chiang, Y. M., Strain accommodation during phase transformations in olivine-based cathodes as a materials selection criterion for high-power rechargeable batteries. *Advanced Functional Materials* **2007,** 17, (7), 1115-1123.

[141] Balaya, P.; Bhattacharyya, A. J.; Jamnik, J.; Zhukovskii, Y. F.; Kotomin, E. A.; Maier, J., Nano-ionics in the context of lithium batteries. *Journal of Power Sources* **2006,** 159, (1), 171-178.

[142] Maier, J., Nanoionics: ion transport and electrochemical storage in confined systems. *Nat Mater* **2005,** 4, (11), 805-815.

[143] Jiao, F.; Harrison, A.; Hill, A. H.; Bruce, P. G., Mesoporous Mn2O3 and Mn3O4 with Crystalline Walls. *Advanced Materials* **2007,** 19, (22), 4063-4066.

[144] Guo, Y.-G.; Hu, J.-S.; Wan, L.-J., Nanostructured materials for electrochemical energy conversion and storage devices. *Advanced Materials* **2008,** 20, (15), 2878-2887.

[145] Zhou, H. S.; Li, D. L.; Hibino, M.; Honma, I., A self-ordered, crystalline-glass, mesoporous nanocomposite for use as a lithium-based storage device with both high power and high energy densities. *Angewandte Chemie-International Edition* **2005,** 44, (5), 797-802.

[146] Yamada, A.; Koizumi, H.; Nishimura, S.-i.; Sonoyama, N.; Kanno, R.; Yonemura, M.; Nakamura, T.; Kobayashi, Y., Room-temperature miscibility gap in Li_xFePO_4. *Nat Mater* **2006,** 5, (5), 357-360.

[147] Kobayashi, G.; Nishimura, S. I.; Park, M. S.; Kanno, R.; Yashima, M.; Ida, T.; Yamada, A., Isolation of Solid Solution Phases in Size-Controlled LixFePO4 at Room Temperature. *Advanced Functional Materials* **2009,** 19, (3), 395-403.

[148] Kang, B.; Ceder, G., Battery materials for ultrafast charging and discharging. *Nature* **2009,** 458, (7235), 190-193.

[149] Kanamura, K.; Koizumi, S. H.; Dokko, K. R., Hydrothermal synthesis of $LiFePO_4$ as a cathode material for lithium batteries. *Journal of Materials Science* **2008,** 43, (7), 2138-2142.

[150] Mestre-Aizpurua, F.; Hamelet, S.; Masquelier, C.; Palacín, M. R., High temperature electrochemical performance of nanosized $LiFePO_4$. *Journal of Power Sources* **2010,** 195, (19), 6897-6901.

[151] Zhao, L.; Hu, Y.-S.; Li, H.; Wang, Z.; Chen, L., Porous $Li_4Ti_5O_{12}$ coated with N-doped carbon from ionic liquids for Li-ion batteries. *Advanced Materials* **2011,** 23, (11), 1385-1388.

[152] Baccile, N.; Laurent, G.; Babonneau, F.; Fayon, F.; Titirici, M.-M.; Antonietti, M., Structural Characterization of Hydrothermal Carbon Spheres by Advanced Solid-State MAS 13C NMR Investigations. *The Journal of Physical Chemistry C* **2009,** 113, (22), 9644-9654.

List of Abbreviations and Symbols

Abbreviation /Symbol	Description
α	aperture, angle of the objective lens in a microscope
a	first unit cell parameter
b	second unit cell parameter
c	third unit cell parameter
d_{hkl}	permissible interatomic distances in crystalline lattice
d^*	scattering vector
D_{Li}	Li^+ ion diffusion coefficient
EA	Elemental Analysis
EDX	Energy-Dispersive X-ray spectroscopy
EELS	Electron-Energy Loss Spectroscopy
EV	Electric Vehicle
HEV	Hybrid Electric Vehicle
HR-TEM	High-Resolution Transmission Electron Microscopy
λ	wavelength
Λ	reversible specific capacity
L	Li^+ ion diffusion lenght
L_e	electron transport lenght
η	Li^+ ion mobility in the intercalation compound
r_d	resolution of a microscope
r_{p-o}	interatomic distance between P and O atoms
s	scattered wave vector
s_0	incident wave vector
SAED	Selected-Area Electron Diffraction

SEM	Scanning Electron Microscopy
Θ	Bragg angle
τ	Li^+ ion diffusion time constant
TEM	Transmission Electron Microscopy
V_{OC}	battery cell potential
x	first atomic parameter
XPS	X-ray Photoelectron Spectroscopy
XRD	X-ray diffraction
y	second atomic parameter
Y	total intensity of a X-ray diffraction peak
z	third atomic parameter

Appendix

Instrumental details

X-ray Diffraction (XRD)

XRD patterns were recorded in reflection mode on a Bruker D8 diffractometer with $Cu_{K\alpha}$ radiation (λ_1 = 1.54053 Å), using different scanning speeds. The samples were finely grinded and measured on the silicon sample holders. Lattice parameters calculation and structure refinement of the obtained data was performed using profile matching in the Fullprof® program (Windows version, 2009).

Elemental Analysis (EA)

Carbon and nitrogen contents were determined using a Vario Elmer-Perkin elemental analyzer by Ms. Silvia Pirok (Max Planck Institute of Colloids and Interfaces, Golm, Germany).

Scanning Electron Microscopy (SEM)

SEM was performed using a Gemini Leo-1550 instrument. Before imaging, material was loaded onto carbon tapes and sputtered with Au.

Transmission Electron Microscopy (TEM)

TEM was performed using Omega 912 (Carl Zeiss, Oberkochen, Germany) instrument by Ms. Rona Pitschke and Ms. Stephanie Wohlgemuth (Max Planck Institute of Colloids and Interfaces, Golm, Germany). The samples were prepared by dispersion in ethanol and evaporative deposition onto Cu grids.

High Resolution Transmission Electron Microscopy (HR-TEM)

HR-TEM was performed using Topcon EM-002B and a Philips CM200 instrument with a LaB_6 cathode by Dr. Noriko Yoshizawa (National Institute for Material Science, Tsukuba, Japan) and Dr. Julian Tornow (Fritz Haber Institute of Max Planck Society, Berlin, Germany), respectfully. In both cases, all samples were prepared by dispersion in ethanol and evaporative deposition onto Cu grids.

Energy-Dispersive X-ray spectroscopy (EDX)

EDX was performed using a Philips CM200 spectrometer by Dr. Julian Tornow (Fritz Haber Institute of Max Planck Society, Berlin, Germany).

Electron Energy Loss Spectroscopy (EELS)

EELS spectra were taken with a Philips CM200 spectrometer equipped with a field-emission cathode, resulting in an energy resolution of 0.9 eV. The measurements were performed by Dr. Julian Tornow (Fritz Haber Institute of Max Planck Society, Berlin, Germany).

Raman spectroscopy

Raman spectra were obtained using a Jobin Yvon LabRam spectrometer with excitation wavelength of 632.8 nm. The beam intensity was reduced to prevent thermal damage of the samples.

X-ray Photoelectron Spectroscopy (XPS)

XPS was carried out using a Thermo-Scietific K-Alpha instrument with monochromatic X-ray source $Al_{K\alpha}$ (1486.6 eV) and a monochromatic spot of 400 μm by Dr. Carmen Serra (University of Vigo, Vigo, Spain).

Nitrogen sorption

Nitrogen sorption analysis was performed using Quadrasorb SI (Quantachrome instrument) at 77K. Prior to measurements samples were degassed at 180 ^{0}C for 20 h. Surface area was determined using the Brunauer-Emmett-Teller (BET) method. The measurements were perfomed by Ms. Regina Rothe (Max Planck Institute of Colloids and Interfaces, Golm, Germany).

Electrochemical testing

Electrochemical experiments were performed using two-electrode Swagelok®-type cells. No ball-milling of materials prior to measurements has been performed. The working electrode consisted of 80 wt % active material ($LiFePO_4$). In the case of pristine (non-carbon coated) materials, 20 wt % of Ketjen® carbon black was mixed in the agate mortar.

In the case of carbon coated materials, smaller amount of Ketjen® carbon black was added, taking into account its composition. Glass fiber (GF/D) from Whatman® was used as a separator and pure lithium foil (Aldrich) was used as a counter/reference electrode. $LiPF_6$ (1 M) in ethylene carbonate/dimethyl carbonate (EC/DMC, 1:1 by volume) was used as electrolyte. The cells were assembled inside an argon-filled glove box. Galvanostatic charge/discharge experiments were carried out using a VMP2 potentiostat. An electrode composite weighing 10 mg was used for all tests of the materials. The experiments were performed by Dr. Rezan Demir-Cakan (Univerity of Picardie - Jules Verne, Amiens, France).